

UCLA

UCLA Electronic Theses and Dissertations

Title

Synthesis and characterization of nanostructured transition metal oxides for energy storage devices

Permalink

<https://escholarship.org/uc/item/34z248mr>

Author

Kim, Jong Woung

Publication Date

2012

Peer reviewed|Thesis/dissertation

UNIVERSITY OF CALIFORNIA

Los Angeles

Synthesis and characterization of nanostructured transition metal oxides
for energy storage devices

A dissertation submitted in partial satisfaction of the
requirements for the degree Doctor of Philosophy
in Materials Science and Engineering

by

Jong Woung Kim

2012

© Copyright by
Jong Woung Kim
2012

ABSTRACT OF THE DISSERTATION

Synthesis and characterization of nanostructured transition metal oxides
for energy storage devices

by

Jong Woung Kim

Doctor of Philosophy in Materials Science and Engineering

University of California, Los Angeles, 2012

Professor Bruce Dunn, Chair

Finding a promising material and constructing a new method to have both high energy and power are key issues for future energy storage systems. This dissertation addresses three different materials systems to resolve those issues. Pseudocapacitive materials such as RuO_2 and MnO_2 display high capacitance but Nb_2O_5 displays a different charge storage mechanism, one highly dependent on its crystal phase rather than its surface area. Various sol-gel techniques were used to synthesize the different phases of Nb_2O_5 and electrochemical testing was used to study their charge storage with some phases displaying comparable charge storage to MnO_2 . To overcome the electrical limitations of using an insulating material, the core-shell structure ($\text{Nb}_2\text{O}_5/\text{C}$) was also examined and the method could be generalized to improve other pseudocapacitors. Besides electronic conductivity, the diffusion of the electrolyte ions through the shell material is a critical factor for fast charging/discharging in the core-shell structure.

This dissertation also involves another topic, a reconfigurable electrode, that displays both high energy and power density. By constructing a reconfigurable electrode which has different electrical properties (metallic or insulating state) depending on the amount of intercalated ‘guest’ ions into ‘host’ material, it can be used as a battery or electrochemical capacitor material in the insulating or metallic state respectively. Metal oxide bronzes having metal-insulator transition were investigated in this study.

The dissertation of Jong Woung Kim is approved.

Sarah Tolbert

Xiangfeng Duan

Bruce Dunn, Committee Chair

University of California, Los Angeles

2012

To my family

TABLE OF CONTENTS

| | |
|---|-------|
| LIST OF FIGURES | ix |
| LIST OF TABLES | xvi |
| ACKNOWLEDGMENTS | xvii |
| VITA | xviii |
| Chapter 1. Introduction and objectives | 1 |
| Chapter 2. Niobium oxide (Nb ₂ O ₅) for Pseudocapacitors | 4 |
| Chapter 2.1. Introduction | 4 |
| Chapter 2.2. Technical Background..... | 7 |
| Chapter 2.2.1. Niobium oxide (Nb ₂ O ₅)..... | 7 |
| Chapter 2.2.2. Electrochemical capacitors (EDLCs and Pseudocapacitors) | 10 |
| Chapter 2.2.3. Nanostructured materials for pseudocapacitors | 12 |
| Chapter 2.3. Experimental | 13 |
| Chapter 2.3.1. Synthesis of Nb ₂ O ₅ | 13 |
| Chapter 2.3.2. Material Characterization | 14 |
| Chapter 2.3.3. Electrochemical characterization | 15 |
| Chapter 2.4. Results and Discussion..... | 15 |
| Chapter 2.4.1. Nb ₂ O ₅ synthesis and characterization | 15 |
| Chapter 2.4.2. The effect of crystallinity on pseudocapacitive behavior of Nb ₂ O ₅ | 23 |
| Chapter 2.4.3. Intercalation pseudocapacitance and structural stability of Nb ₂ O ₅ | 27 |
| Chapter 2.4.4. Electrolyte ion size effect | 31 |
| Chapter 2.4.5. Kinetic behavior of T-Nb ₂ O ₅ | 34 |

| | |
|---|----|
| Chapter 2.5. Conclusion..... | 39 |
| Chapter 3. Nb ₂ O ₅ /C core-shells for pseudocapacitors | 40 |
| Chapter 3.1. Introduction | 40 |
| Chapter 3.2. Experimental | 42 |
| Chapter 3.2.1. Synthesis an oxidation of core-shells | 42 |
| Chapter 3.2.2. Material chatacterization | 43 |
| Chapter 3.2.3. Electrochemical characterization | 44 |
| Chapter 3.3. Results and Discussion..... | 45 |
| Chapter 3.3.1. Synthesis and characterization of Nb ₂ O ₅ /C core-shell..... | 45 |
| Chapter 3.3.2. Voltammetry studies on Nb ₂ O ₅ /C core-shell..... | 54 |
| Chapter 3.3.3. The effect of oxidation on the kinetics of Nb ₂ O ₅ /C core-shell..... | 59 |
| Chapter 3.3.4. Electrochemical behavior of thick film (Bare Nb ₂ O ₅ vs. Nb ₂ O ₅ /C core-shell) | 65 |
| Chapter 3.4. Conclusion..... | 67 |
| Chapter 4. Transition metal oxide bronzes for reconfigurable electrodes | 68 |
| Chapter 4.1. Introduction | 68 |
| Chapter 4.2. Technical backgrounds: Transition metal oxide bronzes | 69 |
| Chapter 4.2.1. Sodium tungsten bronze (Na _x WO ₃) | 69 |
| Chapter 4.2.2. Sodium molybdenum bronzes (Na _x MoO ₃ or Na _{0.9} Mo ₆ O ₁₇)..... | 71 |
| Chapter 4.3. Experimental | 73 |
| Chapter 4.3.1. Synthesis of Cubic Na _{0.85} WO ₃ | 73 |
| Chapter 4.3.2. Synthesis of Na _{0.9} Mo ₆ O ₁₇ | 74 |

| | |
|--|----|
| Chapter 4.3.3. Material characterization..... | 75 |
| Chapter 4.3.4. Electrochemical characterization | 76 |
| Chapter 4.4. Results and Discussion..... | 77 |
| Chapter 4.4.1. Synthesis and characterization of Sodium tungsten bronze (Na_xWO_3) | 77 |
| Chapter 4.4.2. Electrochemical behavior of Sodium tungsten bronze ($\text{Na}_{0.85}\text{WO}_3$)..... | 79 |
| Chapter 4.4.3. Synthesis and characterization of $\alpha\text{-MoO}_3$ and $\text{Na}_{0.9}\text{Mo}_6\text{O}_{17}$ | 81 |
| Chapter 4.4.4. Electrochemical behavior of Sodium molybdenum bronze ($\text{Na}_{0.9}\text{Mo}_6\text{O}_{17}$).. | 92 |
| Chapter 4.5. Suggestions for future work | 95 |
| Chapter 5. Conclusions | 98 |

LIST OF FIGURES

| | |
|---|----|
| Figure 1.1. Ragone plot of various energy storage systems ^[1] | 2 |
| Figure 2.1. Polymorphism of niobium oxide (Nb ₂ O ₅) ^[17] | 8 |
| Figure 2.2. Projection of the structure of orthorhombic <i>T</i> -Nb ₂ O ₅ parallel to the [001] plane; (○) oxygen, (○,●) niobium ^[18] | 9 |
| Figure 2.3. Crystal structure of <i>H</i> -Nb ₂ O ₅ ; (bold diamond) NbO ₆ octahedra, (●) Nb in tetrahedral site. ^[19] | 10 |
| Figure 2.4. Mechanism for electrochemical capacitors: (a) Electrochemical double layer capacitors (EDLCs) and (b) Pseudocapacitors. | 11 |
| Figure 2.5. Sol-gel process of metal alkoxide..... | 16 |
| Figure 2.6. Ring-opening reaction of propylene oxide with acid ^[31] | 17 |
| Figure 2.7. Condensation steps for non-aqueous sol-gel process based on reacting metal halides in benzyl alcohol ^[32] | 17 |
| Figure 2.8. X-ray diffraction patterns for different phases of Nb ₂ O ₅ : a) dehydrated amorphous Nb ₂ O ₅ aerogel, b) pseudohexagonal (<i>TT</i> -Nb ₂ O ₅), c) orthorhombic (<i>T</i> -Nb ₂ O ₅)..... | 18 |
| Figure 2.9. Transmission electron microscopy (TEM) images for the different Nb ₂ O ₅ phases: a) as-synthesized Nb ₂ O ₅ aerogel, b) dehydrated Nb ₂ O ₅ aerogel, c) pseudohexagonal (<i>TT</i> -Nb ₂ O ₅), d) orthorhombic (<i>T</i> -Nb ₂ O ₅). | 20 |
| Figure 2.10. Raman spectra of Nb ₂ O ₅ with different crystalline structure; A peak at 520 cm ⁻¹ is caused by Si substrate which was used for measurement..... | 22 |
| Figure 2.11. TEM image of Nb ₂ O ₅ heat treated at 800 °C for 2 hrs in air; Nb ₂ O ₅ aerogel synthesized in this study was used as a precursor material | 22 |

| | |
|---|----|
| Figure 2.12. Voltammetric sweeps (10 mV/s in 1 M LiClO ₄ in propylene carbonate) demonstrate that the stainless steel substrate (SS) contributes very little to the total current..... | 23 |
| Figure 2.13. Voltammetric sweeps for Nb ₂ O ₅ in lithium ion electrolyte: CVs at 10 mV/s for different Nb ₂ O ₅ phases. | 24 |
| Figure 2.14. Charge storage as a function of charging time for different Nb ₂ O ₅ phases..... | 25 |
| Figure 2.15. The surface-area normalized capacitance for different Nb ₂ O ₅ phases in Li ⁺ electrolyte..... | 26 |
| Figure 2.16. HR-TEM images of <i>T</i> -Nb ₂ O ₅ : a) pristine material, b) lithiated to 1.2 V (vs. Li/Li ⁺), c) delithiated to 3 V (vs Li/Li ⁺) after cycling 10 times at 100 mV/s. (scale bar: 5nm)..... | 29 |
| Figure 2.17. Electron diffraction (ED) studies of <i>T</i> -Nb ₂ O ₅ : a) pristine material, b) after lithiation, c) after delithiation. The orthorhombic phase of <i>T</i> -Nb ₂ O ₅ is maintained after lithium insertion and deinsertion. (scale bar: 2 1/nm)..... | 30 |
| Figure 2.18. Effect of electrolyte ion size on electrochemical behavior of Nb ₂ O ₅ : CV at 5 mV/s for <i>T</i> -Nb ₂ O ₅ using Li ⁺ (—) or Na ⁺ (- - -) electrolytes..... | 31 |
| Figure 2.19. The surface-area normalized capacitance for different Nb ₂ O ₅ phases in Na ⁺ electrolytes | 32 |
| Figure 2.20. Voltammetric sweeps for Nb ₂ O ₅ materials in sodium ion electrolyte (1 M NaClO ₄ in propylene carbonate). Current is normalized by weight..... | 33 |
| Figure 2.21. Voltammetric sweeps for Nb ₂ O ₅ materials in sodium ion electrolyte (1 M NaClO ₄ in propylene carbonate). Current is normalized by surface area..... | 33 |

| | |
|---|----|
| Figure 2.22. Determination of the infinite sweep-rate capacitance of $T\text{-Nb}_2\text{O}_5$: the capacity as a function of sweep rate $^{-1/2}$, the y-intercept is 470 C/g and represents the infinite sweep rate capacity | 35 |
| Figure 2.23. The contribution of the capacity at infinite sweep rate to the total charge storage .. | 36 |
| Figure 2.24. Nyquist representation of impedance spectra for the $T\text{-Nb}_2\text{O}_5$ nanocrystal electrode at two different potentials, before any lithiation at open-circuit (a), and (b) after lithiating to 1.2 V. The circuit model used for fitting is shown in (c), where R_{el} is the electrolyte resistance, CPE_{dl} is the double-layer capacitance present at all electrode/electrolyte interfaces, R_f is the faradaic charge transfer resistance, and CPE_{pseudo} is the pseudocapacitance. CPE is the constant phase element ($Z_{CPE} = [B(j\omega)^n]^{-1}$, where B and n are constants and ω is the frequency). Simulations indicate that R_f decreases on lithiation from 14.3 kohms to 15 ohms. | 38 |
| Figure 3.1. Synthesis of $\text{Nb}_2\text{O}_5/\text{C}$ core-shell | 45 |
| Figure 3.2. TEM images of bare $T\text{-Nb}_2\text{O}_5$ and $\text{Nb}_2\text{O}_5/\text{C}$ core-shells; (a) Bare $T\text{-Nb}_2\text{O}_5$ nanoparticles, (b) As-synthesized $\text{Nb}_2\text{O}_5/\text{C}$ core-shells (average shell thickness: 5 nm), (c) $\text{Nb}_2\text{O}_5/\text{C_F700}$ and (d) Oxidized $\text{Nb}_2\text{O}_5/\text{C_F700}$ | 47 |
| Figure 3.3. $\text{Nb}_2\text{O}_5/\text{C}$ core-shell with different shell thickness; (a) 10-15 nm ($M_{\text{glucose}}/M_{\text{Nb}_2\text{O}_5} \sim 220$), (b) 5 nm ($M_{\text{glucose}}/M_{\text{Nb}_2\text{O}_5} \sim 110$) and (c) 2 nm ($M_{\text{glucose}}/M_{\text{Nb}_2\text{O}_5} \sim 55$) | 48 |
| Figure 3.4. TEM image of Nb_2O_5 annealed at 700 °C (ave. particle size ~ 100 nm in dia.) | 49 |
| Figure 3.5. XPS spectra of bare $T\text{-Nb}_2\text{O}_5$ and $\text{Nb}_2\text{O}_5/\text{C}$ core-shells; (a) C 1s and (b) Nb 3d..... | 49 |
| Figure 3.6. FT-IR spectra of $\text{Nb}_2\text{O}_5/\text{C}$ core-shells; Upon oxidation, peaks for carboxylic groups increases dramatically | 50 |

| | |
|--|----|
| Figure 3.7. XRD patterns of the bare Nb ₂ O ₅ and Nb ₂ O ₅ /C core-shells; (a) Bare Nb ₂ O ₅ , (b) As-synthesized Nb ₂ O ₅ /C core-shell, (c) Nb ₂ O ₅ /C_F700 and (d) Oxidized Nb ₂ O ₅ /C_F700 | 51 |
| Figure 3.8. Raman spectra of Nb ₂ O ₅ /C core-shells; (a) As-synthesized Nb ₂ O ₅ /C, (b) Nb ₂ O ₅ /C_F700, and (c) Oxidized Nb ₂ O ₅ /C_F700..... | 53 |
| Figure 3.9. Thermal gravimetric analysis (TGA) on Nb ₂ O ₅ /C core-shells (in air)..... | 54 |
| Figure 3.10. Cyclic voltammetry (CVs) for Nb ₂ O ₅ /C core-shells (thin film~20 µg) at 10 mV/s. | 55 |
| Figure 3.11. Specific charge of bare Nb ₂ O ₅ and Nb ₂ O ₅ /C core-shells at different sweep rates (2-100 mV/s). Mass loading is ~ 20 µg (film thickness is less than 200 nm). | 55 |
| Figure 3.12. Electrochemical impedance spectra (EIS) for Nb ₂ O ₅ /C_F700 and oxidized Nb ₂ O ₅ /C_F700 (at 1.2 V (vs. Li/Li ⁺)); (a) Nyquist plot and (b) phase angle as a function of frequency..... | 58 |
| Figure 3.13. The circuits for Nb ₂ O ₅ /C_F700 (a) and oxidized Nb ₂ O ₅ /C_F700 (b). | 59 |
| Figure 3.14. Charge storage as a function of sweep rate ^{-1/2} (Specific charge is based on the active material) | 60 |
| Figure 3.15. b-value characterization for oxidized Nb ₂ O ₅ /C_F700 using the current at peak potentials at sweep rates of 0.1 – 10 mV/s..... | 61 |
| Figure 3.16. Capacitive contribution in oxidized Nb ₂ O ₅ /C_F700 at 10 mV/s..... | 62 |
| Figure 3.17. Cyclic voltammetry on oxidized Nb ₂ O ₅ /C_F700 using different electrolytes: LiClO ₄ in PC and TEABF ₄ in acetonitrile..... | 64 |
| Figure 3.18. Capacity of bare Nb ₂ O ₅ and oxidized Nb ₂ O ₅ /C_F700. Mass loading on stainless current collector is ~0.5 mg. Film thickness is ~ 5 µm..... | 66 |
| Figure 4.1. Optical properties of Na _x WO ₃ with Na concentration ^[77] | 70 |

| | |
|--|----|
| Figure 4.2. Phase diagram of Na_xWO_3 with Na concentration ^[77] | 70 |
| Figure 4.3. Crystal structure of purple molybdenum bronze ($\text{K}_{0.9}\text{Mo}_6\text{O}_{17}$) ^[79] | 72 |
| Figure 4.4. Crystal structure of purple molybdenum bronze ($\text{Li}_{0.9}\text{Mo}_6\text{O}_{17}$) projected in ac plane ^[81] | 73 |
| Figure 4.5. XRD pattern of $\text{Na}_{0.85}\text{WO}_3$ | 78 |
| Figure 4.6. Scanning Electron Microscopy (SEM) image of Na_xWO_3 (x=0.85) | 78 |
| Figure 4.7. CV curves of $\text{Na}_{0.85}\text{WO}_3$ at different sweep rates | 79 |
| Figure 4.8. Galvanostatic charge/discharge curves of $\text{Na}_{0.85}\text{WO}_3$ | 80 |
| Figure 4.9. Ragone plot showing the energy and power density spectrum for an asymmetric electrochemical capacitor Na_xWO_3 – activated carbon. The device characteristics are shown in red. The other samples represent other types of carbon-based capacitors (after reference [86]) | 81 |
| Figure 4.10. Charge (z) versus pH diagram ^[87] ; the ‘aquo ($\text{M}(\text{OH})_2$)’, ‘hydroxo ($\text{M}(\text{OH})$)’ and ‘oxo ($\text{M}=\text{O}$)’ domains depend on valence of cation and pH | 82 |
| Figure 4.11. XRD patterns for (a) as-synthesized MoO_3 aerogel and (b) MoO_3 aerogel after thermal annealing at 400°C | 82 |
| Figure 4.12. Raman spectrum of MoO_3 aerogel annealed at 400 °C | 83 |
| Figure 4.13. FT-IR spectrum of MoO_3 aerogel annealed at 400 °C | 83 |
| Figure 4.14. TEM images of (a) as-synthesized MoO_3 aerogel and (b) $\alpha\text{-MoO}_3$ after thermal annealing at 400°C | 84 |

| | |
|---|----|
| Figure 4.15. XRD patterns of MoO_x synthesized by microwave-assisted solvothermal reaction using co-solvent (DI water + ethanol); (a) As-synthesized MoO_2 and (b) After heat treatment at 450 °C in air (ST- MoO_3)..... | 85 |
| Figure 4.16. TEM images of MoO_x synthesized by microwave-assisted solvothermal reaction using co-solvent (DI water + ethanol); (a) As-synthesized MoO_2 and (b) After heat treatment at 450 °C in air (ST- MoO_3)..... | 86 |
| Figure 4.17. XRD pattern of N- MoO_3 | 87 |
| Figure 4.18. SEM image of N- MoO_3 | 87 |
| Figure 4.19. XRD pattern of Mo bronzes; (a) as-synthesized and (b) after heat treatment at 400 °C in Ar | 89 |
| Figure 4.20. TGA and DTA on the hydrated sodium molybdenum bronze in Ar atmosphere | 90 |
| Figure 4.21. TEM image of $\text{Na}_{0.9}\text{Mo}_6\text{O}_{17}$ synthesized using ST- MoO_3 | 91 |
| Figure 4.22. SEM image of $\text{Na}_{0.9}\text{Mo}_6\text{O}_{17}$ synthesized using N- MoO_3 | 91 |
| Figure 4.23. CV curves of $\text{Na}_{0.9}\text{Mo}_6\text{O}_{17}$ synthesized using ST- MoO_3 with different electrolyte ions (Li^+ and Na^+) at the sweep rate of 10 mV/s | 92 |
| Figure 4.24. The capacity of $\text{Na}_{0.9}\text{Mo}_6\text{O}_{17}$ synthesized using ST- MoO_3 with different electrolyte ions (Li^+ and Na^+) at different sweep rates | 93 |
| Figure 4.25. CV curve of $\text{Na}_{0.9}\text{Mo}_6\text{O}_{17}$ synthesized using N- MoO_3 at different sweep rates (2 - 100 mV/s)..... | 94 |
| Figure 4.26. The capacity of $\text{Na}_{0.9}\text{Mo}_6\text{O}_{17}$ synthesized using N- MoO_3 | 94 |
| Figure 4.27. b-value characterization for $\text{Na}_{0.9}\text{Mo}_6\text{O}_{17}$ synthesized using N- MoO_3 ; (a) at cathodic peak, (b) at anodic peak | 95 |

Figure 4.28. TGA & DTA of MoO₂ synthesized via microwave-assisted hydrothermal process. 96

LIST OF TABLES

| | |
|---|----|
| Table 2.1. Brunauer-Emmett-Teller (BET) surface areas for different phases of Nb ₂ O ₅ nanoparticles. | 19 |
| Table 3.1. Brunauer-Emmett-Teller (BET) surface areas and average pore sizes for Nb ₂ O ₅ /C core-shells with different shell thickness. | 52 |
| Table 3.2. The values of circuit elements for Nb ₂ O ₅ /C_F700 | 59 |
| Table 3.3. The values of circuit elements for oxidized Nb ₂ O ₅ /C_F700..... | 59 |

ACKNOWLEDGMENTS

I'd like to express my sincere appreciation to my advisor, Prof. Bruce Dunn, for his outstanding mentorship for the past 5 years. His leadership and generosity enabled me to complete the works during my Ph.D. program. I feel extremely fortunate to have spent my graduate career with him.

I would also like to thank my labmates at UCLA, Dr. Esther Lan, Dr. Jonathan Fang, Dr. Thibaut Forestier, Dr. Hyunchul (Jeff) Lee, Dr. Enrico Gaspera, Dr. Emilie Perre, Dr. Ryan Maloney, Dr. Grant Umeda, Dr. Steven Jonas, Peter Malati, Nicolas Cirigliano, Veronica Augustyn, Wade Richardson, Rita Blaik, Daniel Membreno, Kurt Star, Joy Trujillo, Hyungsuk (Jimmy) Kim, Jesse Ko, Danielle Casillas, Jing-Yu (Rebecca) Chen, Chun-Han (Matt) Lai, for their help and supports.

I would also like to thank my dissertation committee, Prof. Xiangfeng Duan, Prof. Sarah Tolbert, and Prof. Suneel Kodambaka for their valuable time and discussion.

I would also like to thank my friend, Dr. Choong-heui Chung, at UCLA who studied together and spent lots of time for discussion and joy during my Ph.D. program.

I cannot thank enough to my family in South Korea. Their endless support and prayers always give me a strength and confidence. Most of all, I thank my fiancée, Boyoun Choi, for her deep understanding, patience, and love to make this possible.

VITA

- 2005 B.S. in Chemical Engineering

 Chung-Ang University, Seoul, South Korea
- 2007 M.S. in Chemical Engineering

 Chung-Ang University, Seoul, South Korea
- 2007-2012 Graduate Student Researcher

 Department of Materials Science and Engineering

 University of California, Los Angeles

PUBLICATIONS AND PRESENTATIONS

V. Augustyn, J. Come, J.W. Kim, M. Lowe, P.L. Taberna, H. Abruna, S. Tolbert, P. Simon and B. Dunn, “A new mechanism for high rate lithium-ion storage through intercalation pseudocapacitance”, *Nature Materials*, submitted (2012)

J.W. Kim, V. Augustyn and B. Dunn, “The effect of crystallinity on the rapid pseudocapacitive response of Nb₂O₅”, *Advanced Energy Materials*, 2, 141-148 (2012)

J.E. Trujillo, J.W. Kim, E.H. Lan, B. Dunn, “Combining Positive and Negative Thermal Expansion Materials to Tailor the Coefficient of Thermal Expansion in Metal/Ceramic Composites”, Materials Science & Technology (MS&T), Pittsburgh, PA, Oct. 7-11 (2012)

J.E. Trujillo, J.W. Kim, E.H. Lan, S. Sharratt, Y.S. Ju and B. Dunn, “Metal-matrix nanocomposites with tailored coefficients of thermal expansion for improved thermomechanical reliability”, *Journal of Electronic Materials*, 41, 1020-1023 (2011)

V. Augustyn, J.W. Kim, T.E. Quickel, S. Tolbert and B. Dunn, "The Development of Pseudocapacitance in Nanostructured Transition Metal Oxide Materials", The 220th ECS meeting, Boston, MA, Oct. 9-14 (2011)

V. Augustyn, J.W. Kim, T.E. Quickel, S. Tolbert and B. Dunn, "The roles of material structure and morphology on the pseudocapacitance of niobium pentoxide", The 2011 MRS spring meeting, San Francisco, CA, Apr. 25-29

J.W. Kim, L.U. Kim and C.K. Kim, "Size Control of the Silica Nanoparticles and Their Surface Treatment for the Fabrication of Dental Nanocomposites", *Biomacromolecules*, 8, 215-222 (2007)

J.W. Kim, J.S. Yoo and C.K. Kim, "Continuous Nanocomposite Coatings on a Phosphor for the Enhancement of the Long-term Stability", The 232nd ACS National Meeting, San Francisco, CA, Sep. 10-14 (2006)

L.U. Kim, J.W. Kim and C.K. Kim, "Effects of Molecular Structure of the Resins on the Volumetric Shrinkage and the Mechanical Strength of Dental Restorative Composites", *Biomacromolecules*, 7, 2680-2687 (2006)

J.W. Kim, L.U. Kim, C.K. Kim, B.H. Cho and O.Y. Kim, "Characteristics of Novel Dental Composites Containing 2,2-Bis[4-(2-methoxy-3-methacryloyloxy propoxy) phenyl] propane as a Base Resin.", *Biomacromolecules*, 7, 154-160 (2006)

E.J. Moon, J.W. Kim and C.K. Kim, "Fabrication of membranes for the liquid separation Part 2: Microfiltration membranes prepared from immiscible blends containing polysulfone and poly(1-vinylpyrrolidone-co-acrylonitrile) copolymers", *Journal of Membrane Science*, 274, 244-251 (2006)

J.W. Kim, E.J. Moon and C.K. Kim, "New miscible blends composed of polysulfone and poly(1-vinylpyrrolidone-co-acrylonitrile) copolymers and their phase behavior", *Polymer*, 46, 5662-5672 (2005)

J.W. Kim, J.E. Yoo and C.K. Kim, "Phase behavior of ternary blends containing dimethylpolycarbonate, tetramethylpolycarbonate and poly[styrene-co-(methyl methacrylate)] copolymers (or polystyrene)", *Polymer International*, 54, 130-136 (2005)

J.W. Kim, Y. Kim and C.K. Kim, "Effect of molecular weight distribution on the spinodal temperature of polymer mixtures", *Polymer International*, 53, 2059-2065 (2004)

Chapter 1. Introduction and objectives

Advancement comes from improvements in technology and energy storage has become the limiting factor to new technology. The ever increasing use of portable electronics, electric vehicles and large industrial equipment have increased both the power and energy demands to the limit of commercial energy storage technology comprised of batteries, fuel cells and electrochemical capacitors (also called supercapacitors). The limitations of commercial energy storage come from the tradeoff between energy and power. For example, batteries and fuel cells suffer from their low power density while supercapacitors have low energy density (Figure 1.1). Various efforts such as using nanotechnology and conductive additives have been made to achieve higher power density while minimizing the loss in energy density. Finding new materials is a crucial task that has so far been the only method for improving on the energy density of state of the art materials. A deeper understanding on charge storage mechanism is essential to resolve these energy storage challenges. This dissertation addresses three materials systems to demonstrate the following: (1) finding a promising supercapacitor material, (2) developing a method that can improve the power density of electrode materials limited by their electrical conductivity, and (3) proposal of a new concept for both high energy and power density electrode.

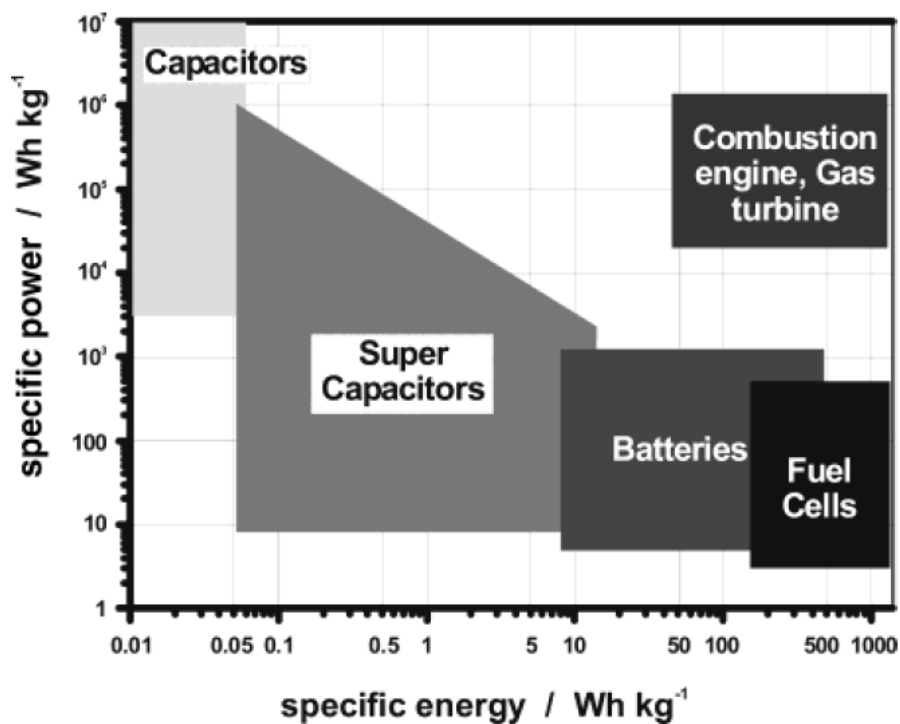


Figure 1.1. Ragone plot of various energy storage systems^[1]

The first system that is presented in this dissertation is niobia (Nb_2O_5). This is the first study of nanocrystalline niobia particles as a pseudocapacitor material. Its outstanding electrochemical performance makes it promising. In this study, the effects of crystallinity of materials on pseudocapacitive behavior were also investigated. For this study, nano-sized niobia with different crystalline structures was synthesized by annealing of an aerogel or by a solvothermal non-aqueous sol-gel process.

The second system discussed in this dissertation is transition metal oxides/carbon ($\text{Nb}_2\text{O}_5/\text{C}$) composite with core-shell structure (0-D). Carbon has long been a conductive

additive but the improvement of the core-shell structure has not previously been applied to supercapacitor materials, even though it has been used to improve battery materials. In this study, The challenges of synthesizing and modifying the core-shell structure were investigated to improve the power density of the metal oxide composites. The core-shell structures were fabricated via microwave-assisted hydrothermal process followed by thermal annealing for carbonization and oxidation.

The third system presented in this dissertation involves the design and preparation of reconfigurable electrodes by using the variable electrical properties exhibited by certain intercalation materials. Sodium tungsten bronzes (Na_xWO_3) and purple molybdenum bronze ($\text{Na}_{0.9}\text{Mo}_6\text{O}_{17}$) are of particular interest for this study, and were synthesized by the insertion of sodium ion into tungsten oxide (WO_3) and molybdenum oxide ($\alpha\text{-MoO}_3$) frameworks, respectively. By tailoring the composition of the material and controlling its electrical conductivity, we engineered the bronzes to produce high energy and power within the same basic material.

Chapter 2. Niobium oxide (Nb₂O₅) for Pseudocapacitors

Chapter 2.1. Introduction

The intense interest in electrochemical energy storage can be traced to a wide range of applications which impact daily life, from portable electronics to electric vehicles to the power grid. Although capacitive energy storage has not been as thoroughly investigated as batteries, it is evident that electrochemical capacitors possess a number of desirable properties which can complement or replace batteries: fast charging (within seconds), long-term cycling and up to ten times more power than batteries.^[2]

Energy storage mechanisms for electrochemical capacitors are fundamentally different from those of batteries. Electrochemical double layer capacitors (EDLCs) store charge at the interface between the electrode, typically carbon, and a liquid electrolyte. This type of capacitance exists at every electrified surface and is directly proportional to the material's surface area. High surface area carbons are the material of choice for EDLCs, and the highest specific capacitance values are around 150 F/g.^[3] A second capacitive storage mechanism is pseudocapacitance, which involves reversible faradaic reactions. These reactions can occur from ions adsorbing onto the surface of the material or, if the material has a layered or tunnel structure, being inserted within specific ion-conducting planes or channels.^[4] The specific capacitance values can be significantly larger for pseudocapacitive materials (> 1,000 F/g) compared to EDLCs because of the greater level of charge storage associated with redox reactions. Thus, there is considerable interest in investigating pseudocapacitive materials since the energy density associated with faradaic reactions is much higher, by approximately an order

of magnitude, than EDLCs such as carbon. Transition metal oxides are the most well-studied class of inorganic pseudocapacitive materials because of the ease of synthesis and the facile electrochemical reduction of materials with high-oxidation states.^[5]

Among the different pseudocapacitor materials, RuO₂ and MnO₂ have received the most study. RuO₂, the first pseudocapacitor investigated in any detail, provides insight into some of the properties required for a successful pseudocapacitive material – appropriate redox reactions at the surface (or near surface) and high electronic conductivity. As a wide band gap semiconductor, MnO₂ has a much lower electrical conductivity and this tends to keep the specific capacitance well below theoretical values, although there are some instances where specific capacitance values close to theoretical, above 1,200 F/g, were reached.^[6] Other transition metal oxides that have received some study include V₂O₅ and NiO, both of which have demonstrated specific capacitance values > 1,000 F/g under specific experimental conditions.^[5, 7] However, similar to MnO₂, these materials also suffer from low electronic conductivity.

Currently, there is little fundamental understanding of what leads to good pseudocapacitive properties. While high surface area has always been an important consideration for EDLCs, recent work with MnO₂ showed that, in fact, surface area had limited impact when charge storage was mainly faradaic.^[8] Results with mesoporous transition metal oxides have shown the benefit of developing a well-controlled, interconnected porous architecture; the porosity enables electrolyte access to the redox-active pore walls. Moreover, for ‘iso-oriented’ systems, MoO₃ and Nb₂O₅, alignment along certain crystallographic directions leads to higher specific capacitance compared to amorphous materials of the same composition due to an additional pseudocapacitive contribution.^[9] The results obtained with mesoporous Nb₂O₅ films

were particularly intriguing because of fast kinetics in addition to high specific capacitance. However, it was not clear from this initial work whether the observed behavior was unique to mesoporous iso-oriented films or whether it was the result of the fundamental charge storage properties of Nb₂O₅.

The electrochemical behavior of Nb₂O₅ was first investigated by Bard *et al.*^[10, 11], who demonstrated that Nb₂O₅ exhibits lithium and proton insertion and is also electrochromic. These studies led to further research of Nb₂O₅ as a lithium-ion battery electrode and as an electrochromic window. Lithium insertion into Nb₂O₅ occurs below 2 V (vs. Li/Li⁺) and the material has been incorporated in 2 V lithium-ion secondary batteries that employ a lithium alloy as the negative electrode.^[12] The reversibility of the lithium intercalation process is well established; the amount of lithium insertion in Li_xNb₂O₅ varies between $x = 1.6$ to 2, for a maximum capacity of 728 C/g or ~ 200 mAh/g. In the electrochromics field, kinetics plays a larger role since fast coloration times are needed and Nb₂O₅ films can color in as fast as 10 seconds.^[13] This kinetic response, along with a large difference between the colored and bleached state, renders Nb₂O₅ as one of the best inorganic electrochromic materials.^[13]

The prior research does not indicate whether one particular phase of Nb₂O₅ is better than another; the application area seems to determine the desired Nb₂O₅ phase. Thus, the pseudo-hexagonal phase of Nb₂O₅ is preferred for electrochromic devices^[11] while the tetragonal phase seems to lead to the best battery electrodes^[12]. In general, the basic question of how crystal structure and phase influence capacitive storage is only beginning to be considered. The work reported by Favier *et al.*^[8] on MnO₂ polytypes demonstrated that the crystallographic structure has a significant influence on the capacitive storage behavior of the material. In particular, three-

dimensional MnO_2 spinels exhibited greater specific capacitance than MnO_2 phases with either 2D or 1D structures.

In this chapter, the effects of phase and crystallinity on the fundamental charge storage properties of Nb_2O_5 nanoparticles are examined. For the most part, the capacitive storage properties of Nb_2O_5 have not been investigated. What is particularly attractive for this system is that the linear dependence of peak current on sweep rate for mesoporous Nb_2O_5 suggests that this material possesses much better charge storage kinetics than other transition metal oxides.^[9] In the current study, different phases of Nb_2O_5 nanoparticles were synthesized through sol gel routes and the electrochemical properties were determined using electrodes composed only of nanoparticle powders, i.e., with no binders or conductive additives to complicate the measured response. Electrochemical studies show that orthorhombic Nb_2O_5 exhibits high specific capacitance at high rates, with nearly 400 F/g being stored reversibly within 12 seconds. These values are comparable to what has been reported for RuO_2 . In addition, the crystal phase of the Nb_2O_5 nanoparticles and the size of the ion are identified as being significant factors in the charge storage process.

Chapter 2.2. Technical Background

Chapter 2.2.1. Niobium oxide (Nb_2O_5)

Niobium is one of the group V metals and forms niobium pentoxide, Nb_2O_5 , with oxygen when it has oxidation state of +5. Nb_2O_5 is an electronic insulator; its bulk resistivity is $\sim 3 \times 10^4$ $\Omega\text{-cm}$ at 300K with a bandgap of ~ 3.4 eV^[14, 15] and comprised of polyhedra (Nb adjacent to 6,7

or 6 oxygens) sharing their edges and corners. There are many polymorphs of Nb_2O_5 depending on the temperature at which amorphous Nb_2O_5 is crystallized through thermal treatment.^[16, 17] The amorphous Nb_2O_5 begins to crystallize in a “low-temperature” form called the *TT* form (from the German “tief-tief” for low-low) at about 773K. At higher temperature, *T*-, *M*- (“Medium-temperature”) and *H*- (“High-temperature”) Nb_2O_5 forms. *P* (“Prism”) and *B* (“Blatter,” German for “leaflets”) Nb_2O_5 can be also formed through other synthetic routes. As shown in Figure 2.1, the crystallization behavior of niobium pentoxide is influenced by the starting materials used, impurities that may be present, and any interactions with other components.

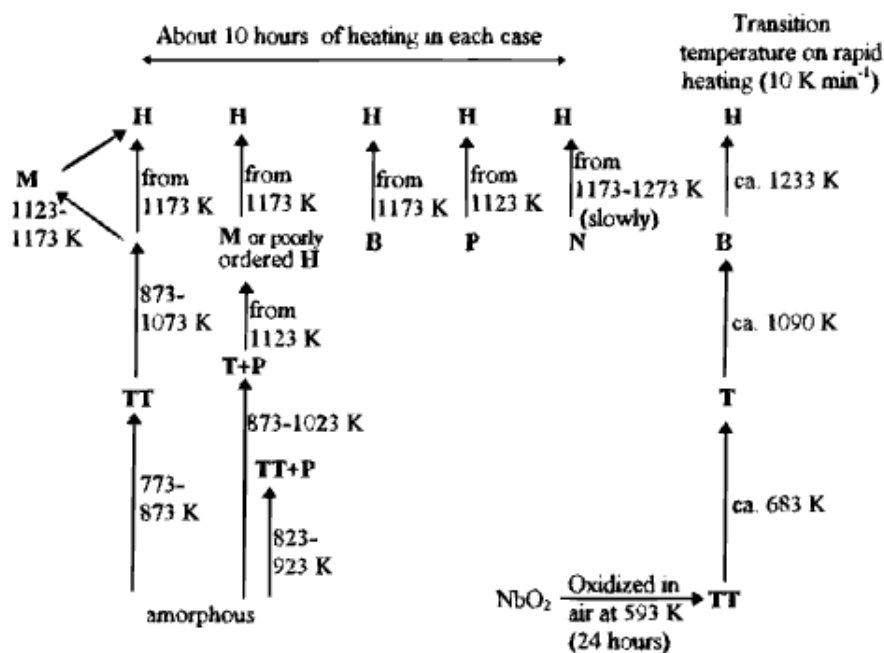


Figure 2.1. Polymorphism of niobium oxide (Nb_2O_5)^[17]

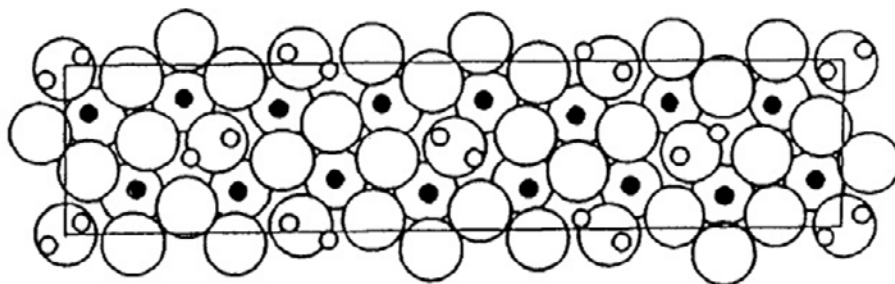


Figure 2.2. Projection of the structure of orthorhombic $T\text{-Nb}_2\text{O}_5$ parallel to the $[001]$ plane; (\bigcirc) oxygen, (\bigcirc , \bullet) niobium^[18]

Among the various phases of Nb_2O_5 , pseudohexagonal $TT\text{-Nb}_2\text{O}_5$, orthorhombic $T\text{-Nb}_2\text{O}_5$ and monoclinic $H\text{-Nb}_2\text{O}_5$ are the most common phases due to the ease of synthesis. Pseudohexagonal $TT\text{-Nb}_2\text{O}_5$ and orthorhombic $T\text{-Nb}_2\text{O}_5$ have long been thought to be the same, because they have similar X-ray diffraction patterns and the $TT\text{-Nb}_2\text{O}_5$ phase does not always form from pure components as starting material. These observations suggest that $TT\text{-Nb}_2\text{O}_5$ may simply be a less crystalline form of $T\text{-Nb}_2\text{O}_5$, stabilized by impurities. The main differences are that some of the oxygen atoms in $T\text{-Nb}_2\text{O}_5$ are replaced by monovalent species (such as Cl^-) or vacancies.^[16] The unit cell of orthorhombic $T\text{-Nb}_2\text{O}_5$ contains 42 oxygen atom positions (large open circles in Figure 2.2). Eight of the Nb ions are present in distorted octahedra, while another eight Nb ions occupy pentagonal bipyramids. The remaining 0.8 Nb ion per unit cell is located in interstitial 9-coordinated sites in the unit cell (small open circles).^[18] Monoclinic $H\text{-Nb}_2\text{O}_5$, on the other hand, has an entirely different structure. $H\text{-Nb}_2\text{O}_5$ has a shear structure consisting of blocks of NbO_6 octahedra (3×4 and 3×5) that share corners with octahedra in their own block and edges with octahedra in other blocks. One of the 28 Nb atoms in each unit cell is present in a

tetrahedral site, which occurs at some block junctions, as depicted by the black circles in Figure 2.3.^[19]

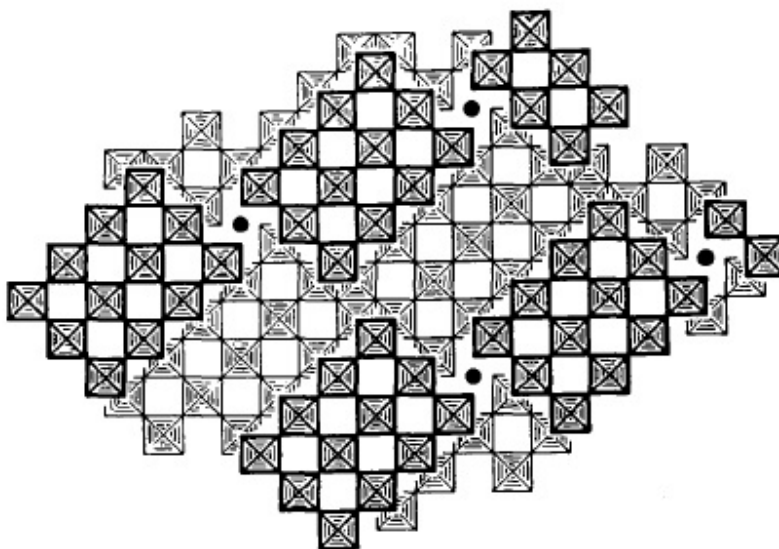


Figure 2.3. Crystal structure of $H\text{-Nb}_2\text{O}_5$; (bold diamond) NbO_6 octahedra, (●) Nb in tetrahedral site.^[19]

Chapter 2.2.2. Electrochemical capacitors (EDLCs and Pseudocapacitors)

There are two different types of electrochemical capacitors, electrochemical double layer capacitors (EDLCs) and pseudocapacitors. For EDLCs, electrical charge is stored directly at an electrified interface (Figure 2.4-(a)). The charge storage process for EDLCs is non-faradaic where no electron transfer takes place across the electrode interface. Electrical energy is stored through electrostatic charge accumulation at the interface in the absence of any redox chemical changes. On the other hand, pseudocapacitance occurs through a redox charge transfer process at

the electrode surface (Figure 2.4-(b)). Such a process is faradaic in origin because it involves electron transfer across the double layer at the electrode/electrolyte interfaces. The electrical energy is stored through electrosorption, redox reactions and intercalation processes.^[20] Pseudocapacitor materials can achieve very high capacitance from these faradaic processes. In addition to pseudocapacitance, materials will also possess an additional double-layer capacitance which arises non-faradaically at the electrode interfaces. Normally, the pseudocapacitive contribution (area normalized), can be 10 - 100 times higher than the double-layer capacitance.

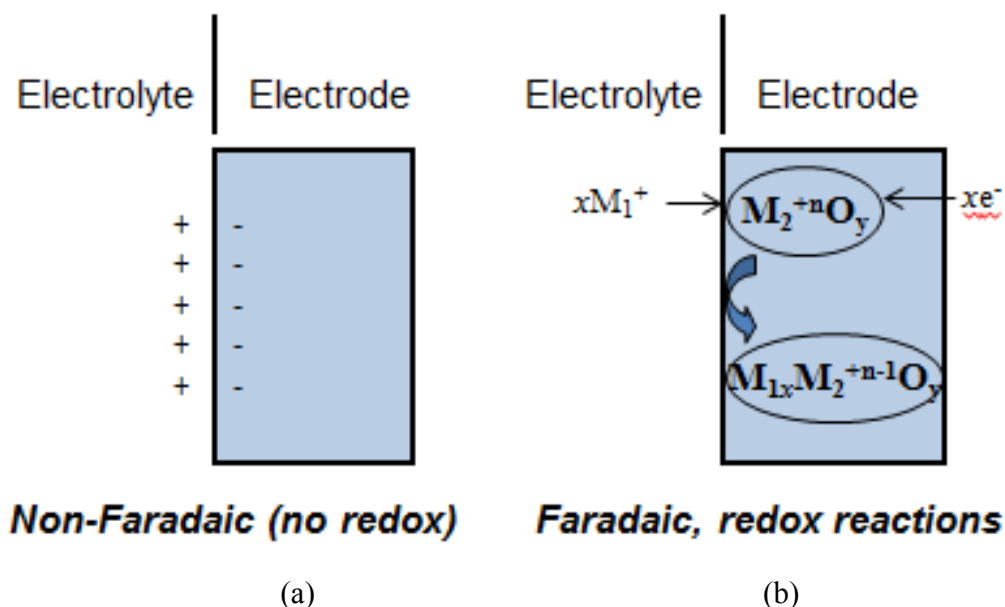


Figure 2.4. Mechanism for electrochemical capacitors: (a) Electrochemical double layer capacitors (EDLCs) and (b) Pseudocapacitors.

Chapter 2.2.3. Nanostructured materials for pseudocapacitors

Nanostructured materials have attracted great interest in recent years because they offer short path lengths for both electron and ion transport. Moreover, nanoscale materials have a high surface-to-volume ratio which enables higher utilization of the electrochemically active material by the electrolyte.^[21] These nano-size effects have been investigated with various pseudocapacitive materials including RuO₂ and MnO₂, which are among the best materials in this field. RuO₂ (dia.~38 nm) was first reported to have a specific capacitance of 720 F/g^[22]. The capacity of RuO₂ increases dramatically when the size of particle decreases to 3 nm, up to 1340 F/g, which is close to its theoretical capacity (1358 F/g)^[23]. In addition to RuO₂, studies on the pseudocapacitive behavior of MnO₂ indicate that thin films (tens to hundreds of nanometers thick) give rise to high specific capacitances, of up to 1380 F g⁻¹^[6]. This value is much larger than that of micrometer-thick films, 150-250 F/g^[24, 25].

Another interesting feature of nano-dimensional materials is that the capacitive contribution at the surface becomes larger as the particle size decreases. Dunn *et al.*^[26] demonstrated that the total stored charge in TiO₂ increases as the particle size decreases due to the increase of the capacitive contribution (e.g. 55% for 7nm and 15% for 30nm of particles) despite the fact that the capacity contributed by Li ion insertion for smaller particles is less than that of large particles. This higher capacitive contribution enables us to have faster charge/discharge rates, which leads higher power as well.

Chapter 2.3. Experimental

Nanoscale Nb₂O₅ particles having different crystalline structures and surface areas were synthesized via either aqueous or non-aqueous sol-gel processes. Niobium chloride (NbCl₅), benzyl alcohol (anhydrous), ethanol (≥99.5%) and propylene oxide (≥99%) were purchased from Sigma-Aldrich. All the chemicals were used without further purification.

Chapter 2.3.1. Synthesis of Nb₂O₅

Amorphous aerogel and orthorhombic T-Nb₂O₅

Both amorphous and T-Nb₂O₅ were synthesized using an aqueous sol-gel technique. Anhydrous NbCl₅ (2.56 mmol) was dissolved in ethanol (2 mL) while a solution of DI water (0.23 mL) in ethanol (2 mL) was prepared in a separate vial. Both solutions were cooled in an ice bath for 2 hours in order to prevent uncontrolled hydrolysis and condensation which leads to precipitate rather than gel formation. The two solutions were then mixed together while propylene oxide (~1 mL) was slowly injected with magnetic stirring until a transparent gel formed. The Nb₂O₅ wet-gel was aged for 1 day to promote network formation before being immersed in acetone, which was replaced periodically for 5 days before the gel was supercritically dried using CO₂.^[27] The resulting amorphous Nb₂O₅ aerogel was calcined at 400°C in air for 2 hours to remove any remaining adsorbed water and organics. This treatment did not crystallize the material. To produce the T-Nb₂O₅ phase the amorphous aerogel was annealed at 600°C for 2 hrs in air.

Pseudohexagonal TT-Nb₂O₅

A non-aqueous sol-gel technique was utilized for the synthesis of TT-Nb₂O₅.^[28] First, NbCl₅ (200 mg) was added to benzyl alcohol (20 mL). The mixture was then transferred into a Teflon cup containing a 45 mL inner volume, slid into a steel autoclave and carefully sealed. All these steps were performed in an Ar-filled glovebox. The sealed autoclave was removed from the glovebox and placed in an oven at 220°C for 4 days. The resulting cloudy suspensions were centrifuged (5000 rpm for 10 minutes) to separate the precipitates which were then washed thoroughly with ethanol and dichloromethane and dried at 60°C. The structure and electrochemical properties of the as-synthesized TT-Nb₂O₅ samples were used without any further heat treatment.

Chapter 2.3.2. Material Characterization

The phase of each Nb₂O₅ sample was identified using a powder X-ray diffractometer (PANalytical, X'PertPro) using Cu-K α ($\lambda=1.54$ Å) radiation. Brunauer-Emmett-Teller (BET) surface areas were obtained from nitrogen adsorption isotherms at 77 K using a gas adsorption analyzer (Micromeritics ASAP 2010). The particle size and crystalline nature of Nb₂O₅ were further characterized by transmission electron microscopy (TEM; CM 120, FEI) and high resolution transmission electron microscopy (HR-TEM; TITAN S/TEM, FEI). Different metal (Nb)-oxygen (O) bondings for various phases were characterized using Raman Spectroscopy (Renishaw inVia with 514 laser).

Chapter 2.3.3. Electrochemical characterization

Electrochemical measurements were performed in a three-electrode cell with a nanoparticle film of Nb_2O_5 serving as the working electrode. To prepare the working electrode, nanoscale sized powders of Nb_2O_5 aerogel or the crystalline phases ($\sim 20 \mu\text{g}$) were cast from an ethanol solution onto an oxygen-plasma treated stainless steel foil ($\sim 1 \text{ cm}^2$ area), which was subsequently heated at 110°C for one hour to evaporate the ethanol. The mass of the nanoparticles deposited on the stainless steel foil was determined using a microbalance. The electrolytes used were LiClO_4 (1 M) or NaClO_4 (1 M) in propylene carbonate. Lithium or sodium metal foils were used as the counter and reference electrodes. Cyclic voltammetry was performed between 1.2 and 3 V vs. Li/Li^+ (or Na/Na^+) using a PAR EG&G 273A Potentiostat. All tests were performed in an argon glovebox, with oxygen and water levels of $< 1 \text{ ppm}$. For the *ex-situ* HR-TEM experiment, *T*- Nb_2O_5 particles were deposited directly on a copper TEM grid which served as the working electrode. After the electrochemical measurements, the sample could be placed directly into the HR-TEM.

Chapter 2.4. Results and Discussion

Chapter 2.4.1. Nb_2O_5 synthesis and characterization

The phases of Nb_2O_5 examined in this study are amorphous, pseudohexagonal (*TT*- Nb_2O_5) and orthorhombic (*T*- Nb_2O_5). The amorphous and *T*-phase Nb_2O_5 were synthesized by heat treatment of Nb_2O_5 aerogel precursor prepared by an aqueous sol-gel route. The sol-gel

process typically includes hydrolysis of the precursor, usually metal alkoxide or metal salt, and poly-condensation between the pre-hydrolyzed precursors (Figure 2.5).

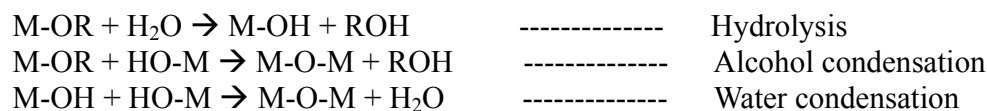


Figure 2.5. Sol-gel process of metal alkoxide

However, in this study, propylene oxide is also involved in the reaction. This reaction, called the epoxide-mediated sol-gel process, was first reported by Gash et al.^[29, 30] Using a stable metal salt, $NbCl_5$ as the starting material, homogeneous gelation can be triggered by the addition of epoxides. Epoxides act as proton scavengers through protonation of the epoxide oxygen and subsequent ring-opening reactions are brought about by the nucleophilic anionic conjugate base, such as Cl^- (Figure 2.6).^[29] This ring-opening reaction results in a moderate and uniform increase in solution pH and eventually promotes the homogeneous hydrolysis and condensation reactions that produce a monolithic gel. Aging a gel before drying helps to strengthen the network and thereby reduce the risk of fracture. Finally, supercritical drying was performed using CO_2 to convert the aged wet-gel to an aerogel. During supercritical drying, the pore liquid phase is converted to gas without passing through its equilibrium phase and thus one can keep the pore structure and high surface area of the wet gel. Using this epoxide-mediated sol-gel process followed by supercritical drying, Nb_2O_5 aerogel was successfully fabricated and used as a precursor material for amorphous and orthorhombic $T-Nb_2O_5$.

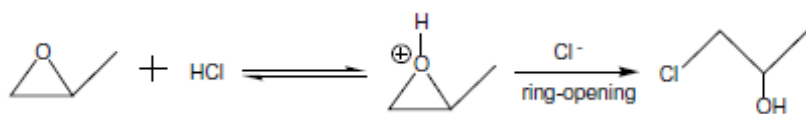


Figure 2.6. Ring-opening reaction of propylene oxide with acid^[31]

Pseudo-hexagonal $TT\text{-Nb}_2\text{O}_5$, on the other hand, was synthesized using a nonaqueous solvothermal sol-gel process. The use of the nonaqueous (or nonhydrolytic) sol-gel process in organic solvents overcomes some limitations of aqueous systems (e.g. the difficulty in preparing nanocrystalline materials). The different products that result from the nonaqueous sol-gel process are caused by the slow reaction rates, which are mainly a consequence of the moderate reactivity of the C–O bond. The stabilizing effect of the organic species in non-aqueous sol-gel processes leads to the formation of nanosized, uniform and highly crystalline materials.^[32] Due to the absence of water and the use of NbCl_5 as a precursor in this study, the only oxygen available for oxide formation is provided by the solvent, benzyl alcohol. Metal-oxygen-metal bonds can be formed through one of the condensation steps, as shown in Figure 2.7.

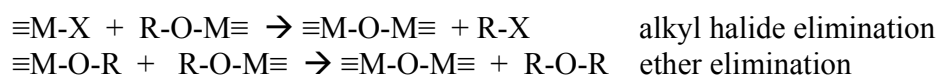


Figure 2.7. Condensation steps for non-aqueous sol-gel process based on reacting metal halides in benzyl alcohol^[32]

The phase and morphology of the Nb_2O_5 materials were characterized using X-ray diffraction (XRD) and transmission electron microscopy (TEM). XRD patterns for each of the Nb_2O_5 phases synthesized are shown in Figure 2.8. As-synthesized Nb_2O_5 aerogel is amorphous

and has a BET surface area of 442 m²/g (Table 1). After calcination at 400 °C to dehydrate the structure, the Nb₂O₅ is still amorphous (Figure 2.8-(a)) but the BET surface area is reduced to 187 m²/g (Table 1). Heating as-synthesized Nb₂O₅ aerogel to 600°C in air leads to *T*-Nb₂O₅ (JCPDS 30-873), as shown in Figure 2.8-(c). Figure 2.8-(b) shows that *TT*-Nb₂O₅ (JCPDS 28-317) is synthesized through a non-aqueous solvothermal sol-gel process without heat treatment. The formation of *TT*-Nb₂O₅ is due to its low synthetic temperature (220 °C) compared to 600 °C for *T*-Nb₂O₅.^[16] XRD patterns of *T*- and *TT*- phases of Nb₂O₅ are similar except for a peak shift around 28° (2 theta) and two small additional peaks around 42° and 45° (2 theta). This is because *TT*-Nb₂O₅ is believed to be a defect structure of *T*-Nb₂O₅. The main difference between the two phases is that in the *TT* phase, some oxygen atoms of the *T*-Nb₂O₅ are replaced by impurities such as Cl⁻ (from residual precursor) or vacancies.^[16] The BET surface areas of *T*- and *TT*-Nb₂O₅ phases are 70 and 149 m²/g, respectively (Table 1).

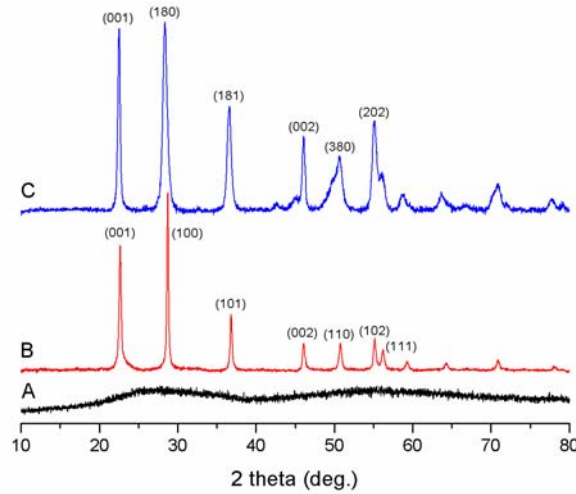


Figure 2.8. X-ray diffraction patterns for different phases of Nb₂O₅: a) dehydrated amorphous Nb₂O₅ aerogel, b) pseudohexagonal (*TT*-Nb₂O₅), c) orthorhombic (*T*-Nb₂O₅).

Table 2.1. Brunauer-Emmett-Teller (BET) surface areas for different phases of Nb₂O₅ nanoparticles.

| | As-synthesized Nb ₂ O ₅ aerogel (Amorphous) | Dehydrated Nb ₂ O ₅ aerogel (Amorphous) | <i>T</i> -Nb ₂ O ₅ | <i>TT</i> -Nb ₂ O ₅ |
|--------------------------------------|---|---|--|---|
| BET surface area [m ² /g] | 442 | 187 | 70 | 149 |

TEM images of the Nb₂O₅ particles synthesized in this work show the different sizes and morphologies for the various phases (Figure 2.9). For as-synthesized aerogel, all the small particles are connected to each other leading to a three-dimensional network structure (Figure 2.9-(a)). After annealing at 400°C, the particles size increased to ~10 nm and the particles formed aggregates (Figure 2.9-(b)). The particle size was further increased for *T*-Nb₂O₅ (35 nm-Figure 2.9-(d)) due to higher annealing temperature (600°C). Figure 2.9-(c) shows that *TT*-Nb₂O₅ synthesized via non-aqueous sol-gel process are slightly agglomerated and the average particle size is 7 nm.

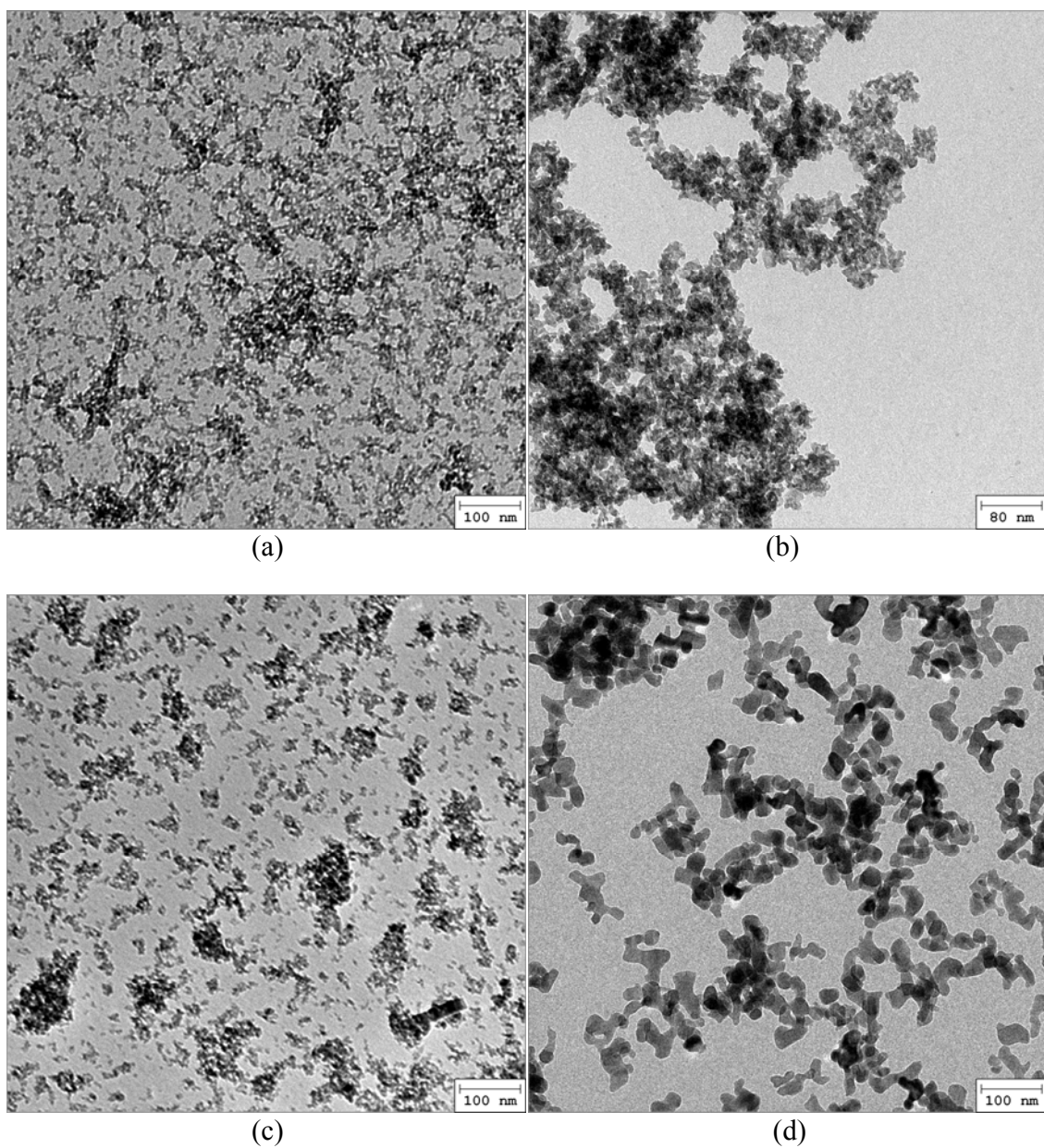


Figure 2.9. Transmission electron microscopy (TEM) images for the different Nb_2O_5 phases: a) as-synthesized Nb_2O_5 aerogel, b) dehydrated Nb_2O_5 aerogel, c) pseudohexagonal ($TT\text{-Nb}_2\text{O}_5$), d) orthorhombic ($T\text{-Nb}_2\text{O}_5$).

The bonds between niobium and oxygen in each Nb₂O₅ phase were characterized using Raman spectroscopy. As shown in Figure 2.10, as-synthesized Nb₂O₅ has two broad peaks around 837 and 647 cm⁻¹ where are attributed to stretching mode of Nb=O on the surface and the stretching mode of slightly distorted Nb-O in polyhedra (NbO₆, NbO₇ and NbO₈), respectively. Those two peaks are characteristic for non-crystalline Nb₂O₅.^[33] For crystalline Nb₂O₅, there is a peak in a range of 580 – 740 cm⁻¹ which is caused by Nb-O-Nb bridging bond of distorted NbO₆.^[34] However, the peak position changes slightly as different temperatures are applied for different phase of Nb₂O₅. Peaks at a range of 180-350 cm⁻¹ correspond to Nb-O-Nb angle deformation.^[34] As shown in Figure 2.10, the peaks for Nb-O-Nb becomes split for *T*-Nb₂O₅ (600 °C and 800 °C) and *H*-Nb₂O₅, which is not shown in as-synthesized or pseudohexagonal Nb₂O₅. For monoclinic *H*-Nb₂O₅ which is formed by heating as-synthesized Nb₂O₅ at 1000 °C, a strong peak at 997 cm⁻¹ starts to be shown. This characteristic peak is attributed to stretching mode of Nb=O due to strong distortion of NbO₆ by heat treatment at high temperature.^[16] However, when Nb₂O₅ is heat treated above 800 °C, the particle size was dramatically increased. Figure 2.11 shows that particle size is over 200 nm (in dia.) when Nb₂O₅ was heat treated at 800 °C. Because the samples heat treated at above 800 °C are no longer nanoscale, they were excluded from the characterization study.

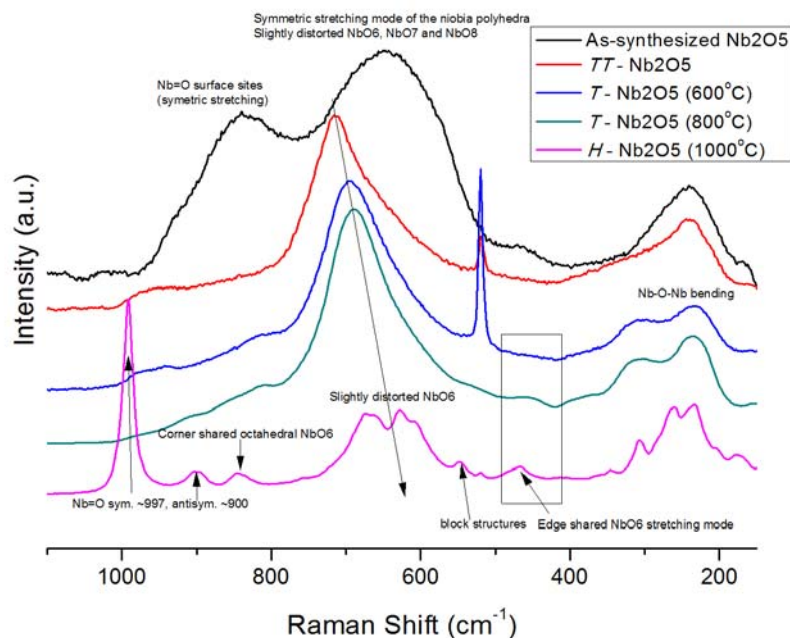


Figure 2.10. Raman spectra of Nb_2O_5 with different crystalline structure; A peak at 520 cm^{-1} is caused by Si substrate which was used for measurement

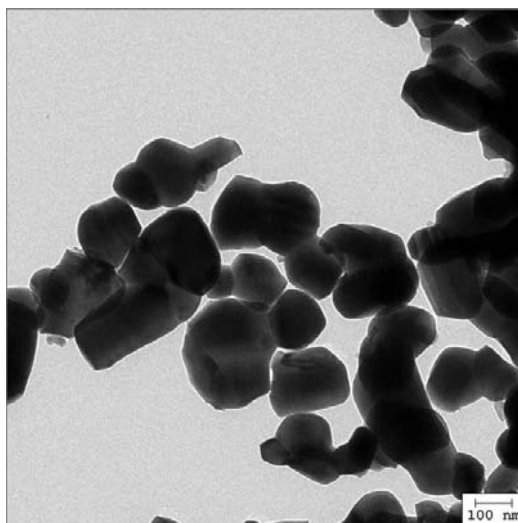
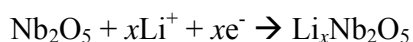


Figure 2.11. TEM image of Nb_2O_5 heat treated at $800\text{ }^\circ\text{C}$ for 2 hrs in air; Nb_2O_5 aerogel synthesized in this study was used as a precursor material

Chapter 2.4.2. The effect of crystallinity on pseudocapacitive behavior of Nb₂O₅

The charge storage properties were investigated in 3-electrode cells using lithium (or sodium) as the counter and reference electrodes. The stainless steel substrate used for the thin film electrodes contributed little to the overall current (Figure 2.12). Cyclic voltammetry (CV) with lithium and sodium-ion electrolytes (1 M LiClO₄ or NaClO₄ in propylene carbonate) was used to determine the electrochemical properties of the Nb₂O₅ nanoparticles. For Nb₂O₅ in a lithium ion electrolyte, charge storage occurs through the insertion of lithium ions with concomitant reduction of Nb⁺⁵ to Nb⁺⁴, for a maximum theoretical storage of $x = 2$ (or 726 C/g)^[35].



In order to investigate the capacitive properties of Nb₂O₅, sweep rates were varied from 5 to 100 mV/s. For a typical range of 1.2 V, these conditions corresponded to a charge/discharge time between 12 seconds and 4 minutes.

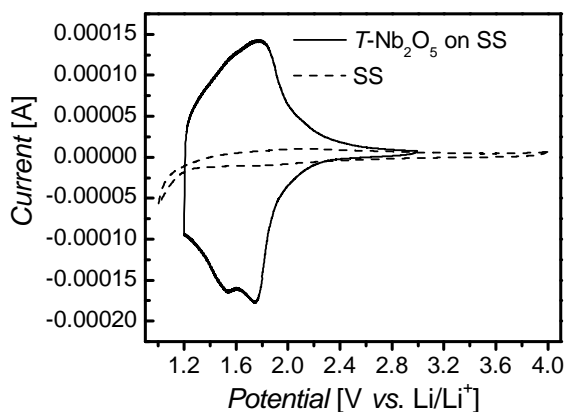


Figure 2.12. Voltammetric sweeps (10 mV/s in 1 m LiClO₄ in propylene carbonate) demonstrate that the stainless steel substrate (SS) contributes very little to the total current.

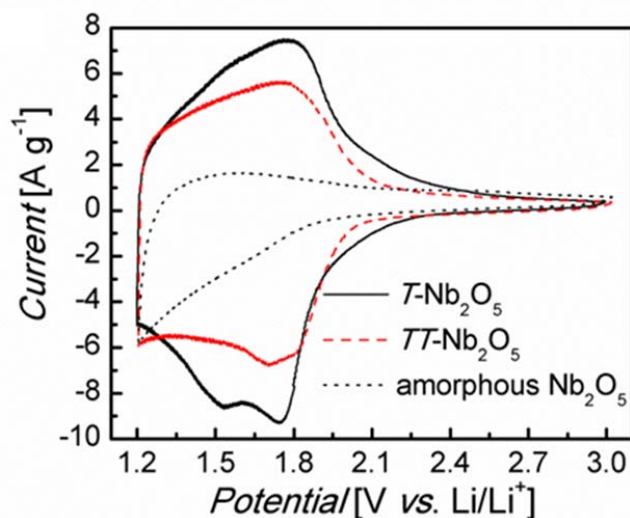


Figure 2.13. Voltammetric sweeps for Nb_2O_5 in lithium ion electrolyte: CVs at 10 mV/s for different Nb_2O_5 phases.

The crystalline phases of Nb_2O_5 exhibit much greater levels of charge storage compared to the amorphous material. The CVs in Figure 2.13 show that for the crystalline materials, the current response increases dramatically below 2.2 V vs. Li/Li^+ , giving rise to several broad cathodic peaks around 1.75 V and 1.5 V (for the orthorhombic phase). During lithiation, the electrodes exhibit blue coloration, demonstrating the well-known electrochromic property of crystalline Nb_2O_5 .^[36] On sweep reversal, identification of anodic peaks for the Nb_2O_5 is more difficult, with two very broad peaks apparent at about 1.5 V and 1.8 V for $T\text{-Nb}_2\text{O}_5$. Based on the small difference between insertion and deinsertion peak voltages, the lithiation process is highly reversible in nanocrystalline Nb_2O_5 . The scans shown in Figure 2.13 cover the range between 3.0 and 1.2 V (vs. Li/Li^+) and establish the absence of any redox peaks above 2.4 V. In fact, it is possible to scan between 2.4 V and 1.2 V to obtain the redox behavior shown in Figure 2.13. The

amorphous aerogel material does not show any peaks in the CV scan and the specific current is significantly lower than either of the crystalline materials. Amorphous Nb_2O_5 has been shown to have lower lithium capacity than crystalline Nb_2O_5 in mesoporous and sol-gel films as well.^[9, 13] Instead of the blue coloration seen in the crystalline materials, amorphous Nb_2O_5 exhibits a brown color during lithiation because of strong absorption in the blue.^[37]

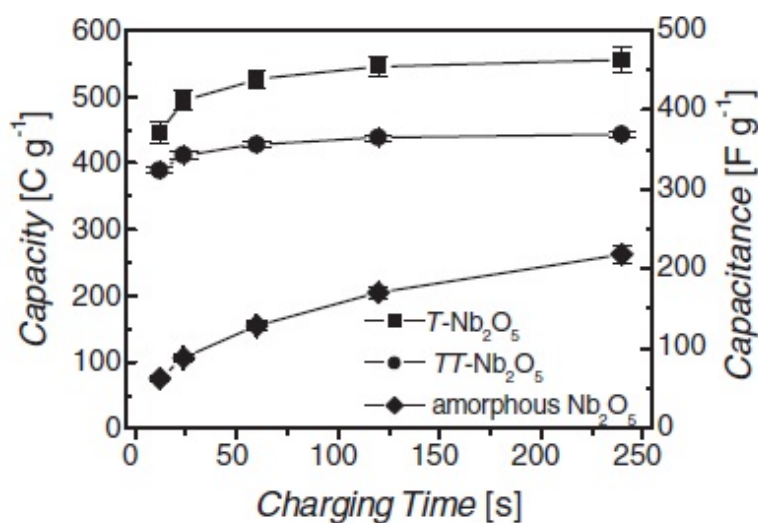


Figure 2.14. Charge storage as a function of charging time for different Nb_2O_5 phases

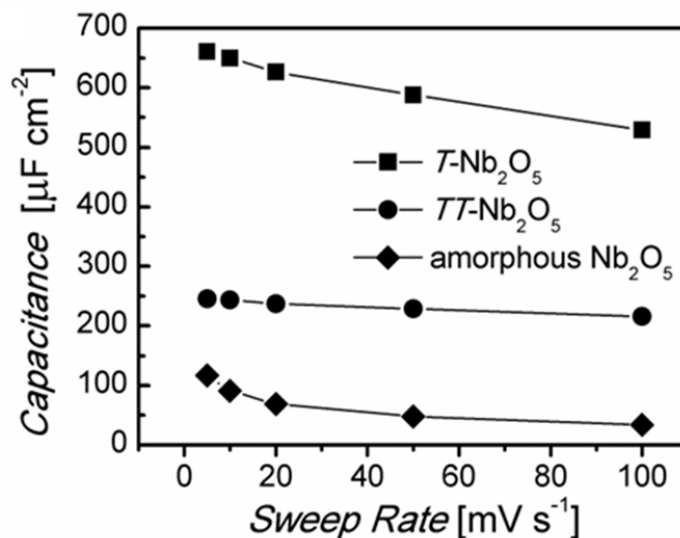


Figure 2.15. The surface-area normalized capacitance for different Nb₂O₅ phases in Li⁺ electrolyte

The kinetics of charge storage are influenced significantly by crystallizing Nb₂O₅. The differences between the crystalline and amorphous materials are quantified in Figure 2.14 and Figure 2.15 based on a voltage window of 1.2 V. The highest capacity is achieved with the *T*-Nb₂O₅: at a charging time of only 12 seconds the capacity is approximately 450 C/g, corresponding to a capacitance of 370 F/g. As charging time increases, the capacity increases until a consistent value of 560 C/g is attained after about 2 minutes. The fact that over 80% of the capacity is accessed within 12 seconds indicates that the kinetic response for *T*-Nb₂O₅ is one of the fastest reported for transition metal oxides. The *TT*-phase also shows significant charge storage, but this value is lower than the *T*-phase material, despite the fact that the surface area of the *TT*-Nb₂O₅ (149 m²/g) is significantly larger than that of the *T*-Nb₂O₅ (70 m²/g). The observation that surface area has limited effect on total charge storage was reported for MnO₂

polytypes^[8] and thus seems to be a characteristic of systems in which charge storage is faradaic and particle size is sub-micron. In contrast, the amorphous Nb₂O₅ aerogel has a significantly lower specific capacitance than either crystalline phase even though its surface area (187 m²/g) is actually higher than *TT*-Nb₂O₅. The great difference between the amorphous and crystalline phases shown in Figure 2.14 and Figure 2.15 is a good indication of how faradaic processes lead to an additional capacitive storage mechanism which does not occur with the non-crystalline material. Moreover, as indicated by the kinetic response, this faradaic contribution occurs at very short timescales where diffusion-related processes are expected to be minimal.

Chapter 2.4.3. Intercalation pseudocapacitance and structural stability of Nb₂O₅

Ex situ HR-TEM was used to investigate the ion intercalation and the structural stability of *T*-Nb₂O₅ during high-rate (100 mV/s) lithium insertion and extraction. To obtain the lithiated and delithiated *T*-Nb₂O₅, the cycling was stopped at 1.2 V and 3 V (vs. Li/Li⁺), respectively. Figure 2.16-(a) displays the lattices of *T*-Nb₂O₅ prior to the CV cycles. The lattice parameter (3.157 Å) in Figure 2.16-(a) corresponds to the (180) plane of *T*-Nb₂O₅, which is not present in *TT*-Nb₂O₅. This lattice parameter analysis is in good agreement with XRD pattern (Figure 2.8-(c)). Figure 2.16-(b) shows that the lattice parameter (3.25 Å) of *T*-Nb₂O₅ after lithiation was slightly larger than the lattice parameter (3.157 Å) of the pristine (180) plane. This indicates that the lattice parameter of the (180) plane is increased by 3% due to lithium insertion, which is in good agreement with prior XRD studies on lithium insertion into *T*-Nb₂O₅.^[38] The prior results of Kumagai and the study involving iso-oriented mesoporous films suggest that the (180) plane

of $T\text{-Nb}_2\text{O}_5$ may provide a favorable pathway for Li^+ transport.^[9] Upon delithiation, there is no evidence of a phase change. The HR-TEM image shown in Figure 2.16-(c) corresponds to the (001) plane of $T\text{-Nb}_2\text{O}_5$. Electron diffraction was also performed on each sample to investigate structure change during CV cycles. Figure 2-17 shows that all three samples have (180) and (181) plane, which are characteristic for orthorhombic $T\text{-Nb}_2\text{O}_5$. Electron diffraction analysis as well as d-spacing studies of HR-TEM images indicate that the structure of $T\text{-Nb}_2\text{O}_5$ did not change after 10 cycles of lithium insertion and extraction. In addition, Figure 2.16-(b) and 2.16-(c) demonstrate that a solid electrolyte interphase (SEI) layer was formed on the surface of Nb_2O_5 as expected from the use of low potentials during cycling.

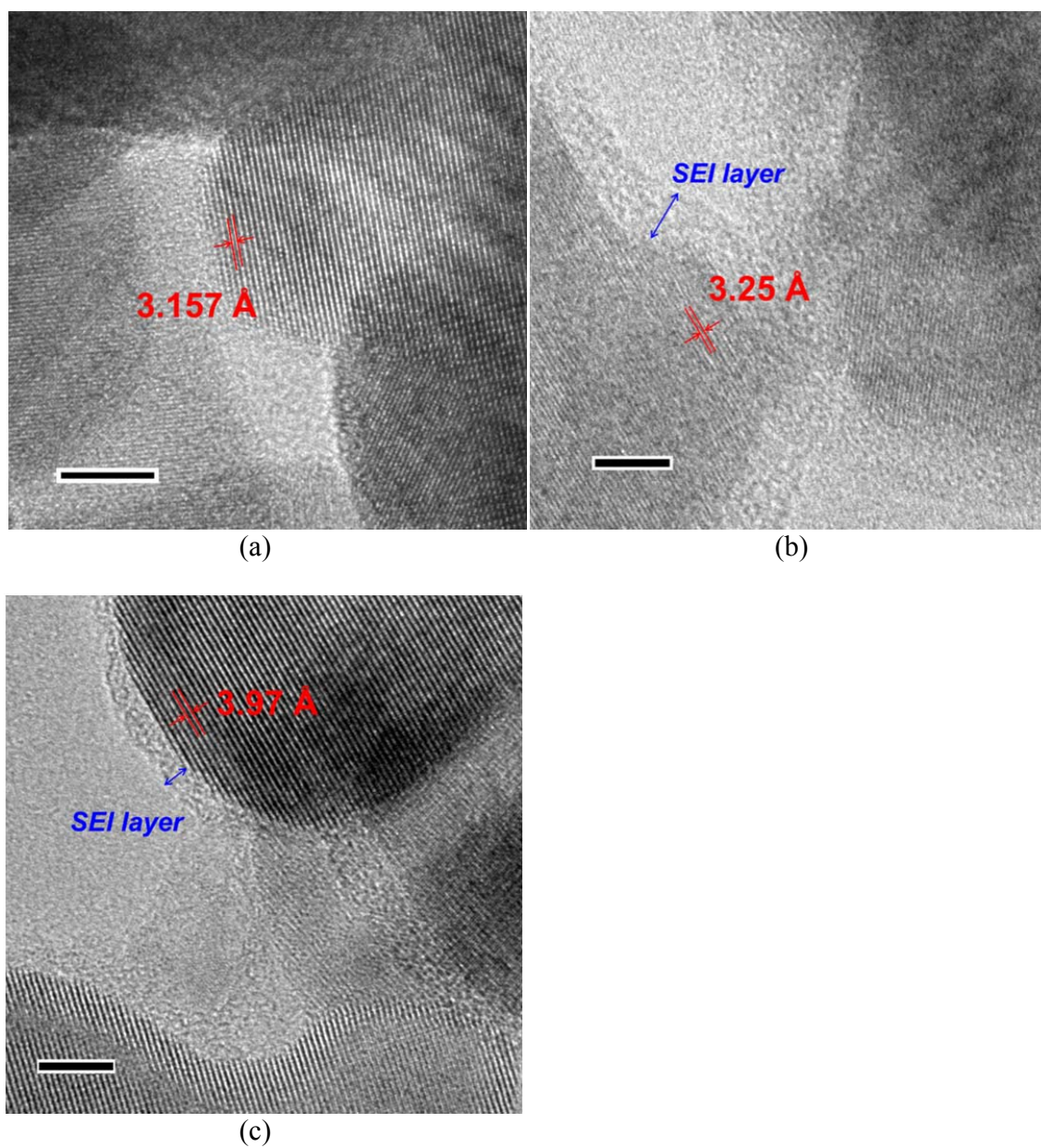


Figure 2.16. HR-TEM images of $T\text{-Nb}_2\text{O}_5$: a) pristine material, b) lithiated to 1.2 V (vs. Li/Li^+), c) delithiated to 3 V (vs Li/Li^+) after cycling 10 times at 100 mV/s. (scale bar: 5nm)

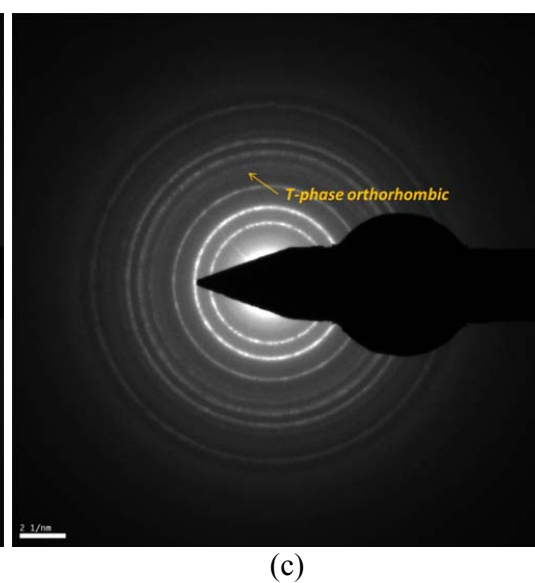
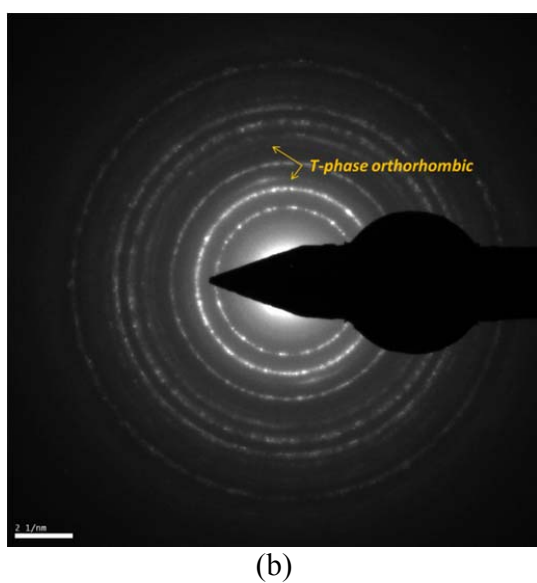
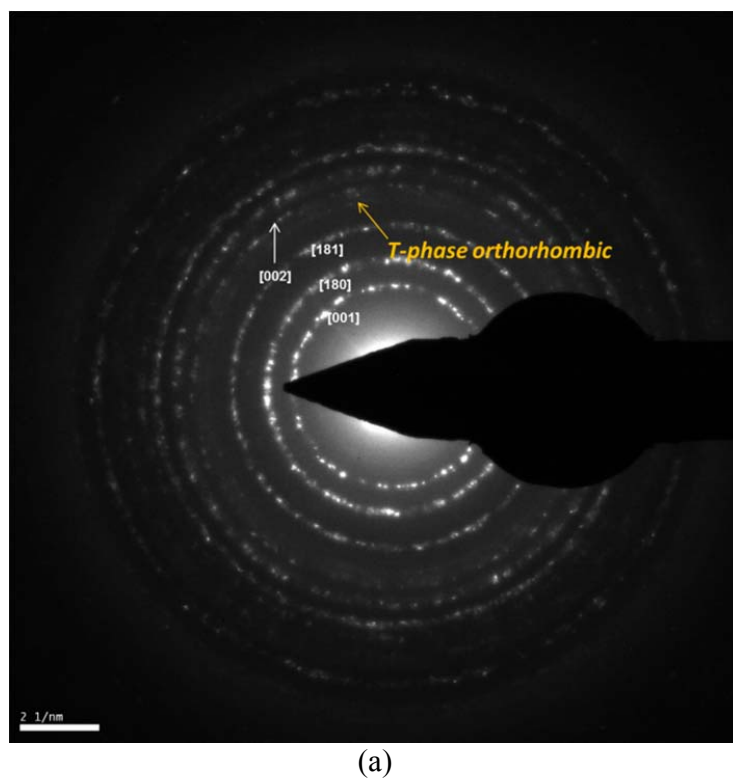


Figure 2.17. Electron diffraction (ED) studies of $T\text{-Nb}_2\text{O}_5$: a) pristine material, b) after lithiation, c) after delithiation. The orthorhombic phase of $T\text{-Nb}_2\text{O}_5$ is maintained after lithium insertion and deinsertion. (scale bar: 2 1/nm)

Chapter 2.4.4. Electrolyte ion size effect

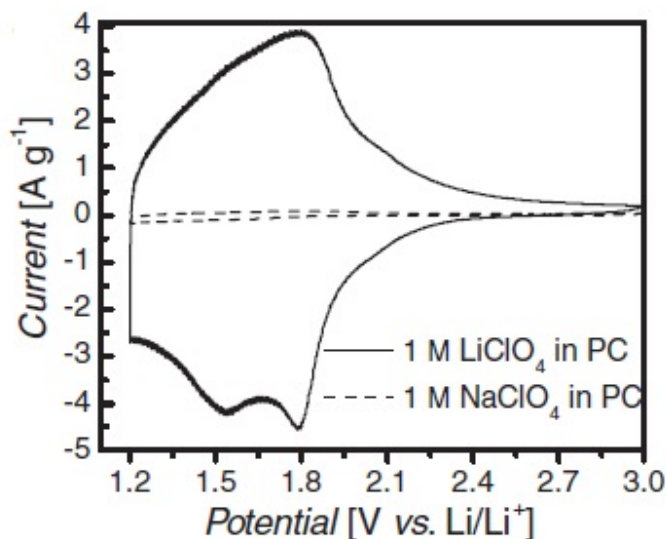


Figure 2.18. Effect of electrolyte ion size on electrochemical behavior of Nb_2O_5 : CV at 5 mV/s for $T\text{-Nb}_2\text{O}_5$ using Li^+ (—) or Na^+ (---) electrolytes.

The crystallographic dependence observed for Li^+ charge storage led us to consider the effect of ion size. To investigate the electrolyte ion size effect on charge storage of Nb_2O_5 , two different ions (Li^+ : 0.74 Å and Na^+ : 1.02 Å in rad.)^[39] were tested in this study. The results shown in Figure 2.18 for the $T\text{-Nb}_2\text{O}_5$ are quite dramatic as substantially greater current occurs using the lithium-ion electrolyte as compared to the sodium ion electrolyte. Surface area-normalized capacitance (Figure 2.19) shows that with the sodium-ion electrolyte, the amount of charge storage does not depend on crystallinity or phase. The measured value of 20 F/cm² is a level generally associated with double-layer capacitance.^[4] If capacitive energy storage using the sodium electrolyte occurs only from electrical double layer contributions, it is expected that the

specific capacity increases with surface area. Thus, because of its greater surface area, it is not surprising that the amorphous Nb_2O_5 aerogel exhibits a larger gravimetric capacity ($\sim 40 \text{ C/g}$ at 5 mV/s ; Figure 2.20) than that of crystalline phases. And it is also reasonable that capacity values normalized by surface area for each phase of Nb_2O_5 are similar each other (Figure 2.21). This behavior is very different from what is observed when using lithium electrolytes. Because of charge storage from faradaic reactions, the surface-area normalized capacitance of the crystalline materials in lithium-ion electrolyte is at least an order of magnitude larger than in sodium for all sweep rates (Figure 2.15). The inability for the larger Na^+ to move within the frameworks of the TT - and T - Nb_2O_5 phases was reported by Kumagai *et al.*^[40] and is a commonly observed feature for other intercalation compounds.^[41]

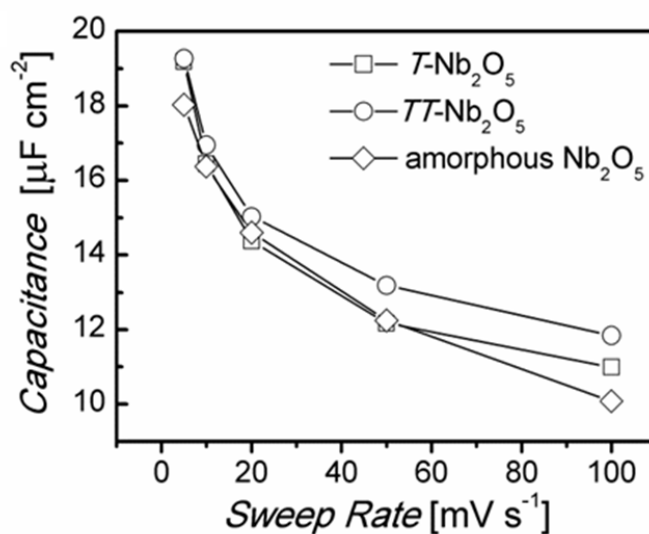


Figure 2.19. The surface-area normalized capacitance for different Nb_2O_5 phases in Na^+ electrolytes

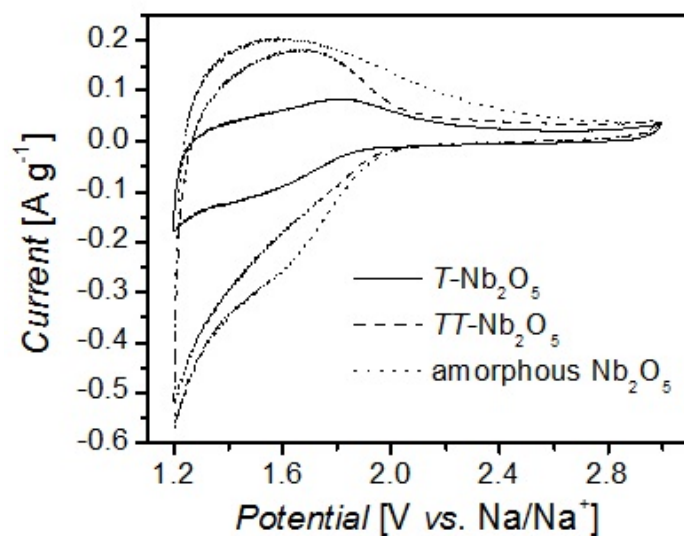


Figure 2.20. Voltammetric sweeps for Nb_2O_5 materials in sodium ion electrolyte (1 M NaClO_4 in propylene carbonate). Current is normalized by weight.

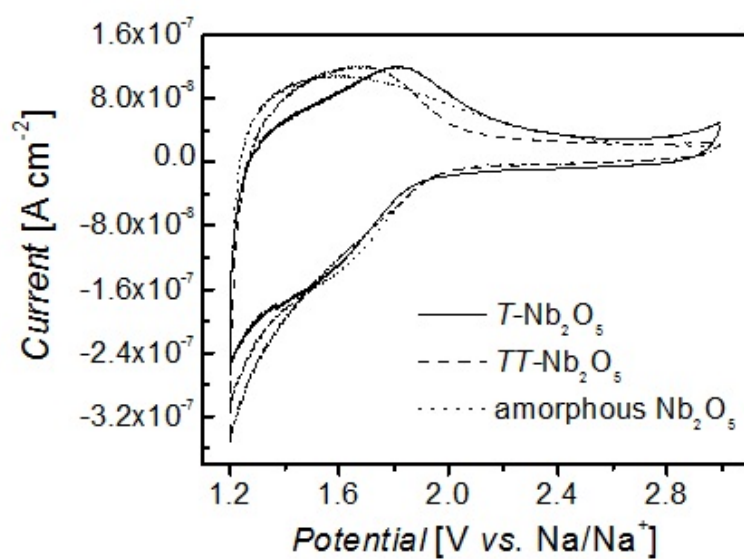


Figure 2.21. Voltammetric sweeps for Nb_2O_5 materials in sodium ion electrolyte (1 M NaClO_4 in propylene carbonate). Current is normalized by surface area.

Chapter 2.4.5. Kinetic behavior of T-Nb₂O₅

To obtain further insight concerning the kinetics of charge storage in T-Nb₂O₅, we adapted an analysis first used by Trasatti *et al.* to characterize the charge storage of RuO₂, a well-known pseudocapacitive material.^[42] In this analysis, the overall capacity (Q) of a material is assumed to contain two contributions, that from capacitive charge storage (Q_{capacitive}, the “outer surface”) and that from bulk charge storage (Q_{bulk}, the “inner surface”):

$$Q = Q_{\text{capacitive}} + Q_{\text{bulk}}$$

The bulk charge storage depends upon ion diffusion and, assuming semi-infinite linear diffusion, is expected to vary as $t^{1/2}$. By rewriting the above equation in terms of the sweep rate (ν), the following relationship arises:

$$Q(\nu) = Q_{\text{capacitive}} + \text{constant}(\nu^{-1/2})$$

In this analysis, a plot of capacity vs. $\nu^{-1/2}$ yields a straight line whose y-intercept ($\nu = \infty$) is the “outer surface” capacity or the infinite-sweep rate capacity. Due to the possibility of polarization at high sweep rates, deviation from a straight line usually occurs, and intermediate sweep rates are then chosen to extrapolate to the y-intercept.^[43] The extrapolated infinite sweep-rate capacitance for T-Nb₂O₅ (Figure 2.22) is estimated to be around 400 F/g, in good agreement with the charging behavior shown in Figure 2.14. This value represents the amount of charge

storage from capacitive processes, namely double-layer and/or pseudocapacitance. At slower sweep rates, diffusion-related processes begin to contribute and the total amount of charge storage becomes a combination of capacitive and diffusion components. In some materials, diffusion-related charge storage increases significantly and far outweighs the capacitive contribution. In the case of TiO_2 nanoparticles, for example, diffusion processes contributed between 85% and 45% of the total amount of charge storage depending upon crystallite size.^[26] What is particularly interesting with Nb_2O_5 is that even at slow sweep rates and reasonably large crystallite sizes (30-40 nm), diffusion processes contribute only a small amount of the total charge, less than 20% at 5 mV/s (Figure 2.23).

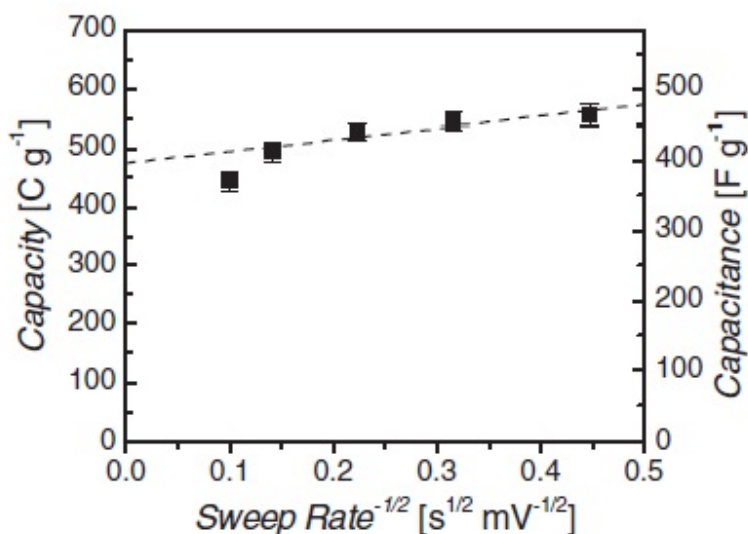


Figure 2.22. Determination of the infinite sweep-rate capacitance of $T\text{-Nb}_2\text{O}_5$: the capacity as a function of sweep rate^{-1/2}, the y-intercept is 470 C/g and represents the infinite sweep rate capacity

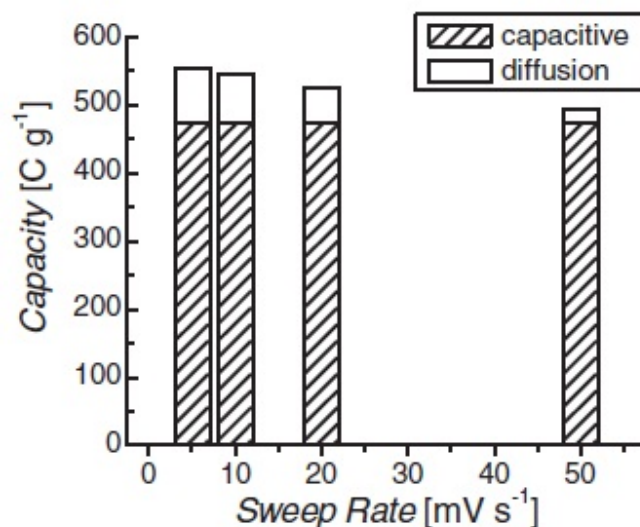


Figure 2.23. The contribution of the capacity at infinite sweep rate to the total charge storage

To provide some context for the extrapolated infinite sweep-rate capacitance, it is useful to make comparisons with both birnessite MnO_2 and RuO_2 . Using non-aqueous lithium electrolytes similar to the experiments reported here, the results from Ma *et. al.* indicate a specific capacitance for birnessite of $\sim 270 \text{ F/g}$.^[44] This is well below the 400 F/g shown in Figure 2.22 for $T\text{-Nb}_2\text{O}_5$. Direct comparisons with RuO_2 are not feasible for these electrolytes because crystalline anhydrous RuO_2 undergoes a phase transition upon lithiation.^[45] With acid electrolytes, however, there is considerable experimental data. Recent results reported for 2 nm-thick RuO_2 nanoskins exhibited an infinite-sweep rate specific capacitance of $\sim 480 \text{ F/g}$.^[46] Thus, even though the pseudocapacitance mechanisms are different for RuO_2 and $T\text{-Nb}_2\text{O}_5$, their charge storage kinetics at short times are quite comparable. In some respects, RuO_2 , which has been investigated since the 1970's, represents a model pseudocapacitor system. Its high

electronic and ionic conductivity have been proposed as the key factors in achieving high specific capacity.^[47] Nb_2O_5 , on the other hand, is an electronic insulator; its bulk resistivity is $\sim 3 \times 10^4 \text{ } \Omega\text{-cm}$ at 300K with a bandgap of $\sim 3.4 \text{ eV}$.^[14, 15] However, the insertion of lithium into the structure apparently dopes the material and increases the electronic conductivity. Electrochemical impedance measurements of $T\text{-Nb}_2\text{O}_5$ samples before and after lithiation (Figure 2.24) indicate that the charge transfer resistance decreases by a factor of about 1000 after lithiation. The mixed electronic and ionic conduction of reduced $T\text{-Nb}_2\text{O}_5$ was noted previously.^[35] Despite the dramatic improvement in electrical properties with lithiation, for device applications that use thicker electrodes, it is likely that conductive additives would still be necessary.

The question of how electronic conduction develops in lithiated Nb_2O_5 has been considered by several research groups. Orel *et al.* proposed that electron transport occurs due to a polaron hopping mechanism and showed that the conductivity increases by four orders of magnitude when Nb_2O_5 is chemically-lithiated.^[13] Also relevant to the conductivity question is the fact that shear structures of reduced monoclinic Nb_2O_5 become conductive with as little as four atomic % Nb^{+4} due to the addition of $4d^1$ electrons to the insulating structure.^[14] Finally, a first-principles study of n-type doping in oxides suggested that Nb_2O_5 will become conductive once hydrogen is inserted into the lattice.^[48] While the results of these studies are not necessarily consistent, they do underscore the point that the addition of small cation dopants into the crystalline Nb_2O_5 lattice increases the electronic conductivity, perhaps substantially and at relatively low dopant levels. It would seem that the development of enhanced electronic

conductivity is of central importance in explaining why an insulator such as Nb_2O_5 exhibits a high rate pseudocapacitive response comparable to that of RuO_2 .

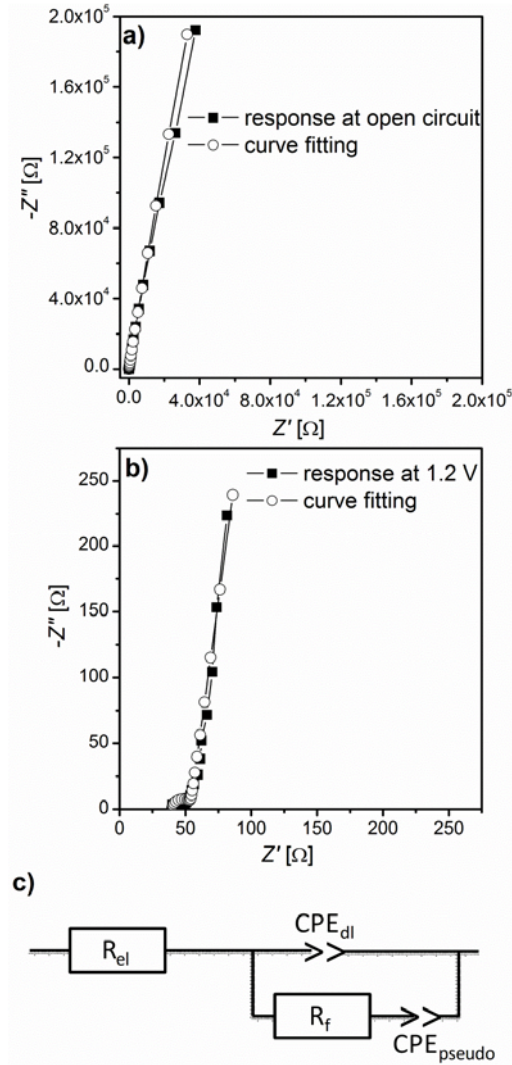


Figure 2.24. Nyquist representation of impedance spectra for the $T\text{-Nb}_2\text{O}_5$ nanocrystal electrode at two different potentials, before any lithiation at open-circuit (a), and (b) after lithiating to 1.2 V. The circuit model used for fitting is shown in (c), where R_{el} is the electrolyte resistance, CPE_{dl} is the double-layer capacitance present at all electrode/electrolyte interfaces, R_f is the faradaic charge transfer resistance, and CPE_{pseudo} is the pseudocapacitance. CPE is the constant phase element ($Z_{CPE} = [B(j\omega)^n]^{-1}$, where B and n are constants and ω is the frequency). Simulations indicate that R_f decreases on lithiation from 14.3 kohms to 15 ohms.

Chapter 2.5. Conclusion

The results in this chapter establish that the high specific capacitance observed with mesoporous iso-oriented films of Nb_2O_5 is, in fact, a fundamental property of this material. The significant difference between the crystalline and amorphous phases arises from the fast faradaic reactions that occur in crystalline Nb_2O_5 , leading to an additional pseudocapacitive storage contribution. The extrapolated infinite sweep rate capacitance of $\sim 400 \text{ F/g}$ exceeds that of birnessite MnO_2 and is comparable to values obtained for RuO_2 . Faradaic reactions in Nb_2O_5 occur over very short timescales and it is likely that Li^+ insertion occurs along preferred crystallographic pathways that provide an appropriate environment for fast ion transport. These pathways are apparently very size sensitive, as experiments with sodium electrolytes exhibit only double layer capacitance. The magnitude of electronic conductivity upon Li^+ insertion and the means by which electronic conduction develops in this wide band gap semiconductor remain to be addressed. The surprising ability of Nb_2O_5 to store charge at high rates despite its insulating character is unusual as compared to most transition metal oxides. This work suggests that in searching for advanced electrochemical capacitor materials, compounds that become highly conductive during ion intercalation represent an exciting direction for the future.

Chapter 3. Nb₂O₅/C core-shells for pseudocapacitors

Chapter 3.1. Introduction

Carbon is commonly used in nanostructures with pseudocapacitors to raise the conductivity of the composite material. Among the various types of nanocomposites reported on, oxides/CNT and oxides/graphene are the most well studied class of pseudocapacitive systems. Several papers indicate that those nanostructured pseudocapacitors deliver higher rate capability and/or capacity retention than bare oxides without a good electronic conductor, CNT or graphene^[49-52]. It should be noted that the remarkable pseudocapacitive performance of the composites is not only because of the increased conductivity of the electrode, but also because the contact area between electrochemically active materials (oxides) and the electrolyte are increased by dispersion of oxides on CNT or graphene. This enhancement is consistent with the mechanism for pseudocapacitance which occurs near and on the surface of the active material. Aside from blending in conductive material, the oxides/carbon core-shell structure may offer even better device performance. An important advantage of this morphology compared to the composites with CNT or graphene is that electrons can reach all the position where faradaic reaction occurs. Thus, with the core-shell structure, one can alleviate polarization phenomenon.

The core-shell structure has been widely used for lithium ion batteries (LIBs) to improve the conductivity of cathode and anode materials.^[53-60] Additional advantages of the core-shell structure are protecting the core material from HF generated by the electrolyte and restricting volume expansion.^[56] The morphologies of the core-shell structure are varied from 0D to 3D in the nano- to micro-meter scale.^[61] Both porous^[55] and dense^[54] carbon shells have been used for

LIBs as well as graphene^[58]. Recent studies on both anode and cathode materials for LIBs showed that higher rate capability and improved cycling stability can be obtained by having a carbon shell. For example, Zhang *et al.* showed that the anode material, Fe₃O₄ core with amorphous carbon shell, has higher reversible capacities (745 mAh/g at 0.2 C and 600 mAh/g at 0.5C) in the first cycle and significantly enhanced cycling performances and higher rate capabilities compared with bare magnetite (Fe₃O₄) particles.^[59] The discharge capacity of LiCoPO₄/C core-shell as a cathode material was maintained 72.6 mAh/g after 30 cycles at 0.1 C, compared to the (19.4 mAh/g) of bare LiCoPO₄. The enhancement of the carbon core shell continues even at higher charge/discharge rate (> 10C). For example, LiFePO₄/C core-shell has higher discharge capacity, 90 mAh/g, than that of bare LiFePO₄, 80 mAh/g at 60C^[57]. Rate capability of LiMn₂O₄ is also improved by having the carbon shell on the active material and LiMn₂O₄/C retained 47% of the initial capacity at 1C at the high rate of 300C^[53]. In general, most studies on core-shell structures for LIBs are based on low galvanostatic charge/discharge rate (< 1C) or slow sweep rate for cyclic voltammetry (< 0.1 mV/s) compared to those for supercapacitors.

In this chapter, the effect of core-shell structure on the pseudocapacitive behavior of niobium oxide (Nb₂O₅) was examined. As mentioned in chapter 2, orthorhombic Nb₂O₅ exhibits high specific capacitance at high rates, with nearly 400 F/g being stored reversibly within 12 seconds^[62]. In addition, the specific capacitance of Nb₂O₅ depends on the crystalline structure, not the surface area, indicating that charge is stored mainly through intercalation in Nb₂O₅. However, this result relied on small mass loading (~ 20 µg), thus its bulk resistivity (~ 3x10⁴ Ω-cm at 300K) with a bandgap of ~3.4 eV^[14, 15] would be challenge for its practical use. Nb₂O₅/C

core-shell was synthesized via *ex-situ* carbon coating on orthorhombic Nb₂O₅ using a microwave-assisted hydrothermal method. Electrochemical studies showed that as Nb₂O₅/C core-shell materials were heat-treated and oxidized, their capacity increased dramatically. Oxidation of Nb₂O₅/C core-shell, in particular, promotes transport of an electrolyte ion through the carbon shell while oxidized carbon still serves as a good electron path. In addition, most of the current from the oxidized Nb₂O₅/C core-shell is capacitive and has similar rate capability to bare Nb₂O₅ electrodes.

Chapter 3.2. Experimental

Chapter 3.2.1. Synthesis and oxidation of core-shells

Nb₂O₅/C core-shells

Nb₂O₅/C core-shell structure was fabricated via *ex-situ* carbon coating on *T*-Nb₂O₅ nanoparticles using a microwave-assisted hydrothermal (MW-HT) method. Synthesis of *T*-Nb₂O₅ was described in previous chapter (chapter 2.3). For the core-shell synthesis, the following were combined in DI water (20 mL) and sonicated for 1 hour; *T*-Nb₂O₅ (0.159 g), glucose (2 g) as a carbon source and polyethylene glycol (0.5 g) as a binder between Nb₂O₅ and carbon. After sonicating, the solution was transferred to the microwave heating system (Discover SP system, CEM) and hydrothermally reacted at 180 °C for 1 hr under magnetic stirring using the maximum microwave power of 200 W. As-synthesized Nb₂O₅/C particles were collected using centrifuge and washed with DI-water and ethanol several times until supernatant solution is clear. The sample was then dried at 60 °C in air. For further carbonization of the carbon shell,

the samples were heat treated at 700 °C under forming gas (5% hydrogen and 95% nitrogen) for 2hrs. This sample is referred to as Nb₂O₅/C-F700 in this chapter.

Oxidation of Nb₂O₅/C core-shell

Post oxidation process was performed on Nb₂O₅/C-F700 as follows. Nb₂O₅/C-F700 (0.1 g) was dispersed in 2 M nitric acid (HNO₃) (20 mL). This solution was then refluxed at 110 °C for 24 hrs. The resulting samples were washed with water and ethanol and collected by centrifuging. Finally, the samples were dried at 100 °C in vacuum.

Chapter 3.2.2. Material characterization

The phase of Nb₂O₅ in each core-shell sample was identified using a powder X-ray diffractometer (PANalytical, X'PertPro) using Cu-K α ($\lambda=1.54$ Å) radiation. Brunauer-Emmett-Teller (BET) surface areas were obtained from nitrogen adsorption isotherms at 77 K using a gas adsorption analyzer (Micromeritics ASAP 2010). The particle size of Nb₂O₅ and the thickness of the carbon shell were characterized by transmission electron microscopy (TEM; CM 120, FEI). The carbon content in each Nb₂O₅/C core-shell sample was determined using thermogravimetric analysis (TGA, SDT Q-600, TA instruments). Raman spectroscopy (Renishaw inVia with 514 laser) and Fourier transform infrared spectroscopy (FT-IR, FT-IR 670, JASCO) were utilized to characterize the carbon in Nb₂O₅/C core-shells. The oxidation state of niobium before and after the core-shell formation was verified using X-ray photoelectron spectroscopy (XPS, Kratos XPS Axis Ultra DLD).

Chapter 3.2.3. Electrochemical characterization

Electrochemical measurements were performed in a three-electrode cell with a nanoparticle film of $T\text{-Nb}_2\text{O}_5$ or $\text{Nb}_2\text{O}_5/\text{C}$ core-shells serving as the working electrode. To prepare the working electrode, the samples ($\sim 20\text{ }\mu\text{g}$ or $\sim 0.5\text{ mg}$) were cast from an ethanol solution onto an oxygen-plasma treated stainless steel foil ($\sim 1\text{ cm}^2$ area), which was subsequently dried at $60\text{ }^\circ\text{C}$ in air. Another type of working electrode was also fabricated by coating slurries containing either $T\text{-Nb}_2\text{O}_5$ or $\text{Nb}_2\text{O}_5/\text{C}$ core-shells (80 wt%), carbon black (10 wt%) and polyvinylidenedifluoride (PVDF, 10 wt%) dispersed in *N*-methylpyrrolidinone (NMP) onto stainless steel current collector ($\sim 1\text{ cm}^2$ area). These electrodes were dried at room temperature for 12 hrs followed by heating in a vacuum oven at $110\text{ }^\circ\text{C}$ for 3 hrs. The mass of the nanoparticles deposited on the stainless steel foil was determined using a microbalance. The electrolyte used in the experiment was LiClO_4 (1 M) in propylene carbonate. Lithium metal foils were used as the counter and reference electrodes. Cyclic voltammetry was performed between 1.2 and 3 V vs. Li/Li^+ using a PAR EG&G 273A Potentiostat in an argon glovebox, with oxygen and water levels of $< 1\text{ ppm}$. Impedance was also measured during the CV cycles using a frequency range of 1 to 10^5 Hz at $10\text{ mV}_{\text{rms}}$. To measure the double layer contribution in $\text{Nb}_2\text{O}_5/\text{C}$ core-shells, another CV was performed using tetraethylammonium tetrafluoroborate (1 M TEABF₄) in acetonitrile as electrolyte with Ag reference and platinum counter electrodes.

Chapter 3.3. Results and Discussion

Chapter 3.3.1. Synthesis and characterization of Nb₂O₅/C core-shell

Three different kinds of Nb₂O₅/C core-shells were synthesized and their electrochemical behaviors were studied. First, microwave heating was used in conjunction with hydrothermal synthesis to prepare an *ex-situ* carbon coating on the *T*-Nb₂O₅ nanoparticles. The process for synthesizing these Nb₂O₅/C core-shell materials is as shown in Figure 3.1. Hydrothermal carbonization occurs through dehydration of glucose followed by polymerization and aromatization.^[63, 64] Microwave-assisted hydrothermal reaction promotes the carbonization of glucose within a reaction time of ~1 hr. As-synthesized Nb₂O₅/C core-shells were then annealed at 700 °C for 2 hrs under 5% H₂/95% N₂ gas flow for further carbonization of the shell. Finally, an oxidation process was performed on Nb₂O₅/C_F700 using nitric acid (2 M HNO₃) at reflux condition.

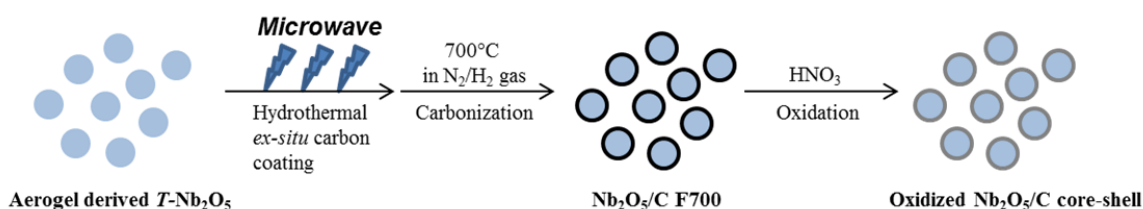


Figure 3.1. Synthesis of Nb₂O₅/C core-shell

The particle size, thickness of carbon shell and morphology of bare $T\text{-Nb}_2\text{O}_5$ nanoparticles and $\text{Nb}_2\text{O}_5/\text{C}$ core-shells were characterized by transmission electron microscopy (TEM). The average size of the bare Nb_2O_5 nanoparticles is 35 nm (in dia.) (Figure 3.2-(a)). Microwave-assisted hydrothermal reaction of glucose in the presence of $T\text{-Nb}_2\text{O}_5$ results in uniform coating of carbon on the surface of $T\text{-Nb}_2\text{O}_5$ as shown in Figure 3.2-(b). During the hydrothermal reaction, the particle size of the core material, $T\text{-Nb}_2\text{O}_5$ nanoparticles, were maintained (Figure 3.2-(b)). The shell thickness is associated with Nb_2O_5 to glucose molar ratio (Figure 3.3). ~5 nm of the carbon shell was obtained when a Nb_2O_5 to glucose molar ratio of 1:110 was used. For $\text{Nb}_2\text{O}_5/\text{C_F700}$, the core-shell structure was maintained during the annealing process, but the thickness of the shell was slightly decreased to ~4nm, as shown in Figure 3.2-(c). There was no change in particle size even after the annealing at 700 °C, which is a higher temperature than the temperature (600 °C) used for $T\text{-Nb}_2\text{O}_5$ synthesis. On the other hand, a significant particle growth was observed when the bare Nb_2O_5 was annealed at 700 °C (Figure 3.4). This indicates that the carbon shell prevents particle growth of $T\text{-Nb}_2\text{O}_5$ and is clear evidence for the core-shell formation by the hydrothermal reaction of glucose. Even after $\text{Nb}_2\text{O}_5/\text{C_F700}$ was oxidized, the core-shell structure, particle size as well as thickness of carbon shell remained constant (Figure 3.2-(d)). It is known that reaction of carbon with concentrated HNO_3 at reflux condition is very effective for surface modification, resulting in oxidation of the surface^[65]. XPS (Figure 3.5-(a)) and FT-IR (Figure 3.6) spectra of the oxidized $\text{Nb}_2\text{O}_5/\text{C}$ revealed that oxygen related functional groups such as C=O, C-O and -OH were indeed created upon oxidation.

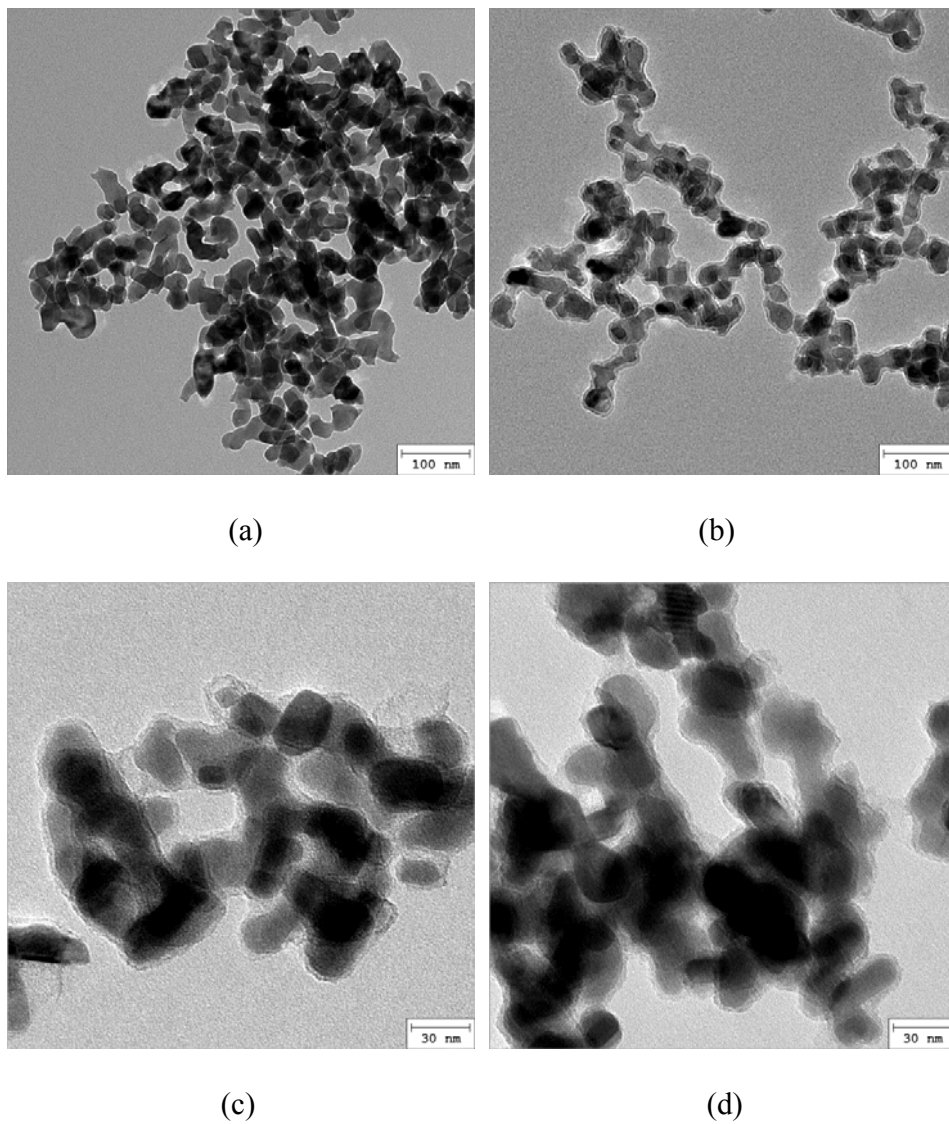
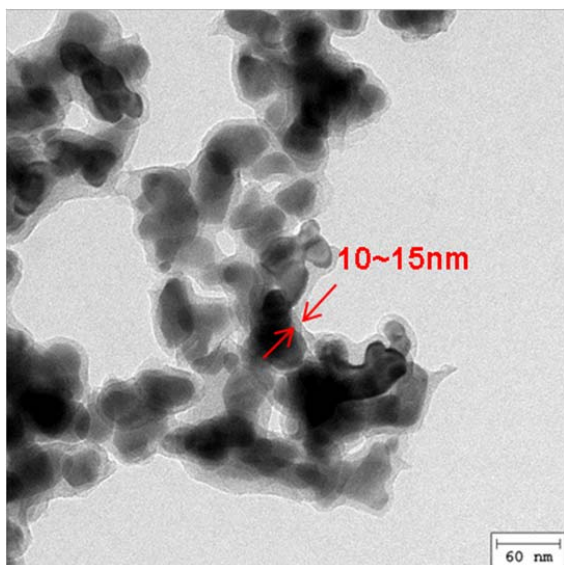
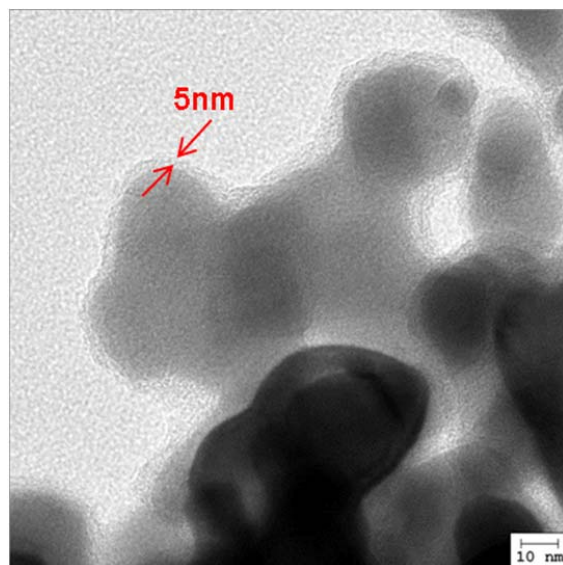


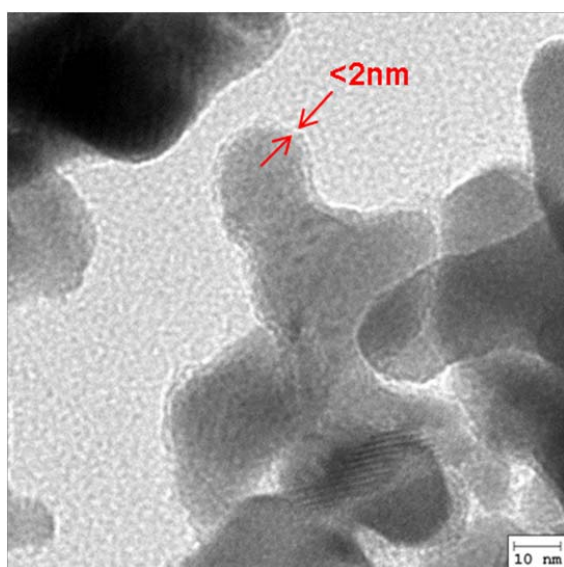
Figure 3.2. TEM images of bare $T\text{-Nb}_2\text{O}_5$ and $\text{Nb}_2\text{O}_5/\text{C}$ core-shells; (a) Bare $T\text{-Nb}_2\text{O}_5$ nanoparticles, (b) As-synthesized $\text{Nb}_2\text{O}_5/\text{C}$ core-shells (average shell thickness: 5 nm), (c) $\text{Nb}_2\text{O}_5/\text{C_F700}$ and (d) Oxidized $\text{Nb}_2\text{O}_5/\text{C_F700}$



(a)



(b)



(c)

Figure 3.3. $\text{Nb}_2\text{O}_5/\text{C}$ core-shell with different shell thickness; (a) 10-15 nm ($M_{\text{glucose}}/M_{\text{Nb}_2\text{O}_5} \sim 220$), (b) 5 nm ($M_{\text{glucose}}/M_{\text{Nb}_2\text{O}_5} \sim 110$) and (c) 2 nm ($M_{\text{glucose}}/M_{\text{Nb}_2\text{O}_5} \sim 55$)

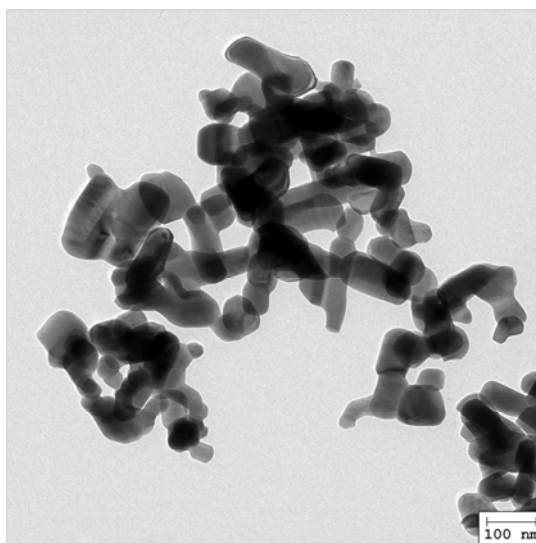


Figure 3.4. TEM image of Nb_2O_5 annealed at 700 °C (ave. particle size ~ 100 nm in dia.)

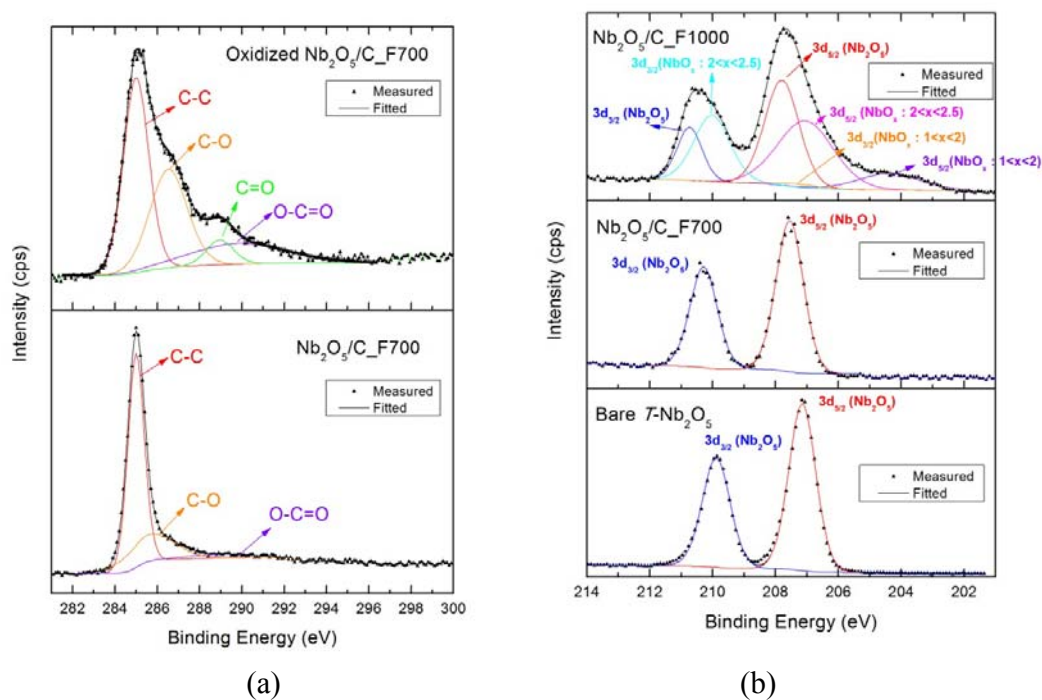


Figure 3.5. XPS spectra of bare $T\text{-Nb}_2\text{O}_5$ and $\text{Nb}_2\text{O}_5/\text{C}$ core-shells; (a) C 1s and (b) Nb 3d. The binding energy scale was calibrated from the carbon contamination using the C 1s peak at 285.0 eV. Peak identification for different carbon (C_{1s}) and niobium (Nb_{3d}) are based on references^[66, 67].

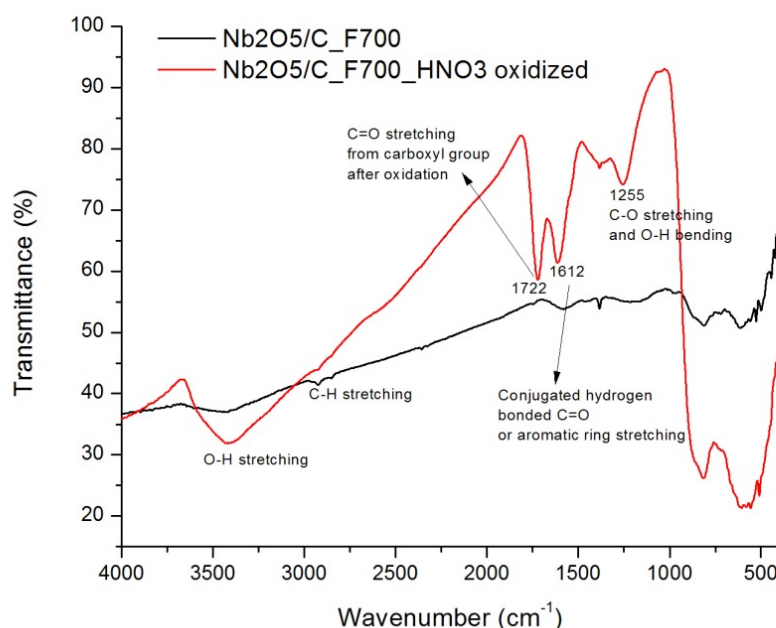


Figure 3.6. FT-IR spectra of Nb₂O₅/C core-shells; Upon oxidation, peaks for carboxylic groups increases dramatically

The Nb₂O₅ crystal phase for each core-shell material was determined using X-ray diffraction. As shown in Figure 3.7, the orthorhombic nature of Nb₂O₅ (*T*-Nb₂O₅, JCPDS 30-873) does not change during hydrothermal reaction followed by heat treatment and oxidation. Note that there was no evidence for formation of reduced niobium oxides (*i.e.* NbO₂) via carbothermal reaction that usually occurs between oxides and carbon at high temperature. XPS spectra (Figure 3.5-(b)) of Nb 3d also indicates that there is no formation of reduced niobium oxides during heat treatment on Nb₂O₅/C core-shells at 700°C, whereas some reduced niobium oxides were formed at 1000°C. Peak splitting at around 28° (2 theta) in both Nb₂O₅/C_F700 and oxidized Nb₂O₅/C_F700 indicates higher crystallinity of orthorhombic *T*-Nb₂O₅ due to higher

temperature (700 °C) heat treatment for carbonization than the temperature (600 °C) for formation of $T\text{-Nb}_2\text{O}_5$ (Figure 3.7).

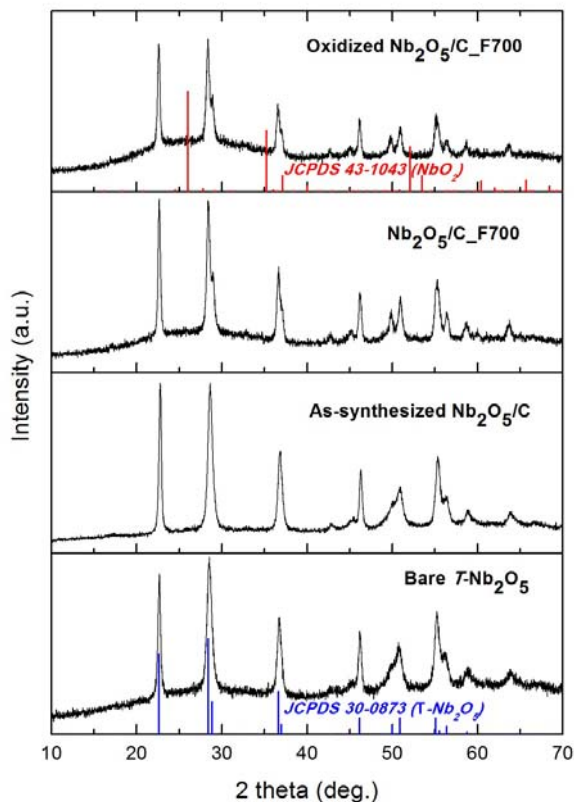


Figure 3.7. XRD patterns of the bare Nb_2O_5 and $\text{Nb}_2\text{O}_5/\text{C}$ core-shells; (a) Bare Nb_2O_5 , (b) As-synthesized $\text{Nb}_2\text{O}_5/\text{C}$ core-shell, (c) $\text{Nb}_2\text{O}_5/\text{C_F700}$ and (d) Oxidized $\text{Nb}_2\text{O}_5/\text{C_F700}$

The surface area calculated by nitrogen gas isotherms using the BET analysis is listed for each sample in Table 3.1. The BET surface area of as-synthesized $\text{Nb}_2\text{O}_5/\text{C}$ core-shell ($53 \text{ m}^2/\text{g}$) is slightly smaller than that of bare $T\text{-Nb}_2\text{O}_5$ ($70 \text{ m}^2/\text{g}$). This is because thin and dense (non-porous) layer of carbon was coated on the surface of bare $T\text{-Nb}_2\text{O}_5$. When as-synthesized

Nb₂O₅/C core-shell was annealed at 700 °C under forming gas, the BET surface area increased to 95 m²/g. Upon oxidation of Nb₂O₅/C_F700 using nitric acid, BET surface area decreased to 65 m²/g because there is more degradation of the porous structure at boiling temperature than fine micropores created during the oxidation^[65].

Table 3.1. Brunauer-Emmett-Teller (BET) surface areas and average pore sizes for Nb₂O₅/C core-shells with different shell thickness.

| | Bare <i>T</i> -Nb ₂ O ₅ | Nb ₂ O ₅ /C core-shell | | |
|--------------------------------------|--|--|--|--|
| | | As-synthesized | Nb ₂ O ₅ /C F700 | Nb ₂ O ₅ /C oxidized |
| BET surface area (m ² /g) | 70 | 53 | 95 | 65 |

Raman spectroscopy was utilized to characterize the carbon shell in Nb₂O₅/C core-shell materials. The I_D/I_G value, a ratio between the peak intensity of the D-band (disordered, ~ 1355 cm⁻¹) and that of the G-band (graphitic, 1500 ~ 1630 cm⁻¹), is generally used as an indicator for the degree of crystallinity of graphitic carbon.^[68, 69] As the I_D/I_G value approaches 0, the number of defects in graphitic carbon is minimized. However, it should be noted that a low I_D/I_G value also can be caused by amorphous carbon which can have up to 20 % sp³ carbons, whereas graphitic carbon has no sp³ carbons.^[68] Figure 3.8-(a) shows that as-synthesized Nb₂O₅/C has a low I_D/I_G value (0.37). TGA data on as-synthesized Nb₂O₅/C (Figure 3.9) shows that there is a significant weight loss (~ 10 %) starting at 250 °C, indicating that some organics related to the precursor, glucose, still remain in the carbon shell after microwave-assisted hydrothermal reaction. Considering the TGA data, it is likely that the low I_D/I_G value for as-synthesized

$\text{Nb}_2\text{O}_5/\text{C}$ is due to the amorphous nature of the carbon shell and not due to ordering of graphitic carbon. Upon thermal annealing at 700 °C, the intensity of D-band (1332 cm^{-1}) compared to G-band (1590 cm^{-1}) increases because nanocrystalline carbons (disordered) are generated during the annealing. Thus, $I_{\text{D}}/I_{\text{G}}$ value for $\text{Nb}_2\text{O}_5/\text{C_F700}$ increases to 0.86 (Figure 3.7-(b)). After $\text{Nb}_2\text{O}_5/\text{C_F700}$ is oxidized, $I_{\text{D}}/I_{\text{G}}$ value (0.83) does not change much due to the low temperature (110 °C) treatment during oxidation (Figure 3.7-(c)). This raman study, along with the TEM images, indicate that the shell on the $T\text{-Nb}_2\text{O}_5$ is indeed carbon and its crystallinity is improved by thermal annealing.

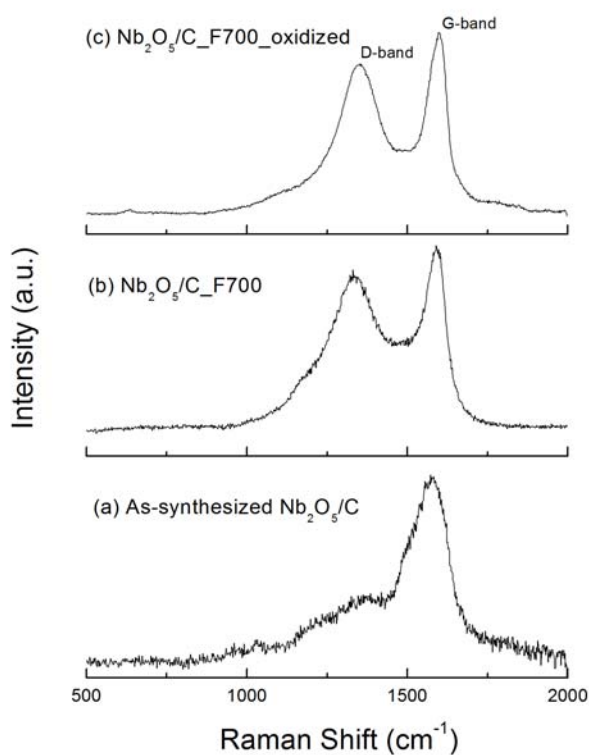


Figure 3.8. Raman spectra of $\text{Nb}_2\text{O}_5/\text{C}$ core-shells; (a) As-synthesized $\text{Nb}_2\text{O}_5/\text{C}$, (b) $\text{Nb}_2\text{O}_5/\text{C_F700}$, and (c) Oxidized $\text{Nb}_2\text{O}_5/\text{C_F700}$

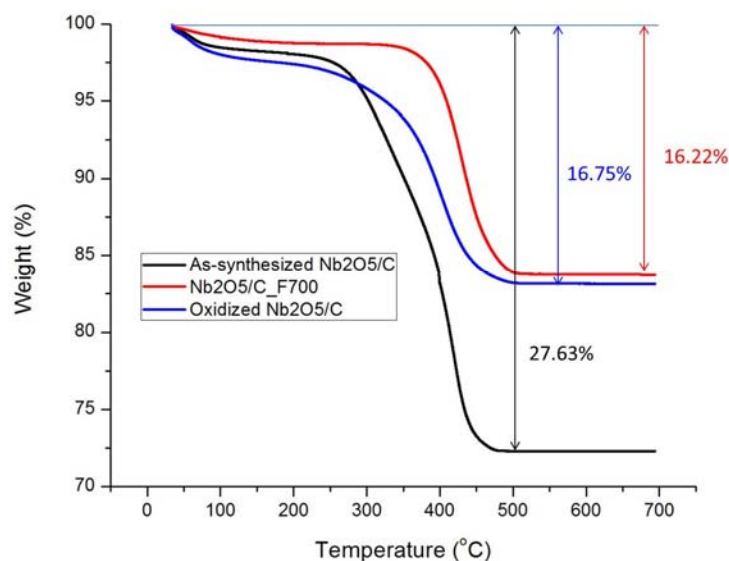


Figure 3.9. Thermal gravimetric analysis (TGA) on Nb₂O₅/C core-shells (in air)

Chapter 3.3.2. Voltammetry studies on Nb₂O₅/C core-shell

Cyclic voltammetry (CV) with lithium ion electrolyte (1 M LiClO₄) was used to determine the electrochemical properties of the different Nb₂O₅/C core-shell materials. In these experiments, the total weight of each Nb₂O₅/C core-shell was used to calculate the gravimetrically normalized current and capacity. Figure 3.10 demonstrates that oxidized Nb₂O₅/C_F700 has much higher current response than the other materials, as-synthesized Nb₂O₅/C and Nb₂O₅/C_F700. Unique to oxidized Nb₂O₅/C_F700 are two cathodic peaks near 1.7 V and 1.5 V (vs. Li/Li⁺) and a broad anodic peak at 1.85 V.

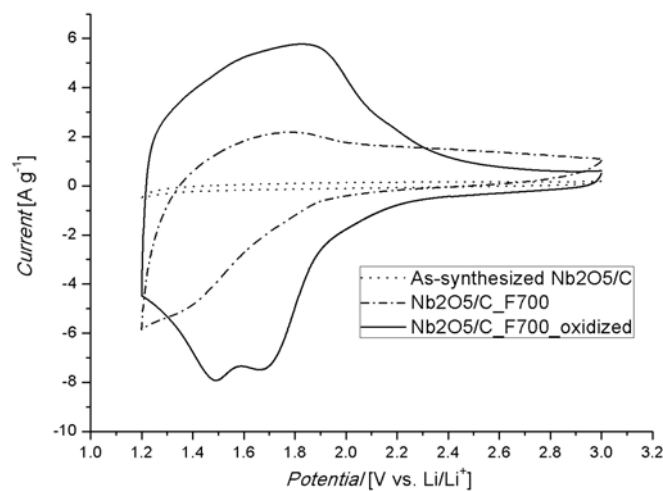


Figure 3.10. Cyclic voltammetry (CVs) for Nb₂O₅/C core-shells (thin film~20 μ g) at 10 mV/s

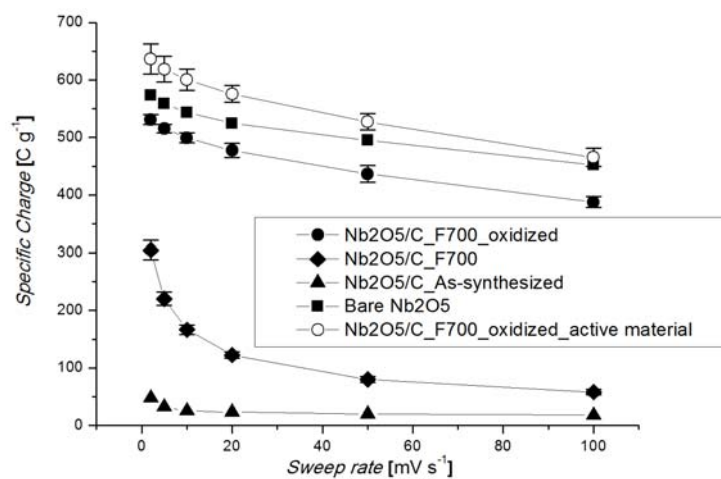
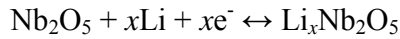


Figure 3.11. Specific charge of bare Nb₂O₅ and Nb₂O₅/C core-shells at different sweep rates (2-100 mV/s). Mass loading is ~ 20 μ g (film thickness is less than 200 nm).

Figure 3.11 shows that specific charges for as-synthesized Nb₂O₅/C are very low (< 50 C/g). This is because the carbon shell in as-synthesized Nb₂O₅/C includes hydrocarbons left during hydrothermal reaction of glucose and water (Figure 3.9), which impedes lithium ion access to the Nb₂O₅ core. Considering the dense carbon shells, the capacity of as-synthesized Nb₂O₅/C mainly relies on the low surface area of the Nb₂O₅ (Table 3.1) which is much lower than that of activated carbon for electrochemical double layer capacitance (EDLCs)^[2]. Nb₂O₅/C_F700 has higher capacity than as-synthesized Nb₂O₅/C at all sweep rates because of its higher conductivity due to heat treatment at 700°C for further carbonization of the shell, but it is still much lower than the capacity of bare *T*-Nb₂O₅. For Nb₂O₅/C_F700, there is a significant discrepancy in capacity between slow (2 mV/s) and fast (100 mV/s) sweep rate even though conductivity is improved by the carbon shell. This electrochemical behavior of Nb₂O₅/C_F700 contrasts with studies for CNT/oxides^[49] or graphene/oxides^[50] nanocomposites where high conductivity improves rate capability. It may be caused by a characteristic of the core-shell structure where the lithium ions are unable to access the electrochemically active core material because of the carbon shell. Thus, ionic conductivity (or lithium ion transport) through the carbon shell becomes more important factor than electronic conductivity at high sweep rate. In CNT/oxide or graphene/oxide systems, however, there is no limitation for electrolytes to access the oxide phase, even at fast sweep rates. Following the trend that the capacity of Nb₂O₅/C_F700 increases drastically when sweep rate is slower than 20 mV/s (Figure 3.11), it is readily predicted that capacity of Nb₂O₅/C-F700 would be comparable or even higher than that of the bare *T*-Nb₂O₅ at very slow sweep rate (equivalent to 0.1~1C). Achieving the high capacity at slow sweep rate with core-shell structures has been utilized mainly for batteries that have longer

charge/discharge time (hours) than supercapacitors (minutes or seconds). After an oxidation process was performed on Nb₂O₅/C_F700, the capacity is increased significantly at all sweep rates. When the capacity of oxidized Nb₂O₅/C_F700 is normalized by the weight of active material, Nb₂O₅, the specific capacitance is higher than that of bare *T*-Nb₂O₅. Moreover, the capacity of 636 C/g at 2 mV/s of oxidized Nb₂O₅/C_F700 is close to the theoretical value (725 C/g) for Nb₂O₅. This amount of charge is based on $x = 2$ according to the following equation for lithium intercalation into Nb₂O₅^[35].



In addition, the rate capability of Nb₂O₅/C is improved by the oxidation process as shown by the capacity (465 C/g) of the oxidized Nb₂O₅/C_F700 at 100 mV/s. This amount of charge is more than 70% of the capacity at 2 mV/s (Figure 3.11).

To further investigate the effect of oxidation on the electrochemical behavior of Nb₂O₅/C core-shells, impedance measurements were performed on Nb₂O₅/C_F700 and oxidized Nb₂O₅/C_F700. Figure 3.12 shows the electrochemical impedance spectra (EIS) of Nb₂O₅/C_F700 and oxidized Nb₂O₅/C_F700. The circuits used for curve fitting are shown in Figure 3.13. The EIS data were collected at 1.2 V (vs. Li/Li⁺) after three CV cycles at 10 mV/s. From the Nyquist plot (Figure 3.12-(a)), it can be seen that before oxidation the impedance has nearly a -45 degree phase angle (Figure 3.12-(b)) which is associated with a diffusion controlled system. After oxidation the charge transport is improved and the capacitance contributions from the double layer and the pseudocapacitance can be distinguished according to the equivalent

circuit following the work by Conway *et al.*^[4] For the pseudocapacitive model, two constant phase elements are used with one representing the double layer contribution and the other the pseudocapacitive contribution. An additional resistor R_{Elect} was added to the Conway model to account for the bulk electrolyte contribution. The bulk electrolyte contribution is of the same magnitude in both systems (Table 3.2 and Table 3.3). Based on the circuit modeling the $\text{Nb}_2\text{O}_5/\text{carbon}$ core shell before oxidation shows diffusion limited capacitance, which makes it difficult to distinguish the double layer and pseudocapacitive contribution. From the impedance it is evident that electrolyte ion diffusion through the carbon shell is the rate limiting factor in $\text{Nb}_2\text{O}_5/\text{C_F700}$. However upon oxidation, the ion transport becomes faster and thus the oxidized $\text{Nb}_2\text{O}_5/\text{C_F700}$ begins to have capacitive behavior similar to the bare Nb_2O_5 .

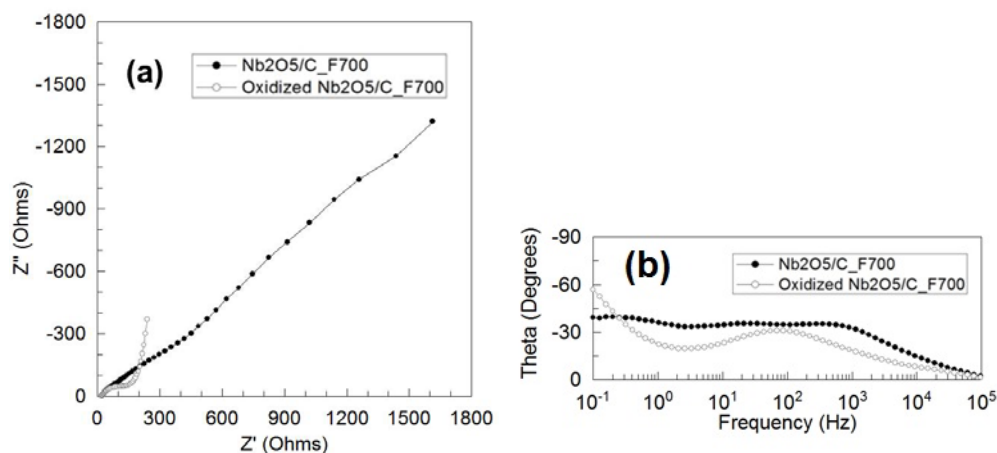


Figure 3.12. Electrochemical impedance spectra (EIS) for $\text{Nb}_2\text{O}_5/\text{C_F700}$ and oxidized $\text{Nb}_2\text{O}_5/\text{C_F700}$ (at 1.2 V (vs. Li/Li^+)); (a) Nyquist plot and (b) phase angle as a function of frequency

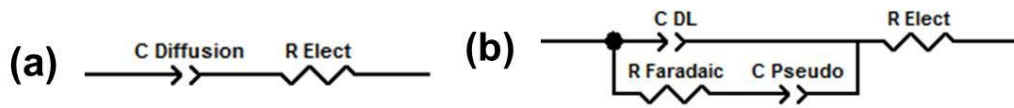


Figure 3.13. The circuits for Nb₂O₅/C_F700 (a) and oxidized Nb₂O₅/C_F700 (b).

Table 3.2. The values of circuit elements for Nb₂O₅/C_F700

| Circuit Element | Nb ₂ O ₅ /C_F700 |
|------------------------------|--|
| $C_{\text{Diffusion}}$ | 599.9×10^{-6} |
| $C_{\text{Diffusion Phase}}$ | 0.44 |
| R_{Elect} | 16.74 |

Table 3.3. The values of circuit elements for oxidized Nb₂O₅/C_F700

| Circuit Element | Oxidized Nb ₂ O ₅ /C_F700 |
|---------------------------|---|
| C_{DL} | 333.5×10^{-6} |
| $C_{\text{DL Phase}}$ | 0.65 |
| C_{Pseudo} | 3579.6×10^{-6} |
| $C_{\text{Pseudo Phase}}$ | 0.83 |
| R_{Faradaic} | 163.2 |
| R_{Elect} | 20.63 |

Chapter 3.3.3. The effect of oxidation on the kinetics of Nb₂O₅/C core-shell

To determine rate limiting factor for a charge storage mechanism on each Nb₂O₅/C sample, charge versus $\nu^{-1/2}$, where ν is sweep rate, is plotted in Figure 3.14. According to previous studies by Trassati *et al.*^[42, 43], a linear slope in the plot is associated with semi-infinite diffusion, while frequency independent capacity represents capacitive behavior. For a system

having the frequency independent response, the extrapolated y-intercept will yield the infinite sweep rate capacitance. As-synthesized Nb₂O₅/C has a linear slope over different sweep rates (Figure 3.14) indicating that current response for as-synthesized Nb₂O₅/C depends on diffusion of electrolyte. The capacity of Nb₂O₅/C_F700 also changes linearly as a function of $v^{-1/2}$ (Figure 3.14), showing that it is still a diffusion controlled system even though the slope for Nb₂O₅/C_F700 was much higher than that for as-synthesized Nb₂O₅/C. However, upon oxidation, the capacity becomes independent of $v^{-1/2}$ which is similar to that of bare Nb₂O₅ (Figure 3.14). This implies that the oxidation step helps lithium ion transport through the carbon shell and the kinetics of oxidized Nb₂O₅/C_F700 begins to be governed by the active material, Nb₂O₅, not the carbon shell.

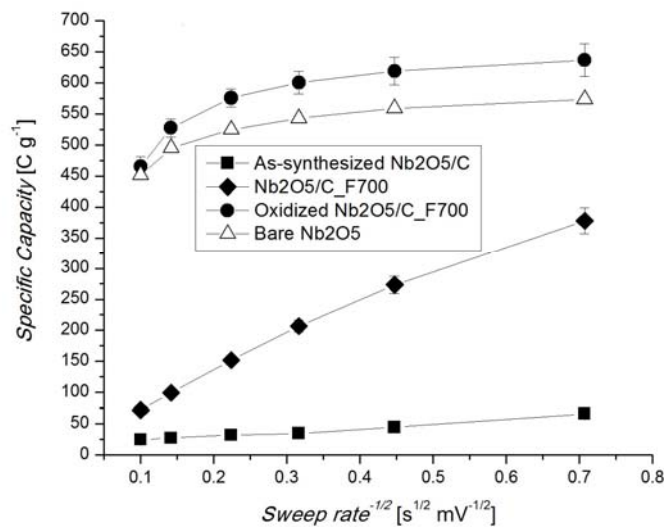


Figure 3.14. Charge storage as a function of sweep rate^{-1/2} (Specific charge is based on the active material)

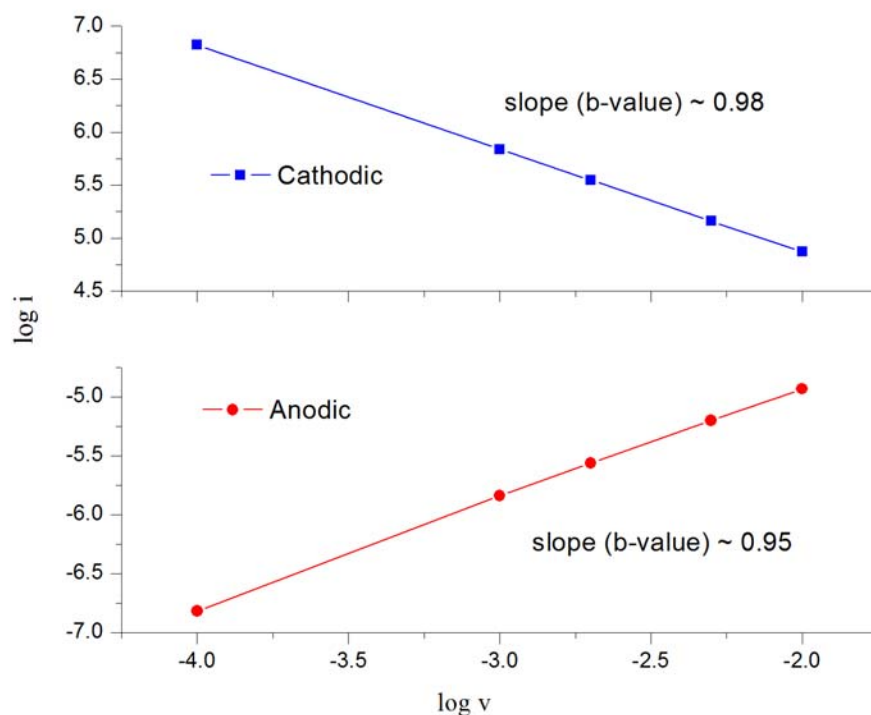


Figure 3.15. b -value characterization for oxidized Nb₂O₅/C_F700 using the current at peak potentials at sweep rates of 0.1 – 10 mV/s.

The capacitive behavior of oxidized Nb₂O₅/C_F700 was characterized by analyzing the cyclic voltammetry data at various sweep rates according to^[70]

$$i = av^b$$

where the measured current i obeys a power law relationship with the sweep rate v . Both a and b are adjustable parameters. The b -value can be determined from the slope in the plot of $\log i$ vs. $\log v$. When the b -value is close to 0.5, the current response is diffusion controlled. When the

current is proportional to the sweep rate ($b = 1.0$), on the other hand, it represents that the current is purely capacitive. For b -value analysis on oxidized Nb₂O₅/C_F700, the measured currents at peak potential, where cathodic or anodic peak was formed, were collected at various sweep rates. The b -values for cathodic and anodic peak are 0.98 and 0.95, respectively (Figure 3.15). These values are closed to 1.0, indicating that most of current response of oxidized Nb₂O₅/C_F700 is capacitive. This capacitive behavior from b -value characterization is in good agreement with the sweep rate independent capacity as discussed above.

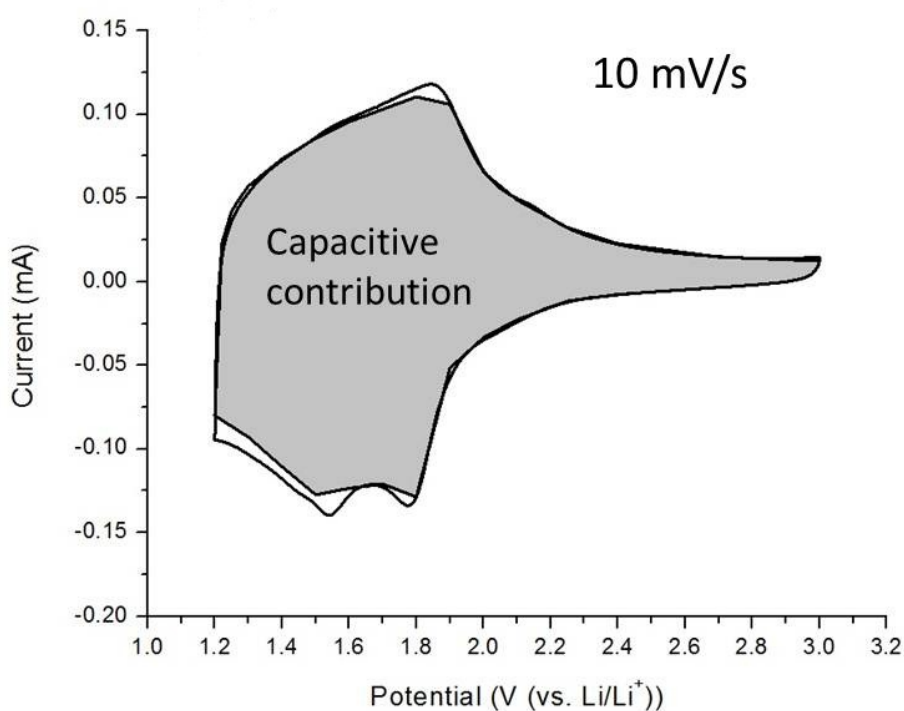


Figure 3.16. Capacitive contribution in oxidized Nb₂O₅/C_F700 at 10 mV/s

To quantify the capacitive contribution to the total measured current, a closer examination of voltammetric sweep rate dependence was performed. Using the concept presented above, one can express the current response at a fixed potential (V) as being the combination of two separate mechanisms, capacitive and diffusion-controlled^[71]:

$$i(V) = k_1v + k_2v^{1/2}$$

where k_1v and $k_2v^{1/2}$ corresponds to capacitive and diffusion contribution, respectively. This equation can be arranged for analytical purpose as follows,

$$i(V)/v^{1/2} = k_1v^{1/2} + k_2$$

By plotting $i/v^{1/2}$ vs. $v^{1/2}$ at various potentials, k_1 and k_2 value can be determined by characterizing the slope and y-axis intercept, respectively. To analyze k_1 and k_2 value, the sweep rates of 0.1 to 10 mV/s were used and a slight peak shift as a function of the sweep rate was neglected. Figure 3.16 shows that capacitive contribution (shaded region) is dominant at both peak potentials and the rest of them. This demonstrates that over 90 % of current response from the oxidized Nb₂O₅/C_F700 is associated with the capacitive contribution. However, it is noteworthy that this capacitive contribution may arise not only from pseudocapacitive behavior of Nb₂O₅ core, but also from double layer capacitance by the carbon shell. Thus, it is important to investigate the double layer contribution in oxidized Nb₂O₅/C_F700. To check the double layer contribution, another CV was performed using tetraethylammonium tetrafluoroborate (1 M

TEABF₄) in acetonitrile as electrolyte with Ag reference and Pt counter electrodes. It is apparent that the double layer contribution is very small compared to the total charge storage (Figure 3.17). These results are in good agreement with the low BET surface area of oxidized Nb₂O₅/C_F700 (65 m²/g) compared to carbons for EDLCs (>1000 m²/g). Therefore, it is evident that the charge storage in oxidized Nb₂O₅/C_F700 is mainly due to pseudocapacitive behavior of Nb₂O₅ core. In addition, this study on core-shell structure where the surface of active material is covered by carbon confirms that pseudocapacitance of Nb₂O₅ occurs via intercalation pseudocapacitance (in the bulk of material) instead of redox reaction on the surface. Thus, it would be interesting to apply the oxidized core-shell concept for other materials having intercalation pseudocapacitance in order to obtain high energy density as well as power density.

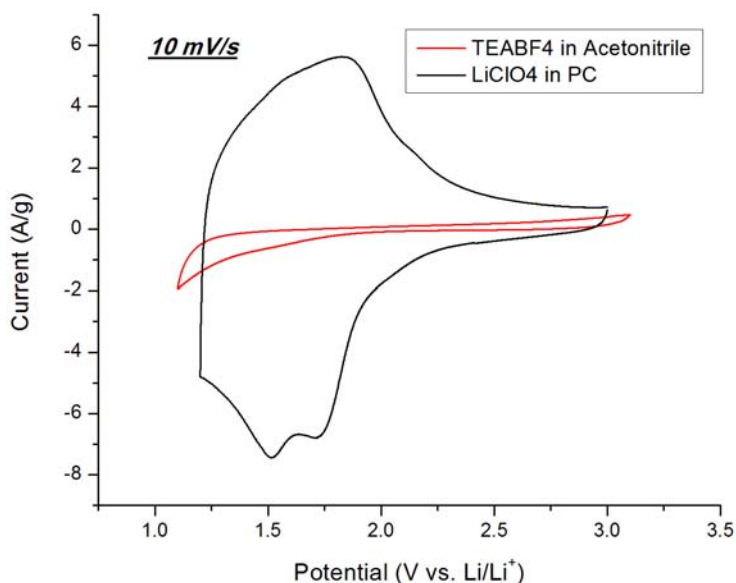


Figure 3.17. Cyclic voltammetry on oxidized Nb₂O₅/C_F700 using different electrolytes: LiClO₄ in PC and TEABF₄ in acetonitrile.

Chapter 3.3.4. Electrochemical behavior of thick film (Bare Nb₂O₅ vs. Nb₂O₅/C core-shell)

To further investigate the effect of carbon coating on the electrochemical properties of Nb₂O₅, electrodes with higher mass loading (~ 0.5 mg) and thickness (~ 5 μm) were prepared and tested using cyclic voltammetry. As shown in Figure 3.18, the capacity of bare Nb₂O₅ without any carbon additives is much smaller than that for thin film (< 200 nm) of the same material at all sweep rates (Figure 3.11). This indeed shows that the capacity of bare Nb₂O₅ decreases with higher mass loading due to its low conductivity. The capacity of bare Nb₂O₅ can be improved by mixing the electrode material with carbon additive (10 wt %) (Figure 3.18). However, a significant capacity decrease is observed even in the electrode with carbon additive as higher sweep rate is applied (526 C/g at 2 mV/s and 52 C/g at 100 mV/s). Even though carbon additive improves the conductivity of the electrode, charge transfer resistance between aggregated Nb₂O₅ nanoparticles still limits the charge storage especially at high sweep rates. Moreover, for bare Nb₂O₅ with carbon additive, the aggregated Nb₂O₅ nanoparticles are likely to have limited contact with the carbon additive and thus a significant polarization is generated during voltammetry sweeps.

Figure 3.18 also shows that the oxidized Nb₂O₅/C_F700 without carbon additive possesses higher capacity at all sweep rates (587 C/g at 2 mV/s and 140 C/g at 100 mV/s) than bare Nb₂O₅ without carbon additive. Note that the capacity values for the oxidized Nb₂O₅/C_F700 without carbon additive is higher than even those for bare Nb₂O₅ with carbon additive. The capacity difference between the oxidized Nb₂O₅/C_F700 and bare Nb₂O₅ with carbon additive becomes more significant at higher sweep rate (> 10 mV s⁻¹). This improvement

in both capacity and rate capability for the oxidized Nb₂O₅/C_F700 is because the complete carbon coating provides the electron conducting pathway between Nb₂O₅ nanoparticles. In addition of a carbon additive to Nb₂O₅/C core-shell is not as effective as the addition to bare Nb₂O₅ because the Nb₂O₅/C core-shell already contains ~10 wt% of carbon (Figure 3.9). Thus, the oxidized Nb₂O₅/C_F700 with carbon additive has the same electrochemical behavior as the bare Nb₂O₅ without carbon additive, as shown in Figure 3.18. The capacities of the oxidized Nb₂O₅/C_F700 at different sweep rates are comparable to those reported for CNT/Nb₂O₅ nanocomposite (267 C/g at 50 mV/s which is 60 % of the capacity at 1 mV/s)^[72]. In addition, the rate capability of CNT/Nb₂O₅ nanocomposite is similar to another CNT-based composite, CNT/V₂O₅^[49]. Therefore, the electrochemical performance of the oxidized Nb₂O₅/C_F700 without carbon additive indicates that core-shell structure is promising for pseudocapacitors as well as batteries.

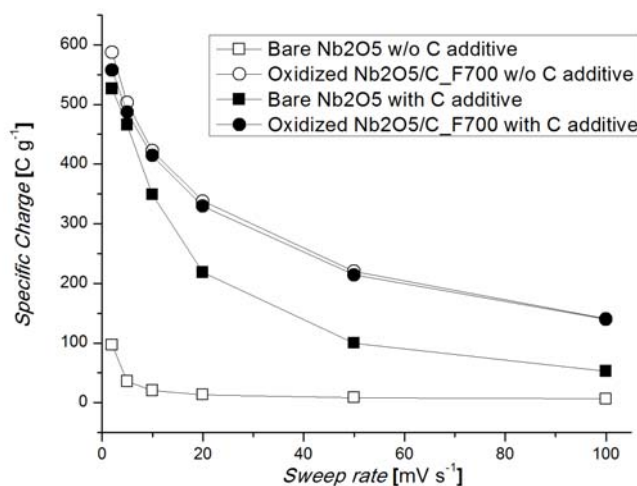


Figure 3.18. Capacity of bare Nb₂O₅ and oxidized Nb₂O₅/C_F700. Mass loading on stainless current collector is ~0.5 mg. Film thickness is ~ 5 μm.

Chapter 3.4. Conclusion

The results presented in this chapter, establish that the core-shell structure is beneficial for pseudocapacitors whose charge storage occurs through the intercalation pseudocapacitance mechanism. The microwave-assisted hydrothermal reaction, was very effective producing the Nb₂O₅/C core-shell structure. Electrolyte ion transport through the carbon shell is the rate limiting step for the Nb₂O₅/C core-shells. Additional thermal annealing of Nb₂O₅/C core-shells at 700 °C improved the capacity, but it takes an oxidation process with nitric acid to dramatically improve the kinetics of the Nb₂O₅/C core-shells (> 90% capacitive current). The oxidized Nb₂O₅/C core-shells exhibited comparable capacity and rate capability with bare Nb₂O₅ in thin electrodes (< 200 nm, ~ 20 µg). In thicker electrodes (~ 5 µm, ~ 0.5 mg) the bare Nb₂O₅ requires a carbon additive but even with adding the same mass of carbon, the core-shell structure's superior distribution of carbon delivers higher capacity electrodes with better rate capability.

Chapter 4. Transition metal oxide bronzes for reconfigurable electrodes

Chapter 4.1. Introduction

Energy storage systems having both high energy and high power densities are essential to satisfy the demands for future energy storage devices. In particular, current technologies for batteries and supercapacitors are far from satisfying the requirements for electric vehicles. Improvements in energy storage are necessary in order for electric vehicles to successfully enter the market and there are currently many efforts addressing this issue. For example, nanoscale electrode materials or conducting nanoparticle additives^[73] have been utilized in batteries to enhance electronic conductivity which leads to an increase in power. To improve the energy density of supercapacitors, approaches such as assembling asymmetric cells and using non-aqueous electrolytes^[74], have also been studied. Fundamentally, the methods to improve the energy storage properties rely heavily on the materials' architectures, conductive additives and stable electrolytes.

In this study, we propose a 'reconfigurable electrode' as a new candidate for electrochemical energy storage devices which can render both high power and energy. The idea here is to tailor the composition of the electrode material to provide either high energy or high power by using the variable electrical properties exhibited by certain intercalation materials. For instance, at high levels of intercalation of certain cations, the reconfigurable electrode may generate high power due to its high conductivity, while it can also render high energy at low levels of intercalation because of the remaining vacant sites for cation intercalation. Transition metal oxide bronzes are chosen for this study due to their unique electrical properties.

Chapter 4.2. Technical backgrounds: Transition metal oxide bronzes

Reduced transition metal oxide bronzes have been investigated since sodium tungsten oxide, Na_xWO_3 , was discovered by Wohler in 1824^[75]. It is called ‘bronze’, even though it is not a metal alloy, because of its metallic luster. Accordingly, the term bronze includes a large variety of ternary transition metal oxides with the general formula $\text{A}_x\text{M}_y\text{O}_z$, where A is usually an alkali cation (e.g. Li^+ , Na^+ , K^+) and M is a transition metal (e.g. Ti, V, Nb, Mo, Ta, W, Re). Binary, reduced transition metal oxides (e.g. Mo_4O_{11} , ReO_3), and quaternary transition metal oxides are often classified as bronzes as well. The structures of these materials are closely related to that of ReO_3 with MO_6 corner and/or edge-sharing arranged in either a three-dimensional (3-D) network or two-dimensional (2-D) layer structures. The A cations fill the interstitial sites created by the corner and/or edge-sharing polyhedra. Typically, the bronzes are colored with a metallic sheen, chemically inert to even strong acids and exhibit metallic or semiconducting behavior.^[76] The reason why the bronzes become metallic as A cations are inserted into the host oxide frame is because the empty conduction band of the insulating metal oxide is partially filled with electrons provided by the alkali metal A.

Chapter 4.2.1. Sodium tungsten bronze (Na_xWO_3)

Depending on the number of sodium ions (Na^+) inserted in bulk WO_3 , a series of sodium tungsten bronzes (Na_xWO_3) can be formed. Na_xWO_3 shows very interesting optical properties and its color changes from yellowish green to gray, blue, deep violet, red, and finally to gold as x increases, as shown in Figure 4.1. The metal-insulator transition of Na_xWO_3 occurs for $x > 0.25$.

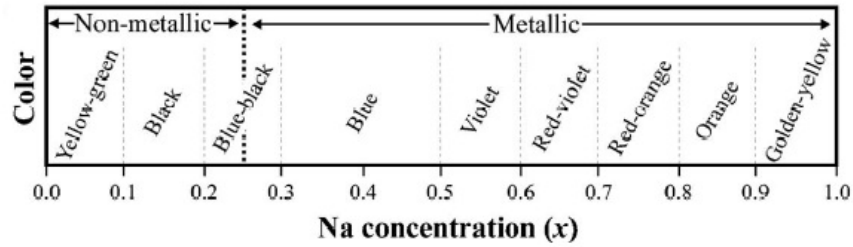


Figure 4.1. Optical properties of Na_xWO_3 with Na concentration^[77]

The material also goes through phase changes for $x < 0.4$. However, for $x > 0.5$, the structure stabilizes; Na_xWO_3 retains the perovskite crystal structure and has cubic symmetry (Figure 4.2). The band structure for Na_xWO_3 is well understood.^[77] With WO_3 , the Fermi level lies at the top of the oxygen 2p bands. The addition of the 3s electrons from sodium are transferred into the empty π^* band for the tungsten 5d so that the material takes on metallic behavior.

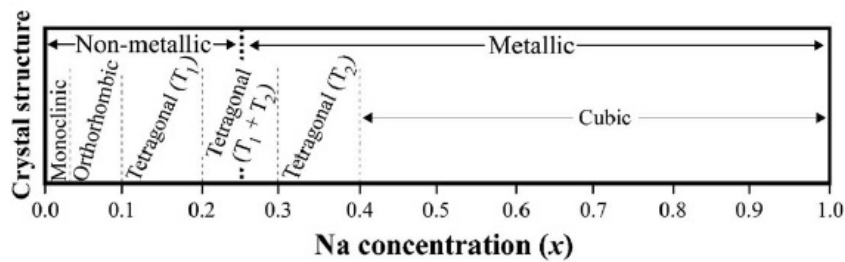


Figure 4.2. Phase diagram of Na_xWO_3 with Na concentration^[77]

For cubic phase, the sodium content x in Na_xWO_3 can be determined using following equation.^[78]

$$a_0 = (3.7845 + 0.0820x) \text{ \AA}, \text{ where } a_0 \text{ is a lattice parameter}$$

Chapter 4.2.2. Sodium molybdenum bronzes (Na_xMoO_3 or $\text{Na}_{0.9}\text{Mo}_6\text{O}_{17}$)

Among the various bronzes, molybdenum bronzes have been investigated intensively because of their unusual properties such as quasi-low-dimensional behavior, metal-insulator transition and insulator-to-superconductor transition.^[76] There are three different kinds of molybdenum bronzes depending on stoichiometric compositions and structure types. First, the blue bronze ($\text{A}_{0.3}\text{MoO}_3$, where A is K, Rb, Tl) is quasi-one-dimensional metal ($\sigma(\text{RT}) \sim 10^4 (\Omega\text{-cm})^{-1}$) and monoclinic. The conductivity along the b axis is larger than the other directions because the conduction electrons are located only on certain MoO_6 octahedra in the Mo layers, which accounts for anisotropic metallic behavior in the blue bronzes. Second, the red bronzes ($\text{A}_{0.33}\text{MoO}_3$, where A is Li, Na, K, Rb, Cs, Tl) have significantly different crystal structure (triclinic) and semiconducting ($\sigma(\text{RT}) \sim 10^{-4} (\Omega\text{-cm})^{-1}$) behavior even though they have a similar composition to the blue bronzes. The lower conductivity of the red bronzes is presumably due to the diminished d - π overlap along the critical Mo-O chain direction (along b) compared to the blue bronzes.

The purple bronzes ($\text{A}_{0.9}\text{Mo}_6\text{O}_{17}$, where A is Li, Na, K, and $\text{AMo}_6\text{O}_{17}$, where A is Tl) are differentiated from the other molybdenum bronzes due to their structures and electronic

properties. The potassium purple bronze $\text{K}_{0.9}\text{Mo}_6\text{O}_{17}$ has separated metal-oxygen layers of composition Mo_6O_{17} , which are made up of both MoO_6 octahedra and MoO_4 tetrahedra (Figure 4.3)^[79]. The sodium purple bronze ($\text{Na}_{0.9}\text{Mo}_6\text{O}_{17}$) and the thallium purple bronze $\text{Tl-Mo}_6\text{O}_{17}$ are similar in structure to the potassium purple bronze. The effective Mo valences are +6 on the Mo (Mo_1 of Figure 4.3) in tetrahedral sites and +5.1 and +5.8 on the two crystallographically nonequivalent Mo in octahedral sites (Mo_2 and Mo_3 , respectively, in Figure 4.3). Thus the 4d electrons of molybdenum atoms are located in the two-dimensional slabs of octahedra, which accounts for quasi-two-dimensional metal behavior ($\sigma(\text{RT}) \sim 10^4 \text{ } (\Omega\text{-cm})^{-1}$).^[80] However, the lithium purple bronze ($\text{Li}_{0.9}\text{Mo}_6\text{O}_{17}$) differs from the other purple bronzes in that it has no separated metal-oxygen layers (Figure 4.4). Therefore, $\text{Li}_{0.9}\text{Mo}_6\text{O}_{17}$ has quasi-one-dimensional metal behavior along the b axis.^[80]

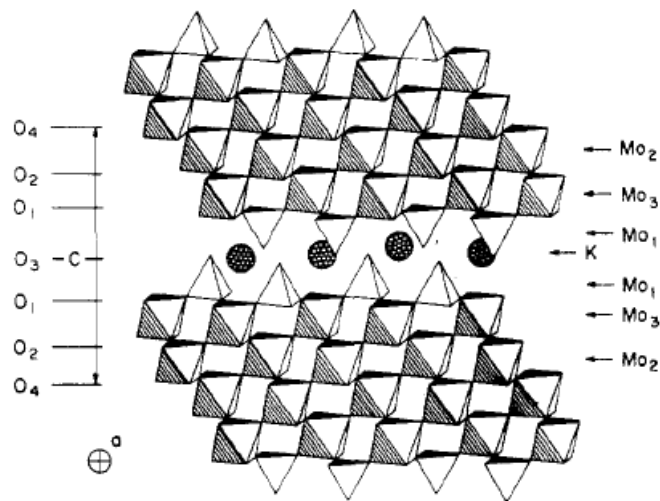


Figure 4.3. Crystal structure of purple molybdenum bronze ($\text{K}_{0.9}\text{Mo}_6\text{O}_{17}$)^[79]

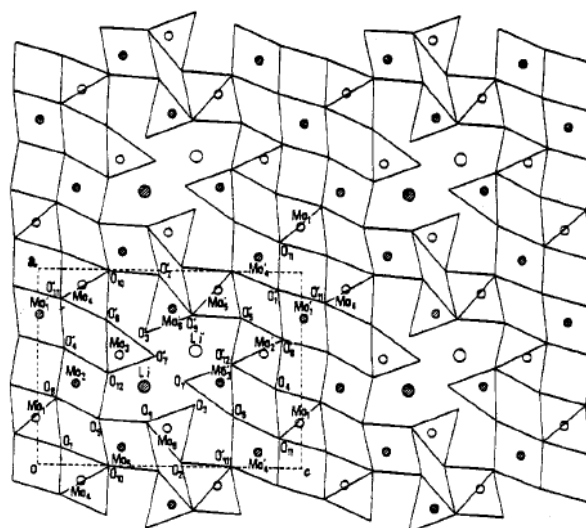


Figure 4.4. Crystal structure of purple molybdenum bronze ($\text{Li}_{0.9}\text{Mo}_6\text{O}_{17}$) projected in ac plane^[81]

Chapter 4.3. Experimental

Chapter 4.3.1. Synthesis of Cubic $\text{Na}_{0.85}\text{WO}_3$

Fine powders of $\text{Na}_{0.85}\text{WO}_3$ were synthesized by reducing aqueous Na_2WO_4 using aqueous NaBH_4 .^[78] 40 ml of 0.25 M Na_2WO_4 was reduced by adding 10 ml of 2.5 M NaBH_4 in NaOH . The pH of the initial NaOH solution was 12.00. After 1 hr reaction under stirring, the particles were collected using centrifugal force, and then washed with methanol several times. To obtain crystalline (cubic) structure of Na_xWO_3 , the particles were heat treated at 600°C under N_2/H_2 gas for 2hrs.

Chapter 4.3.2. Synthesis of $\text{Na}_{0.9}\text{Mo}_6\text{O}_{17}$

The purple molybdenum bronze can be synthesized by reducing $\alpha\text{-MoO}_3$ using sodium hydrosulfite, $\text{Na}_2\text{S}_2\text{O}_4$, followed by heat treatment under Ar.^[82, 83] $\alpha\text{-MoO}_3$ (0.4 g) was first suspended in distilled water (20 ml) and stirred for 30 mins. Then, solid mixture of $\text{Na}_2\text{S}_2\text{O}_4$ (0.16 g) and $\text{Na}_2\text{MoO}_4 \cdot 2\text{H}_2\text{O}$ (4.8 g) was introduced and reacted for 3 hrs. All these reaction were done under oxygen-free nitrogen flowing system using a Schlenk line. The precipitate was collected by centrifugation, washed with distilled water, and dried at 60°C in air. The dried bluish precipitates were further heat treated to 400°C under Ar with a ramp rate of 10 °C/min to obtain purple $\text{Na}_{0.9}\text{Mo}_6\text{O}_{17}$.

Three different $\alpha\text{-MoO}_3$ were synthesized in this study. First, $\alpha\text{-MoO}_3$ was synthesized by thermal annealing MoO_3 aerogel. In the synthesis of MoO_3 aerogel^[84], the precursor, MoCl_5 , in ethanol (solution 1) and 30% of polyacrylic acid (PAA, MW~5000) and water in ethanol (solution 2) were kept in ice for 2hrs and then mixed together. Propylene oxide which was used as a gelation agent was then added to the mixed solution. A translucent reddish-brown gel formed after 2 hrs under moderate stirring. The wet gel was aged for 1 day and then stored in acetone for 5 days. The gel was finally supercritically dried using liquid CO_2 . As-prepared MoO_3 aerogels were then annealed at 400°C for 2hrs to obtain $\alpha\text{-MoO}_3$.

In a second approach, $\alpha\text{-MoO}_3$ was synthesized via microwave-assisted solvothermal method followed by thermal annealing. MoCl_5 (0.13 g) was first dissolved in a mixture of DI water (16 ml) and ethanol (4 ml).^[85] The solution was then directly transferred to a microwave heating system (Discover SP system, CEM) and reacted at 180 °C for 15 min under magnetic

stirring using a maximum microwave power of 150 W. The resultant powders were then annealed at 400 °C in air for 1 hour to obtain α -MoO₃. This sample is referred to as ST-MoO₃ in the following sections.

A third α -MoO₃ was synthesized using nitric acid as an oxidizing agent. The precursor, MoCl₅ (0.27 g), was first dissolved in a mixture of DI water (15 ml) and ethanol (5ml) as a solvent. Nitric acid (0.25 ml), an oxidizing agent, and citric acid (100 mg), a particle size control agent, were both added to the precursor solution. Next, the solution was directly transferred to a microwave heating system (Discover SP system, CEM) and reacted at 180 °C for 15 min under magnetic stirring using a maximum microwave power of 150 W. The resultant product was finally collected using centrifugation and washed with DI-water. The precipitates were dried at 60 °C in air. This sample is referred to as N-MoO₃ in this study.

Chapter 4.3.3. Material characterization

The crystalline structure of the bronzes and precursor oxides were identified using a powder X-ray diffractometer (Rigaku MiniFlex II) with Cu-K α (λ =1.54 Å) radiation. The particle size and morphology were characterized by transmission electron microscopy (TEM; CM 120, FEI) and scanning electron microscopy (SEM; Nova 230 Nano SEM). Thermogravimetric analysis (TGA, SDT Q-600, TA instruments) was used for thermal annealing during the Na_{0.9}Mo₆O₁₇ synthesis. Raman spectroscopy (Renishaw inVia with 514 laser) and Fourier transform infrared spectroscopy (FT-IR, FT-IR 670, JASCO) were utilized to identify metal-oxygen bonds in α -MoO₃.

Chapter 4.3.4. Electrochemical characterization

For Na_xWO_3 , cyclic voltammetry (CV) was first conducted using a three electrode cell with 1M Na_2SO_4 electrolyte. To prepare the working electrode, the synthesized particles were mixed with a conductive carbon (Ketjen Black) and polyvinylidene fluoride binder (PVDF) in the ratio of 75: 20: 5 weight percent, respectively. The mixture was added to propylene carbonate (PC) and electrodes were formed by dip coating stainless steel mesh (working electrode) into the PC suspension. A heat gun was used to dry the electrodes, and residual water was removed by vacuum drying at 10^{-3} torr and 70°C for 1 day. Platinum foil and Ag/AgCl were used as counter and reference electrode, respectively. To obtain power and energy density of Na_xWO_3 , galvanostatic measurements were performed with activated carbon having surface area of $\sim 1000 \text{ m}^2/\text{g}$ as a cathode material. The cathode is prepared by drop casting a slurry with 95 % activated carbon and 5 % PVDF on stainless steel mesh. Both electrodes were finally assembled and galvanostatically cycled in a three neck flask containing 1M Na_2SO_4 electrolyte. Energy and power density was calculated in this study using following equations,

$$\text{Energy density (E)} = 1/2 \cdot C \cdot V^2$$

$$\text{Power density (P)} = I \cdot V$$

where C is the capacitance value, V is potential range applied, and I is current density.

For $\text{Na}_{0.9}\text{Mo}_6\text{O}_{17}$, electrochemical measurements were performed in a three-electrode cell with a thin film of $\text{Na}_{0.9}\text{Mo}_6\text{O}_{17}$ serving as the working electrode. To prepare the working

electrode, $\text{Na}_{0.9}\text{Mo}_6\text{O}_{17}$ ($\sim 20 \mu\text{g}$) was cast from an ethanol solution onto an oxygen-plasma treated stainless steel foil ($\sim 1 \text{ cm}^2$ area), which was subsequently heated at 110°C for one hour to evaporate the ethanol. The mass of the particles deposited on the stainless steel foil was determined using a microbalance. The electrolytes used were 1M LiClO_4 or 1M NaClO_4 in propylene carbonate. Lithium or sodium metal foils were used as the counter and reference electrodes. Cyclic voltammetry was performed between 1.2 and 3.2 V vs. Li/Li^+ (or Na/Na^+) using a PAR EG&G 273A Potentiostat. All tests were performed in an argon-filled glovebox, with oxygen and water levels of $< 1 \text{ ppm}$.

Chapter 4.4. Results and Discussion

Chapter 4.4.1. Synthesis and characterization of Sodium tungsten bronze (Na_xWO_3)

Crystalline structure of the synthesized Na_xWO_3 was identified using X-ray diffraction. The XRD pattern of Na_xWO_3 synthesized in this study (Figure 4.5) is well matched with cubic $\text{Na}_{0.85}\text{WO}_3$ (JCPDS 75-0295). In addition, the color of the particles was orange, which is in good agreement with the relationship between color and sodium content x in Na_xWO_3 (Figure 4.1). Figure 4.6 shows that the shape of the $\text{Na}_{0.85}\text{WO}_3$ particles is cubic and the length of each side is 200~300 nm.

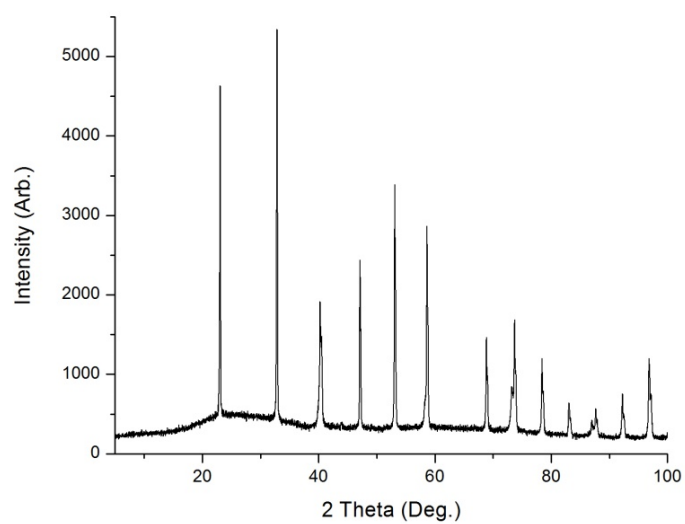


Figure 4.5. XRD pattern of $\text{Na}_{0.85}\text{WO}_3$

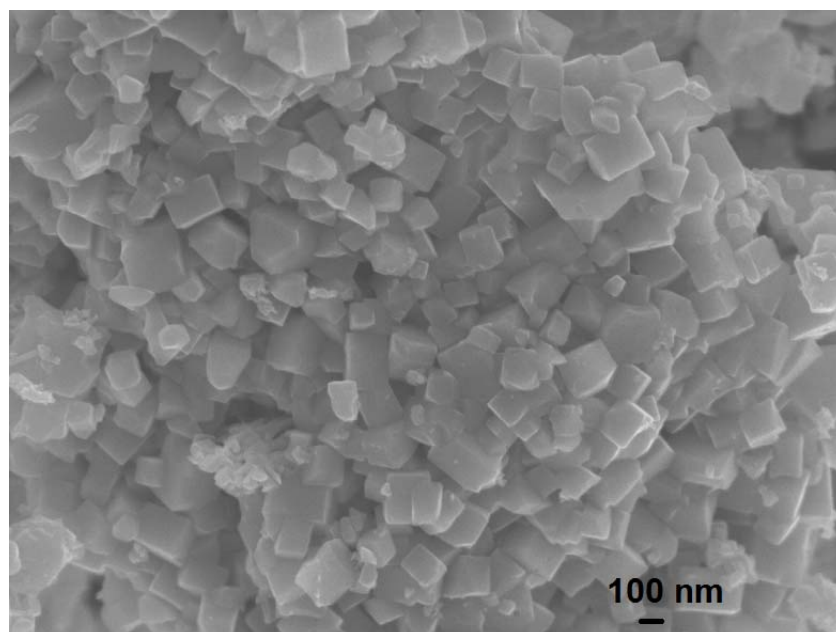


Figure 4.6. Scanning Electron Microscopy (SEM) image of Na_xWO_3 ($x=0.85$)

Chapter 4.4.2. Electrochemical behavior of Sodium tungsten bronze ($\text{Na}_{0.85}\text{WO}_3$)

To investigate the nature of electrochemical behavior of $\text{Na}_{0.85}\text{WO}_3$, cyclic voltammetry with various sweep rates was conducted. Aqueous Na_2SO_4 (1M) was used as an electrolyte to investigate if sodium ions can be inserted and/or de-inserted in Na_xWO_3 . The shape of the CV curves, and the fact that the specific capacitances at different scan rates are similar, indicate that the current responses are capacitive (Figure 4.7). This capacitive behavior results from the metallic state of $\text{Na}_{0.85}\text{WO}_3$. Since there are no redox peaks, most of the current is from electrochemical double layer contributions which are highly affected by the surface area of the materials. Thus, the capacitance of $\text{Na}_{0.85}\text{WO}_3$ is low ($< 50 \text{ F/g}$) due to its large particle size (200 \sim 300 nm) (Figure 4.6).

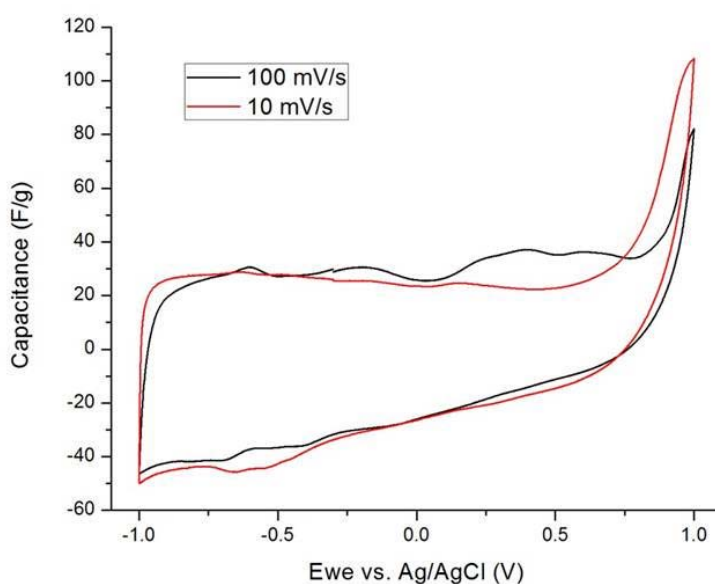


Figure 4.7. CV curves of $\text{Na}_{0.85}\text{WO}_3$ at different sweep rates

With the sodium tungsten bronze ($\text{Na}_{0.85}\text{WO}_3$) in the metallic state, we also carried out galvanostatic experiments using activated carbon as the counter electrode. In this way, we constructed an asymmetric electrochemical capacitor and were able to characterize the energy and power densities of the device. Figure 4.8 shows the galvanostatic charge/discharge curves at different current density. The energy and power density calculated based on the galvanostatic charge/discharge curves (Figure 4.9) are superimposed onto a graph from reference [86] that includes a number of commercial electrochemical capacitor devices. It is evident that the asymmetric capacitor containing Na_xWO_3 performs comparably. The point here is that when the Na_xWO_3 is in the metallic state, it functions as a respectable capacitor that can provide 10 Wh/kg of energy storage at a power density of about 100 W/kg.

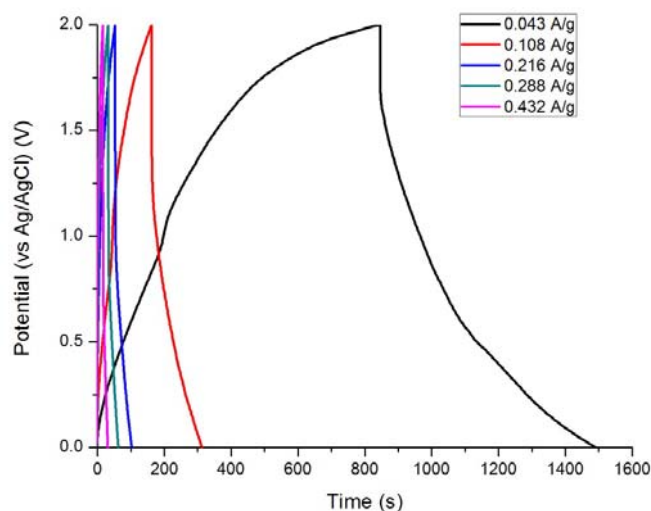


Figure 4.8. Galvanostatic charge/discharge curves of $\text{Na}_{0.85}\text{WO}_3$

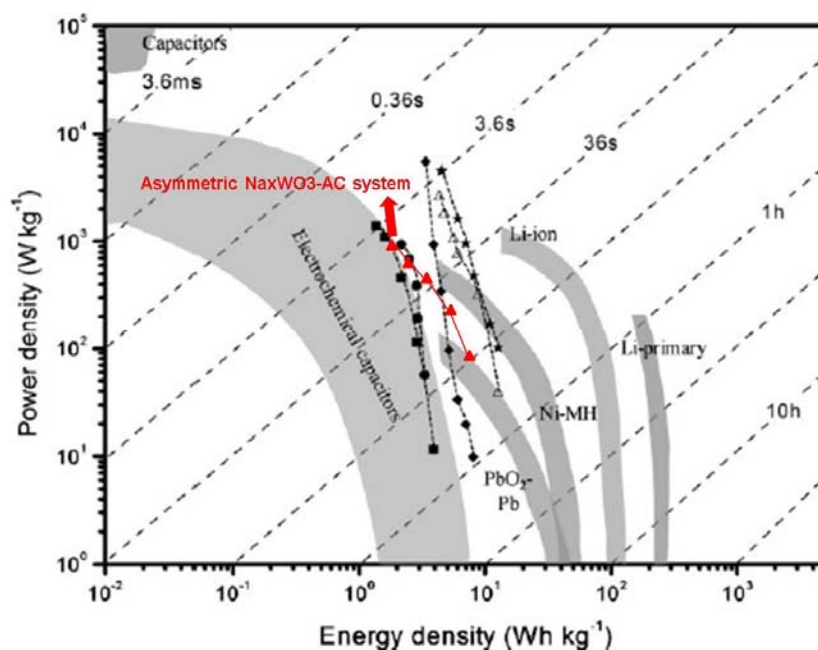


Figure 4.9. Ragone plot showing the energy and power density spectrum for an asymmetric electrochemical capacitor Na_xWO_3 – activated carbon. The device characteristics are shown in red. The other samples represent other types of carbon-based capacitors (after reference [86])

Chapter 4.4.3. Synthesis and characterization of $\alpha\text{-MoO}_3$ and $\text{Na}_{0.9}\text{Mo}_6\text{O}_{17}$

First $\alpha\text{-MoO}_3$ is synthesized by annealing amorphous MoO_3 aerogels. The aerogels were fabricated using epoxide-mediated sol-gel plus polyacrylic acid (PAA). It is well-known that the oxo form ($\text{Mo}=\text{O}$) is readily generated when the molybdenum precursor is hydrolyzed, because of its high valence ($z=+6$) (Figure 4.10).^[87] This oxo ($\text{M}=\text{O}$) form is stable enough to suppress 3-D network gelation.^[88] However, gelation of MoO_3 can be promoted in the presence of PAA having many carboxyl groups, because the strong coordination between PAA and Mo ions resists the formation of the $\text{M}=\text{O}$ bonding.^[84] The as-synthesized MoO_3 aerogel in this study was

amorphous and became crystalline after thermal annealing at 400°C for 2 hrs (Figure 4.11). The peaks for crystalline MoO₃ correspond to the orthorhombic α -MoO₃ (JCPDS 50-508).

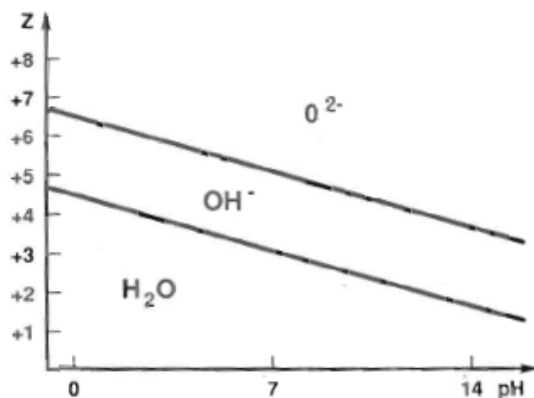


Figure 4.10. Charge (z) versus pH diagram^[87]; the ‘aquo (M-(OH)₂)’, ‘hydroxo (M-OH)’ and ‘oxo (M=O)’ domains depend on valence of cation and pH.

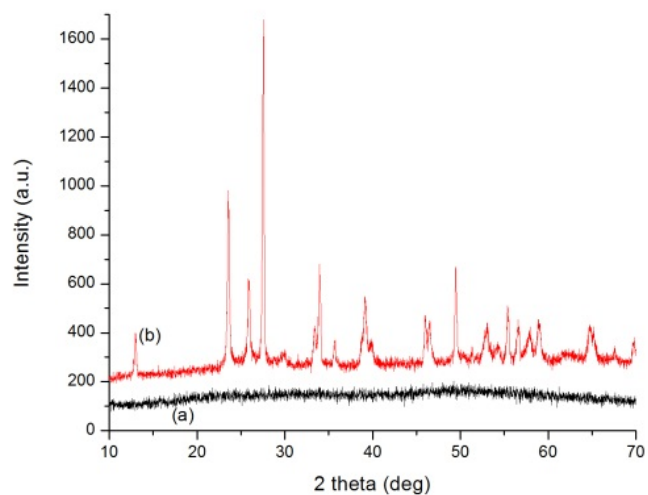


Figure 4.11. XRD patterns for (a) as-synthesized MoO₃ aerogel and (b) MoO₃ aerogel after thermal annealing at 400°C

Both Raman and FT-IR studies on the crystalline MoO_3 further confirm the $\alpha\text{-MoO}_3$ formation. The peak at 986 cm^{-1} in Raman (Figure 4.12) and at 991 cm^{-1} in FT-IR (Figure 4.13) are the characteristic peaks for $\text{Mo}^{6+}=\text{O}$ stretching in $\alpha\text{-MoO}_3$, which the β phase of MoO_3 does not show.^[89] The peaks at 813 and 656 cm^{-1} in Raman represents the presence of $\text{Mo}^{6+}_2\text{-O}$ (corner sharing) and $\text{Mo}^{6+}_3\text{-O}$ (edge sharing), respectively, which are also detected at 858 cm^{-1} ($\text{Mo}_2\text{-O}$) and 613 cm^{-1} ($\text{Mo}_3\text{-O}$) in FT-IR.^[90]

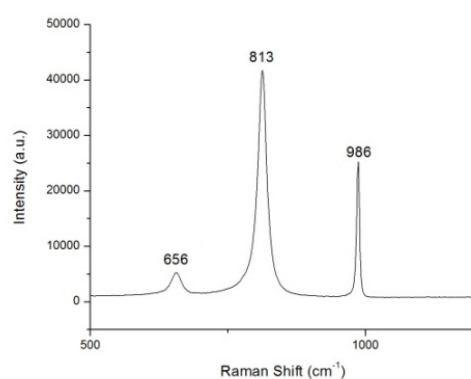


Figure 4.12. Raman spectrum of MoO_3 aerogel annealed at $400\text{ }^{\circ}\text{C}$

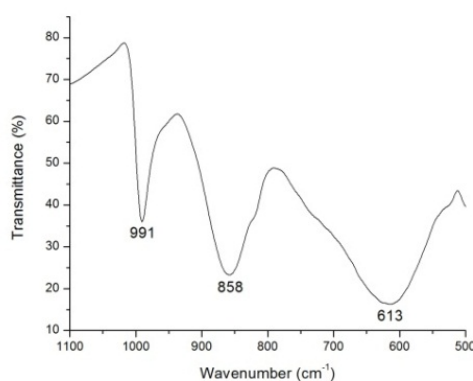


Figure 4.13. FT-IR spectrum of MoO_3 aerogel annealed at $400\text{ }^{\circ}\text{C}$

The morphology and particle size of the MoO_3 aerogel were characterized using TEM. Figure 4.14-(a) shows that the as-synthesized aerogel has a fibrous morphology and does not consist of particles. Upon thermal annealing of the aerogel, 500 nm particles were obtained (Figure 4.14-(b)).

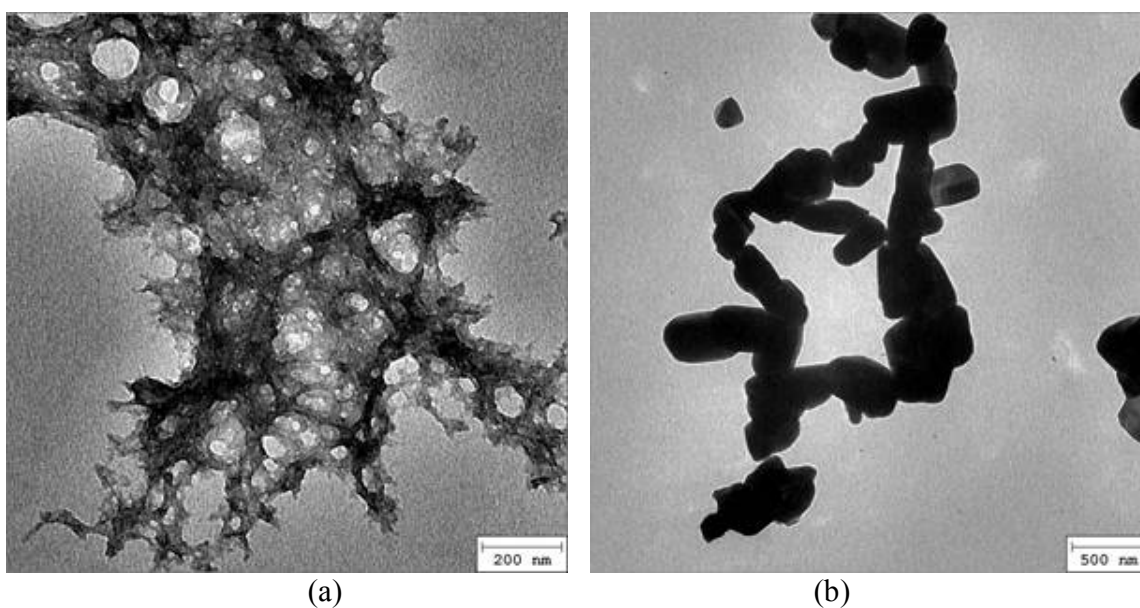


Figure 4.14. TEM images of (a) as-synthesized MoO_3 aerogel and (b) $\alpha\text{-MoO}_3$ after thermal annealing at 400°C

To fabricate smaller MoO_3 particles by using a different synthetic route, a microwave-assisted solvothermal method was used. Using a microwave as a heating source can dramatically reduce the reaction time to 10 ~ 15 min which is much faster than a typical parr-bomb synthesis (days). After using a mixture of DI water and ethanol as a solvent for the reaction, the XRD pattern indicates that the black powders obtained are MoO_2 (JCPDS 78-1073) (Figure 4.15-(a)). During heat treatment at 450°C in air for 2hrs, the color of the particles changes to light blue

associated with a phase transition to α -MoO₃ (JCPDS 05-0508) as shown in Figure 4.15-(b). In addition, the particle size increases from ~20 nm to 300-400 nm in diameter as shown in Figure 4.16.

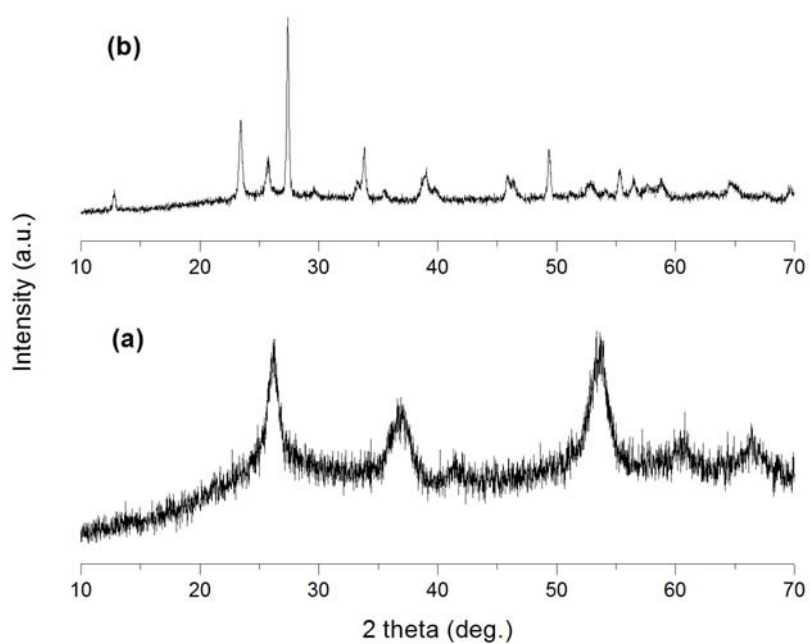


Figure 4.15. XRD patterns of MoO_x synthesized by microwave-assisted solvothermal reaction using co-solvent (DI water + ethanol); (a) As-synthesized MoO₂ and (b) After heat treatment at 450 °C in air (ST-MoO₃)

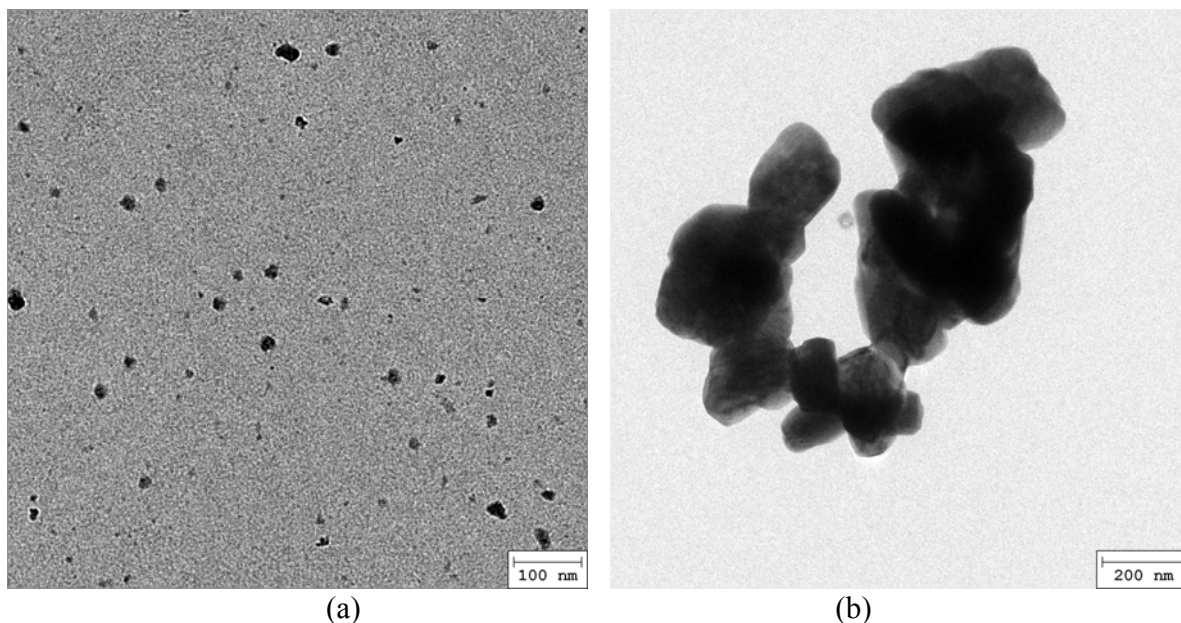


Figure 4.16. TEM images of MoO_x synthesized by microwave-assisted solvothermal reaction using co-solvent (DI water + ethanol); (a) As-synthesized MoO_2 and (b) After heat treatment at $450\text{ }^\circ\text{C}$ in air (ST- MoO_3)

To further control the size and morphology of $\alpha\text{-MoO}_3$, the precursor (MoCl_5) in water/ethanol solvent was solvothermally reacted in the presence of nitric acid which serves as an oxidizing agent. As shown in Figure 4.17, the as-synthesized particles are $\alpha\text{-MoO}_3$ (JCPDS 05-0508) without any heat treatment. This indicates that nitric acid plays an important role in obtaining $\alpha\text{-MoO}_3$, not MoO_2 . However, the resultant morphology is a wire ($3\sim 4\text{ }\mu\text{m}$ in length) rather than a particle (Figure 4.18).

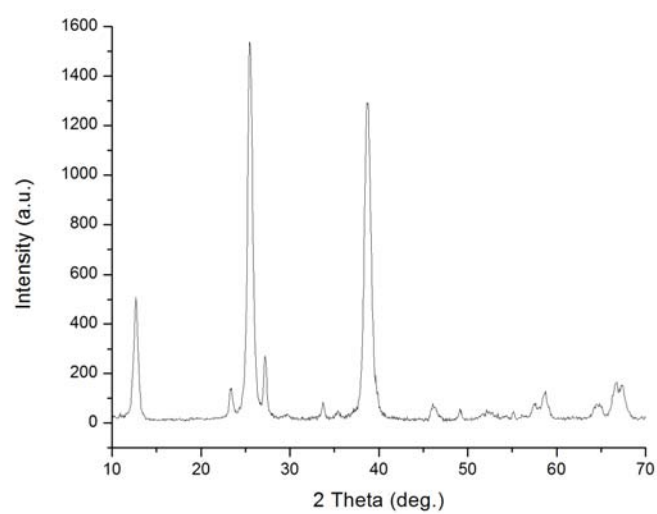


Figure 4.17. XRD pattern of N-MoO₃

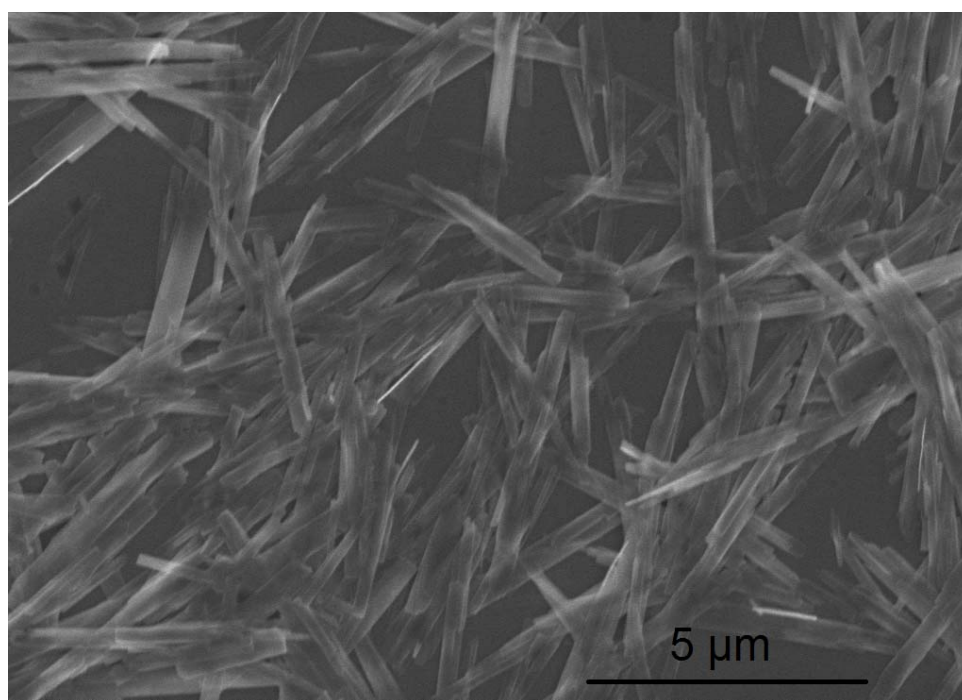


Figure 4.18. SEM image of N-MoO₃

Sodium molybdenum bronzes ($\text{Na}_{0.9}\text{Mo}_6\text{O}_{17}$) were then fabricated using $\alpha\text{-MoO}_3$ as a precursor material in this study. In the synthesis, it is critical that $\text{Na}_2\text{S}_2\text{O}_4$ (reducing agent) and $\text{Na}_2\text{MoO}_4 \cdot 2\text{H}_2\text{O}$ (molybdate buffer) were simultaneously added to $\alpha\text{-MoO}_3$ suspension (water solvent).^[83] If $\text{Na}_2\text{S}_2\text{O}_4$ is added before the molybdate buffer, the reduction of MoO_3 leads to the uptake of protons which could not be displaced by Na^+ , and if the molybdate buffer was added before $\text{Na}_2\text{S}_2\text{O}_4$, $\alpha\text{-MoO}_3$ is consumed as following eqn. (1) due to the proton uptake by the buffer.



X-ray diffraction data (Figure 4.19-(a)) shows that as-synthesized particles are a mixture of two different hydrated sodium molybdenum bronzes, $(\text{Na}(\text{H}_2\text{O})_2)_{0.25}\text{MoO}_3$ (JCPDS 39-0634) and $(\text{Na}(\text{H}_2\text{O})_5)_{0.25}\text{MoO}_3$ (JCPDS 39-1112). To obtain $\text{Na}_{0.9}\text{Mo}_6\text{O}_{17}$, the as-synthesized powders were heat treated up to 400 °C by TGA in an Ar atmosphere. Two endothermic peaks around 78 °C and 192 °C in DTA (Figure 4.20) are attributed to the first and second removal of the hydrated water, respectively.^[91] Both exothermic peaks at 320 °C and 365 °C are associated with the $\text{Na}_{0.9}\text{Mo}_6\text{O}_{17}$ formation.^[91] These formation temperatures are lower than the melting points of the sample by ~ 200 K. These facts indicate that the formation proceeds directly from the hydrated bronzes in the solid-phase process^[91], which is different from a mechanism by usual methods. By the usual methods, the formation proceeds in the liquid phase and via intermediate products with similar structures. XRD of this sample (Figure 4.19-(b)) confirms that $\text{Na}_{0.9}\text{Mo}_6\text{O}_{17}$ (JCPDS 86-1683) is formed during the heat treatment. However, it is observed that

there is also a small amount of $\text{Na}_2\text{Mo}_2\text{O}_7$. The color of the powders changed from dark blue to purple after the heat treatment, which is also indicative of the formation of $\text{Na}_{0.9}\text{Mo}_6\text{O}_{17}$.

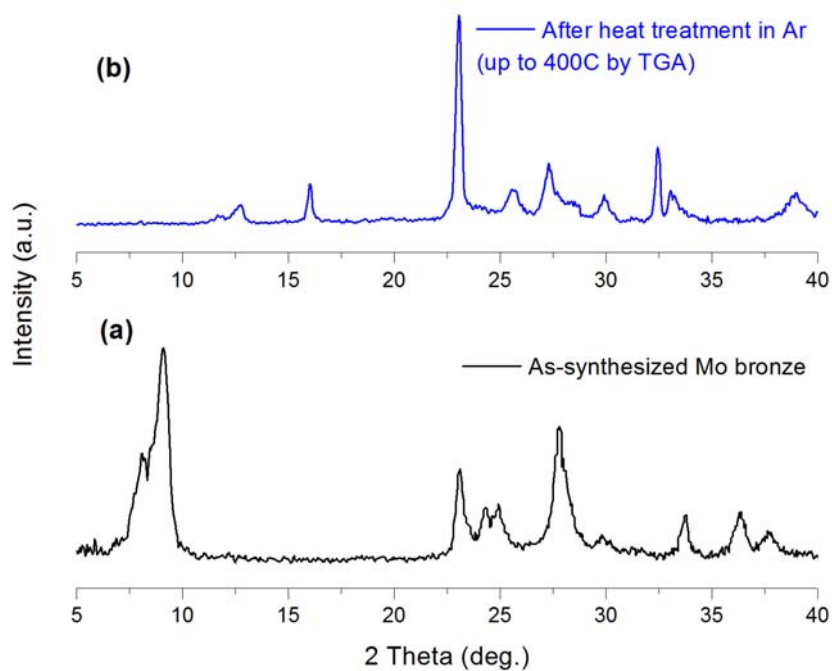


Figure 4.19. XRD pattern of Mo bronzes; (a) as-synthesized and (b) after heat treatment at 400 °C in Ar

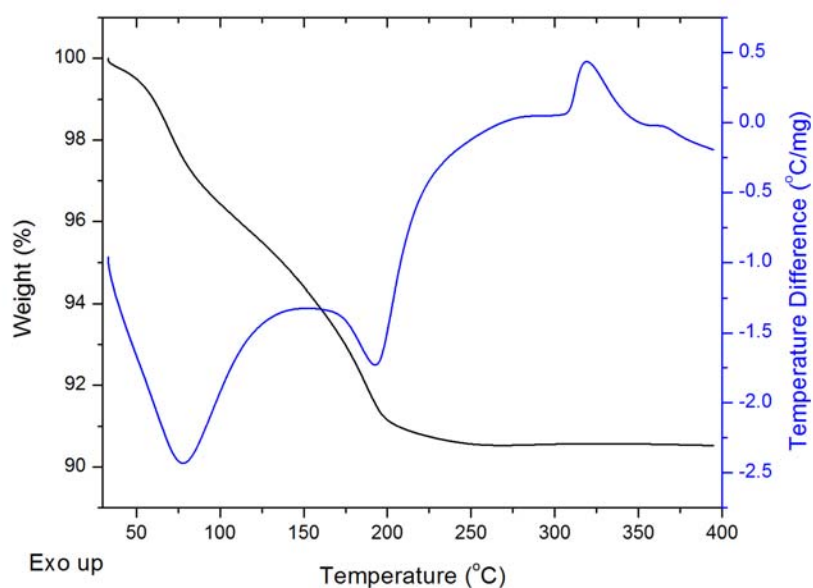


Figure 4.20. TGA and DTA on the hydrated sodium molybdenum bronze in Ar atmosphere

The morphology and size of $\text{Na}_{0.9}\text{Mo}_6\text{O}_{17}$ prepared in this study are varied depending on $\alpha\text{-MoO}_3$ used in the synthesis. When ST- MoO_3 is used, 200 ~ 500 nm (in dia.) of $\text{Na}_{0.9}\text{Mo}_6\text{O}_{17}$ particles were formed as shown in Figure 4.21. When N- MoO_3 is used, most of the wire morphology of N- MoO_3 is broken and ~200 nm $\text{Na}_{0.9}\text{Mo}_6\text{O}_{17}$ particles were obtained (Figure 4.22).

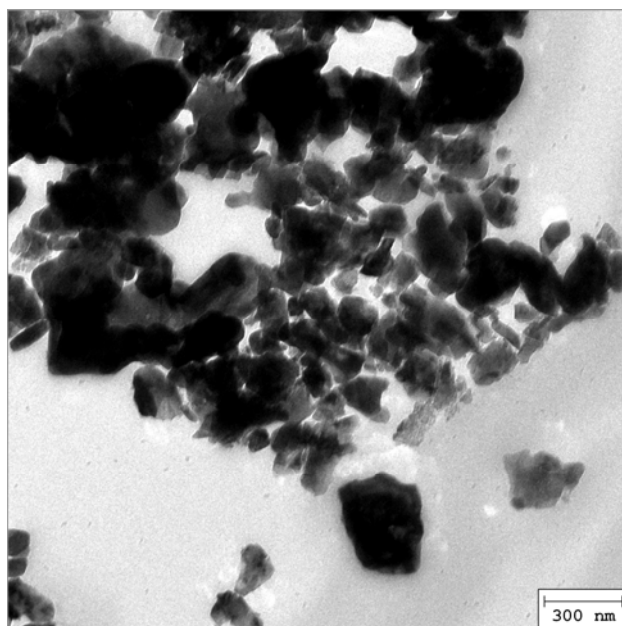


Figure 4.21. TEM image of $\text{Na}_{0.9}\text{Mo}_6\text{O}_{17}$ synthesized using ST- MoO_3

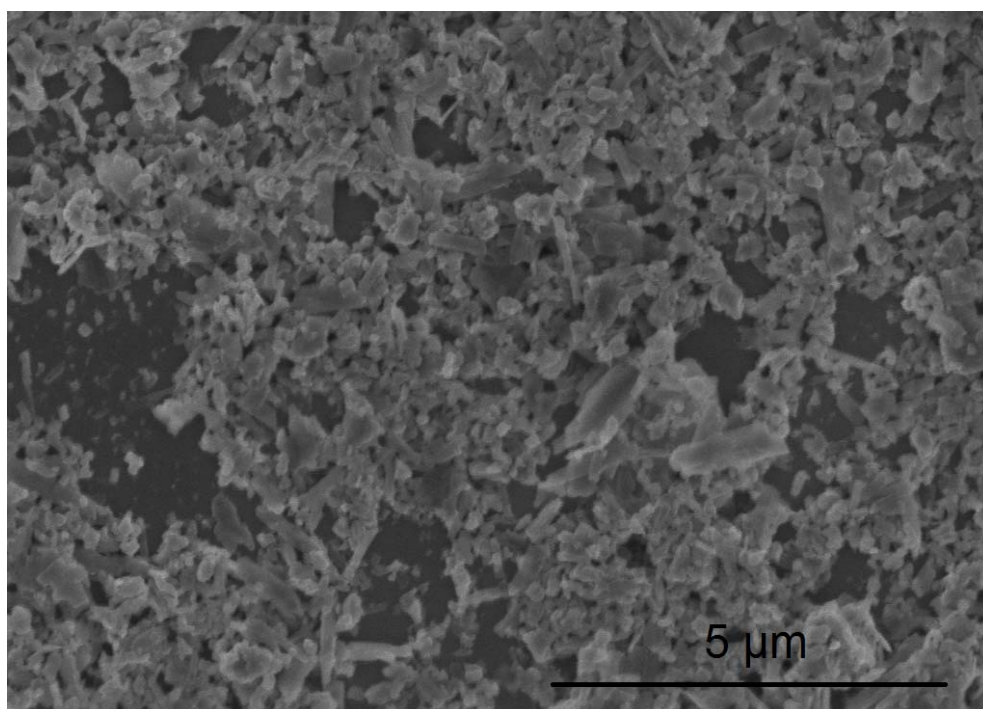


Figure 4.22. SEM image of $\text{Na}_{0.9}\text{Mo}_6\text{O}_{17}$ synthesized using N- MoO_3

Chapter 4.4.4. Electrochemical behavior of Sodium molybdenum bronze ($\text{Na}_{0.9}\text{Mo}_6\text{O}_{17}$)

To investigate the electrochemical property of $\text{Na}_{0.9}\text{Mo}_6\text{O}_{17}$, cyclic voltammetry (CV) was performed using a three-electrode cell with LiClO_4 or NaClO_4 as an electrolyte. Figure 4.23 shows the CV curves of $\text{Na}_{0.9}\text{Mo}_6\text{O}_{17}$ synthesized using ST- MoO_3 at 10 mV/s. For the Li-based electrolyte, there are two anodic peaks at 1.7 and 2.6 V (vs. Li/Li^+), whereas there is no apparent cathodic peak. For the Na-based electrolyte, there are no redox peaks and the specific current from the electrode is much smaller compared to the Li-based electrolyte. Based on the CV curves, specific capacity was calculated and plotted as a function of sweep rate for both electrolytes (Figure 4.24). For the Li-based electrolyte, the capacity decreases as the applied sweep rate increases (552 C/g at 2 mV/s and 248 C/g at 100 mV/s). The capacity for the Na-based electrolyte is less than 100 C/g at all sweep rates (2 ~ 100 mV/s). As a result, the electrolytes having different sized ions indicate that charge storage of $\text{Na}_{0.9}\text{Mo}_6\text{O}_{17}$ occurs not only on the surface but also in the bulk.

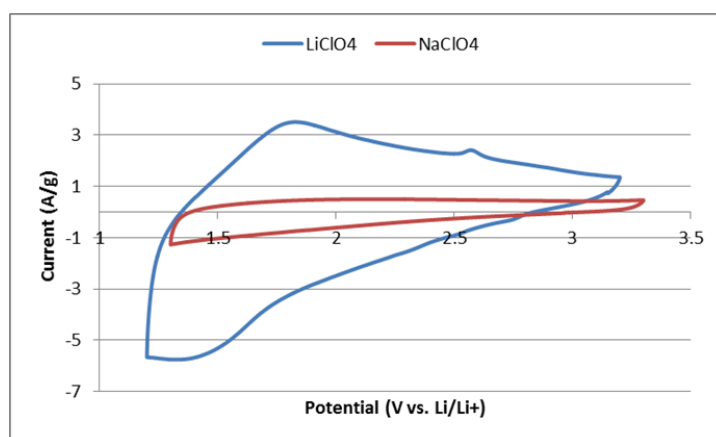


Figure 4.23. CV curves of $\text{Na}_{0.9}\text{Mo}_6\text{O}_{17}$ synthesized using ST- MoO_3 with different electrolyte ions (Li^+ and Na^+) at the sweep rate of 10 mV/s

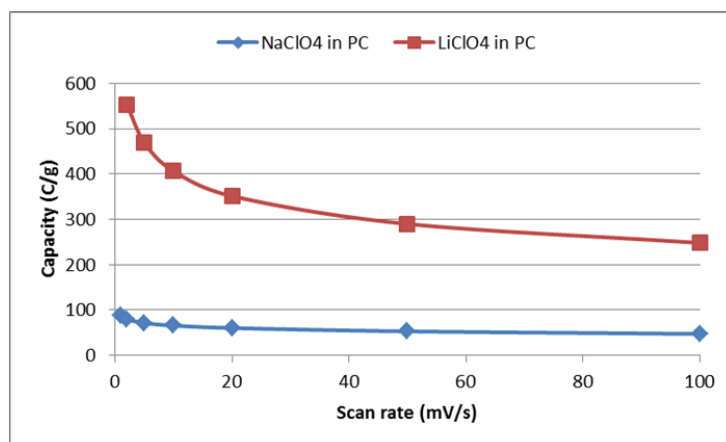


Figure 4.24. The capacity of $\text{Na}_{0.9}\text{Mo}_6\text{O}_{17}$ synthesized using ST- MoO_3 with different electrolyte ions (Li^+ and Na^+) at different sweep rates

The same electrochemical measurements were performed using LiClO_4 electrolyte for $\text{Na}_{0.9}\text{Mo}_6\text{O}_{17}$ synthesized using N- MoO_3 . As shown in Figure 4.25, there are two distinct cathodic peaks around 2.3 V and 1.6 V as well as anodic peaks around 1.8 V and 2.5 V, which is different from $\text{Na}_{0.9}\text{Mo}_6\text{O}_{17}$ synthesized using ST- MoO_3 . Those peaks are apparent at all sweep rates (1 – 100 mV/s). The capacity of $\text{Na}_{0.9}\text{Mo}_6\text{O}_{17}$ synthesized using N- MoO_3 , however, is slightly lower than $\text{Na}_{0.9}\text{Mo}_6\text{O}_{17}$ synthesized using ST- MoO_3 (442 C/g at 2 mV/s and 181 C/g at 100 mV/s) (Figure 4.26). To investigate the kinetic behavior of $\text{Na}_{0.9}\text{Mo}_6\text{O}_{17}$ synthesized using N- MoO_3 , b-value characterization was performed. Figure 4.27 demonstrates that b-values for the cathodic and anodic peak are 0.82 and 0.79, respectively. As explained in Chapter 3, these values indicate that the current response from $\text{Na}_{0.9}\text{Mo}_6\text{O}_{17}$ synthesized using N- MoO_3 is not fully capacitive, and limited by diffusion.

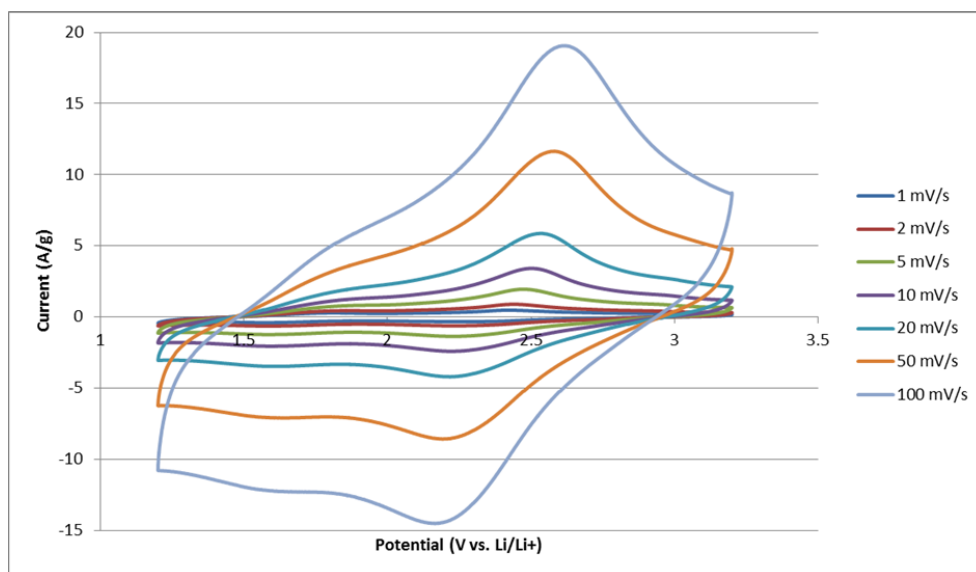


Figure 4.25. CV curve of $\text{Na}_{0.9}\text{Mo}_6\text{O}_{17}$ synthesized using N-MoO_3 at different sweep rates (2 - 100 mV/s)

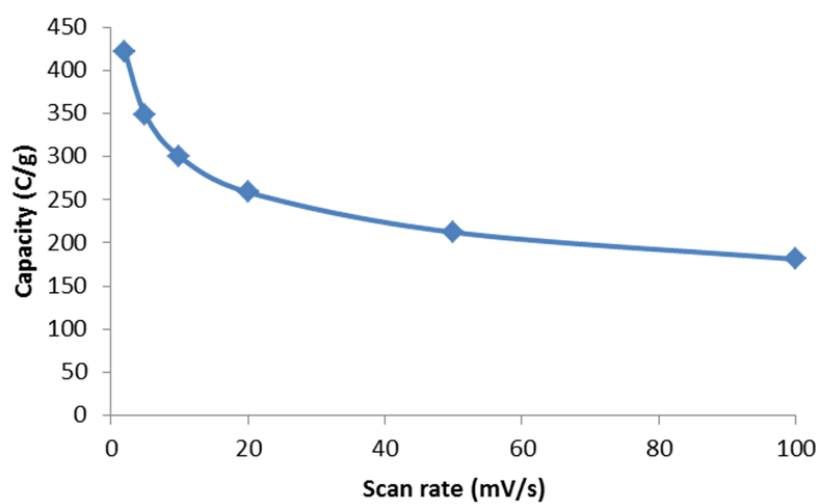


Figure 4.26. The capacity of $\text{Na}_{0.9}\text{Mo}_6\text{O}_{17}$ synthesized using N-MoO_3

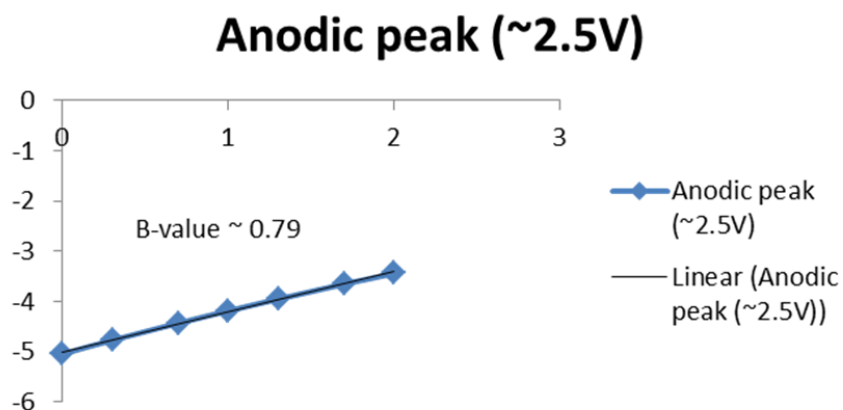
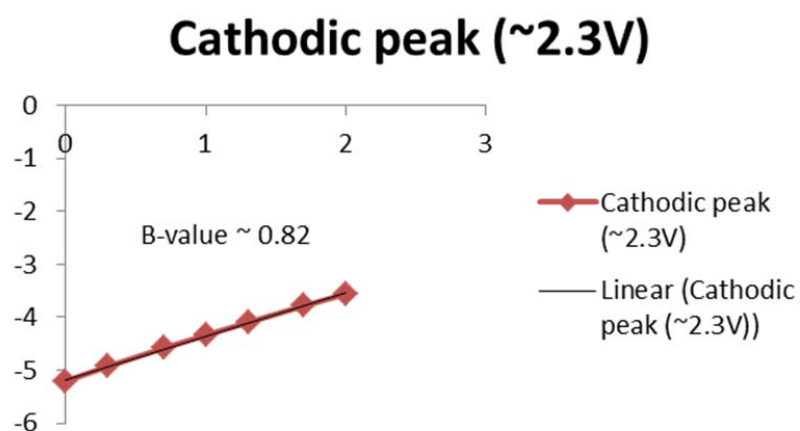


Figure 4.27. b-value characterization for $\text{Na}_{0.9}\text{Mo}_6\text{O}_{17}$ synthesized using N-MoO₃; (a) at cathodic peak, (b) at anodic peak

Chapter 4.5. Suggestions for future work

The Na_xWO_3 and $\text{Na}_{0.9}\text{Mo}_6\text{O}_{17}$ investigated in this study are not in the nanoscale regime (< 100 nm). For $\text{Na}_{0.9}\text{Mo}_6\text{O}_{17}$, reducing the particle size would be the critical step needed to

reduce the diffusion contribution which was observed in this research. To synthesize nanoscale $\text{Na}_{0.9}\text{Mo}_6\text{O}_{17}$, the precursor material size of $\alpha\text{-MoO}_3$ is important. However, making $\alpha\text{-MoO}_3$ nanoparticles is a challenge. For most syntheses without using acid, MoO_2 is formed, so an annealing process at $400 \sim 450^\circ\text{C}$ is required to form $\alpha\text{-MoO}_3$. However, annealing at such temperatures results in significant particle size growth. Adding acid to the reaction helps to prevent the formation of $\alpha\text{-MoO}_3$ without annealing, but a fibrous or wire morphology is always obtained rather than nanoparticles^[92]. As preliminary TGA & DTA data (Figure 4.28) show, MoO_2 nanoparticles can be oxidized at lower temperatures ($\sim 300^\circ\text{C}$). Thus, it would be worth trying to anneal MoO_2 nanoparticles at lower temperatures to minimize particle growth while phase transformations occur. Using mesoporous MoO_3 as a precursor material for $\text{Na}_{0.9}\text{Mo}_6\text{O}_{17}$ would also be interesting because it is able to render the pore walls less than 50 nm ^[93].

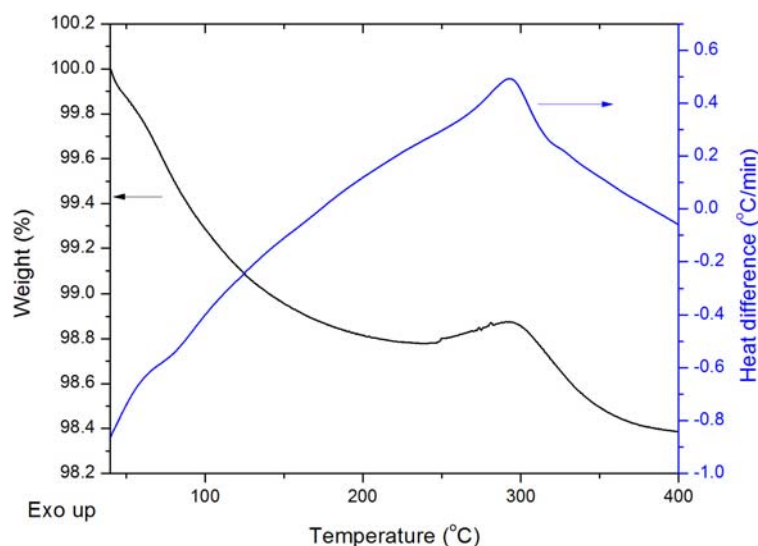


Figure 4.28. TGA & DTA of MoO_2 synthesized via microwave-assisted hydrothermal process

It is also necessary to extend electrochemical studies on both Na_xWO_3 and $\text{Na}_{0.9}\text{Mo}_6\text{O}_{17}$. Because we started to cycle both bronzes which are in the metallic state, it will be necessary to de-intercalate sodium (Na^+) first in order to obtain a non-metallic state, while maintaining the structure. Consequently, electrodes can be charged and discharged galvanostatically to investigate its electrochemical behavior as a battery material.

Chapter 5. Conclusions

Previous research on transition metal oxides for electrochemical capacitors largely focused on RuO_2 and MnO_2 . In this dissertation, we found that Nb_2O_5 can also be considered as an excellent material for electrochemical capacitors. By investigating the effect of crystalline structure of Nb_2O_5 on its pseudocapacitive behavior, it is evident that charge storage in Nb_2O_5 occurs by intercalation/deintercalation processes rather than ion adsorption/desorption processes or redox reactions on the surface of the material. The extrapolated infinite sweep rate capacitance ($\sim 400 \text{ F/g}$) of Nb_2O_5 exceeds that of birnessite MnO_2 and is comparable to values obtained for RuO_2 , indicating that the kinetics of Nb_2O_5 is outstanding even though electrolyte ions intercalate or deintercalate into the bulk of Nb_2O_5 (i.e. intercalation pseudocapacitance) without phase transformations. This research on Nb_2O_5 as a pseudocapacitive material suggests that this new charge storage mechanism, intercalation pseudocapacitance, can become one of the most important directions for obtaining high power density as well as high energy density.

The second part of this dissertation involved a study on the synthesis and electrochemical behavior of oxide/carbon nanocomposites as a pseudocapacitive material. The core-shell structure (0D) investigated in this research differs significantly from common composite morphologies such as 1D (oxide/CNT) and 2D (oxide/graphene). Nb_2O_5 was chosen as a core material in that its insulating nature is a critical factor in limiting practical use even though its electrochemical properties are intriguing as mentioned above. In this research, we showed that the microwave-assisted hydrothermal method is a very effective approach for synthesizing the core-shell structure. Electrochemical measurements on the core-shell structure demonstrated that

electrolyte ion transport through the shell is a more important factor than electronic conductivity when fast charge/discharge (seconds or minutes) is involved. We showed that the ionic conductivity through the shell can be dramatically improved by oxidation processes using nitric acid. Upon oxidation, the capacity and kinetics of the $\text{Nb}_2\text{O}_5/\text{C}$ core-shell becomes comparable to that of bare Nb_2O_5 . As mass loading of electrode materials increases, use of core-shell structure becomes more beneficial. Due to the complete carbon coating on Nb_2O_5 , an electrode consisting of $\text{Nb}_2\text{O}_5/\text{C}$ core-shell particles (~ 0.5 mg) without carbon additive has higher capacity and better rate capability than bare Nb_2O_5 with carbon additive. Thus, the core-shell structure can make Nb_2O_5 to be more practical and attractive for energy storage systems such as power grids.

Another part of this dissertation involved a study of reconfigurable electrodes for both high energy density and power density. The concept used in this study is that a material in which electrical properties change depending on the amount of guest ions in a certain material framework can be used either as battery material (in the insulating state) or an electrochemical capacitor material (in the metallic state). This concept is beneficial especially for electric vehicles which require both high energy and power. Metal oxide bronzes such as Na_xWO_3 and Na_xMoO_3 were of interest in this study. It remains a challenge to synthesize nanoscale particles of bronzes. Despite the submicron size of the materials, both bronzes in the metallic state perform effectively as electrochemical capacitor materials.

References

- [1] M. Winter, R. J. Brodd, *Chemical Reviews* **2004**, *104*, 4245.
- [2] P. Simon, Y. Gogotsi, *Nat Mater* **2008**, *7*, 845.
- [3] C. Largeot, C. Portet, J. Chmiola, P.-L. Taberna, Y. Gogotsi, P. Simon, *Journal of the American Chemical Society* **2008**, *130*, 2730.
- [4] B. E. Conway, in *Kluwer-Academic*, **1999**.
- [5] Y. F. Yuan, X. H. Xia, J. B. Wu, J. L. Yang, Y. B. Chen, S. Y. Guo, *Electrochimica Acta* **2011**, *56*, 2627.
- [6] M. Toupin, T. Brousse, D. Belanger, *Chemistry of Materials* **2004**, *16*, 3184.
- [7] I.-H. Kim, J.-H. Kim, B.-W. Cho, K.-B. Kim, *Journal of The Electrochemical Society* **2006**, *153*, A1451.
- [8] O. Ghodbane, J.-L. Pascal, F. d. r. Favier, *ACS Applied Materials & Interfaces* **2009**, *1*, 1130.
- [9] K. Brezesinski, J. Wang, J. Haetge, C. Reitz, S. O. Steinmueller, S. H. Tolbert, B. M. Smarsly, B. Dunn, T. Brezesinski, *Journal of the American Chemical Society* **2010**, *132*, 6982.
- [10] B. Reichman, A. J. Bard, *Journal of The Electrochemical Society* **1980**, *127*, 241.
- [11] B. Reichman, A. J. Bard, *Journal of The Electrochemical Society* **1981**, *128*, 344.
- [12] R. Kodama, Y. Terada, I. Nakai, S. Komaba, N. Kumagai, *Journal of The Electrochemical Society* **2006**, *153*, A583.
- [13] B. Orel, M. Maček, J. Grdadolnik, A. Meden, *Journal of Solid State Electrochemistry* **1998**, *2*, 221.

- [14] R. J. Cava, B. Batlogg, J. J. Krajewski, H. F. Poulsen, P. Gammel, W. F. Peck, L. W. Rupp, *Physical Review B* **1991**, *44*, 6973.
- [15] D. A. B. de Filho, D. W. Franco, P. P. A. Filho, O. L. Alves, *Journal of Materials Science* **1998**, *33*, 2607.
- [16] I. Nowak, M. Ziolek, *Chemical Reviews* **1999**, *99*, 3603.
- [17] H. Schäfer, R. Gruehn, F. Schulte, *Angewandte Chemie International Edition in English* **1966**, *5*, 40.
- [18] K. Kato, S. Tamura, *Acta Crystallographica Section B* **1975**, *31*, 673.
- [19] B. M. Gatehouse, A. D. Wadsley, *Acta Crystallographica* **1964**, *17*, 1545.
- [20] B. E. Conway, V. Birss, J. Wojtowicz, *Journal of Power Sources* **1997**, *66*, 1.
- [21] A. S. Arico, P. Bruce, B. Scrosati, J.-M. Tarascon, W. van Schalkwijk, *Nat Mater* **2005**, *4*, 366.
- [22] J. P. Zheng, P. J. Cygan, T. R. Jow, *Journal of The Electrochemical Society* **1995**, *142*, 2699.
- [23] C.-C. Hu, W.-C. Chen, K.-H. Chang, *Journal of The Electrochemical Society* **2004**, *151*, A281.
- [24] J.-K. Chang, W.-T. Tsai, *Journal of The Electrochemical Society* **2003**, *150*, A1333.
- [25] J. W. Long, A. L. Young, D. R. Rolison, *Journal of The Electrochemical Society* **2003**, *150*, A1161.
- [26] J. Wang, J. Polleux, J. Lim, B. Dunn, *The Journal of Physical Chemistry C* **2007**, *111*, 14925.

- [27] F. Chaput, B. Dunn, P. Fuqua, K. Salloux, *Journal of Non-Crystalline Solids* **1995**, 188, 11.
- [28] J. Buha, D. Arcon, M. Niederberger, I. Djerdj, *Physical Chemistry Chemical Physics* **2010**, 12, 15537.
- [29] A. E. Gash, T. M. Tillotson, J. H. Satcher, J. F. Poco, L. W. Hrubesh, R. L. Simpson, *Chemistry of Materials* **2001**, 13, 999.
- [30] A. E. Gash, T. M. Tillotson, J. H. Satcher Jr, L. W. Hrubesh, R. L. Simpson, *Journal of Non-Crystalline Solids* **2001**, 285, 22.
- [31] A. Du, B. Zhou, J. Shen, S. Xiao, Z. Zhang, C. Liu, M. Zhang, *Journal of Non-Crystalline Solids* **2009**, 355, 175.
- [32] M. Niederberger, *Accounts of Chemical Research* **2007**, 40, 793.
- [33] J. M. Jehng, I. E. Wachs, *Chemistry of Materials* **1991**, 3, 100.
- [34] T. Ikeya, M. Senna, *Journal of Non-Crystalline Solids* **1988**, 105, 243.
- [35] T. Ohzuku, K. Sawai, T. Hirai, *Journal of Power Sources* **1987**, 19, 287.
- [36] A. Rosario, E. Pereira, *Journal of Solid State Electrochemistry* **2005**, 9, 665.
- [37] M. Schmitt, M. A. Aegerter, *Electrochimica Acta* **2001**, 46, 2105.
- [38] N. Kumagai, Y. Koishikawa, S. Komaba, N. Koshiba, *Journal of The Electrochemical Society* **1999**, 146, 3203.
- [39] R. D. Shannon, C. T. Prewitt, *Acta Crystallographica Section B* **1969**, 25, 925.
- [40] N. Kumagai, I. Ishiyama, K. Tanno, *Journal of Power Sources* **1987**, 20, 193.
- [41] M. S. Whittingham, A. J. Jacobson, Eds., *Intercalation chemistry*, Academic press, **1982**.
- [42] S. Ardizzone, G. Fregonara, S. Trasatti, *Electrochimica Acta* **1990**, 35, 263.

- [43] D. Baronetto, N. Krstajic, S. Trasatti, *Electrochimica Acta* **1994**, 39, 2359.
- [44] S.-B. Ma, K.-W. Nam, W.-S. Yoon, X.-Q. Yang, K.-Y. Ahn, K.-H. Oh, K.-B. Kim, *Journal of Power Sources* **2008**, 178, 483.
- [45] J. Jirkovsky, M. Makarova, P. Krtil, *Journal of The Electrochemical Society* **2005**, 152, A1613.
- [46] C. N. Chervin, A. M. Lubers, K. A. Pettigrew, J. W. Long, M. A. Westgate, J. J. Fontanella, D. R. Rolison, *Nano Letters* **2009**, 9, 2316.
- [47] C. Sassoey, C. Laberty, H. Le Khanh, S. Cassaignon, C. Boissière, M. Antonietti, C. Sanchez, *Advanced Functional Materials* **2009**, 19, 1922.
- [48] Ç. K. a. A. Zunger, *Appl. Phys. Lett.* **2002**, 81, 73.
- [49] Z. Chen, V. Augustyn, J. Wen, Y. Zhang, M. Shen, B. Dunn, Y. Lu, *Advanced Materials* **2011**, 23, 791.
- [50] Z. Fan, J. Yan, T. Wei, L. Zhi, G. Ning, T. Li, F. Wei, *Advanced Functional Materials* **2011**, 21, 2366.
- [51] R.-R. Bi, X.-L. Wu, F.-F. Cao, L.-Y. Jiang, Y.-G. Guo, L.-J. Wan, *The Journal of Physical Chemistry C* **2010**, 114, 2448.
- [52] J. Yan, Z. Fan, T. Wei, W. Qian, M. Zhang, F. Wei, *Carbon* **2010**, 48, 3825.
- [53] S. Lee, Y. Cho, H.-K. Song, K. T. Lee, J. Cho, *Angewandte Chemie International Edition* **2012**, 51, 8748.
- [54] J. Liu, W. Li, A. Manthiram, *Chemical Communications* **2010**, 46, 1437.
- [55] M. M. Rahman, J.-Z. Wang, M. F. Hassan, S. Chou, Z. Chen, H. K. Liu, *Energy & Environmental Science* **2011**, 4, 952.

- [56] L. Su, Y. Jing, Z. Zhou, *Nanoscale* **2011**, 3, 3967.
- [57] Y. Wang, Y. Wang, E. Hosono, K. Wang, H. Zhou, *Angewandte Chemie International Edition* **2008**, 47, 7461.
- [58] S. Yang, X. Feng, S. Ivanovici, K. Müllen, *Angewandte Chemie International Edition* **2010**, 49, 8408.
- [59] W.-M. Zhang, X.-L. Wu, J.-S. Hu, Y.-G. Guo, L.-J. Wan, *Advanced Functional Materials* **2008**, 18, 3941.
- [60] R. Liu, J. Duay, S. B. Lee, *Chemical Communications* **2011**, 47.
- [61] R. Liu, J. Duay, S. B. Lee, *Chemical Communications* **2011**, 47, 1384.
- [62] J. W. Kim, V. Augustyn, B. Dunn, *Advanced Energy Materials* **2012**, 2, 141.
- [63] M.-M. Titirici, M. Antonietti, N. Baccile, *Green Chemistry* **2008**, 10, 1204.
- [64] K. Aydinçak, T. Yumak, A. Sinag, B. Esen, *Industrial & Engineering Chemistry Research* **2012**, 51, 9145.
- [65] J. Choma, W. Burakiewicz-Mortka, M. Jaroniec, Z. Li, J. Klinik, *Journal of Colloid and Interface Science* **1999**, 214, 438.
- [66] J.-w. Lang, X.-b. Yan, W.-w. Liu, R.-t. Wang, Q.-j. Xue, *Journal of Power Sources* **2012**, 204, 220.
- [67] C. F. Miller, G. W. Simmons, R. P. Wei, *Scripta Materialia* **2000**, 42, 227.
- [68] A. C. Ferrari, J. Robertson, *Physical Review B* **2000**, 61, 14095.
- [69] M. A. Pimenta, G. Dresselhaus, M. S. Dresselhaus, L. G. Cancado, A. Jorio, R. Saito, *Physical Chemistry Chemical Physics* **2007**, 9, 1276.

- [70] H. Lindstrom, S. Sodergren, A. Solbrand, H. Rensmo, J. Hjelm, A. Hagfeldt, S.-E. Lindquist, *The Journal of Physical Chemistry B* **1997**, *101*, 7717.
- [71] T. C. Liu, W. G. Pell, B. E. Conway, S. L. Roberson, *Journal of The Electrochemical Society* **1998**, *145*, 1882.
- [72] X. Wang, G. Li, Z. Chen, V. Augustyn, X. Ma, G. Wang, B. Dunn, Y. Lu, *Advanced Energy Materials* **2011**, *1*, 1089.
- [73] Y. S. Hu, Y. G. Guo, R. Dominko, M. Gaberscek, J. Jamnik, J. Maier, *Advanced Materials* **2007**, *19*, 1963.
- [74] P.-C. Chen, G. Shen, Y. Shi, H. Chen, C. Zhou, *ACS Nano* **2010**, *4*, 4403.
- [75] F. Wohler, *Phil. Mag.* **1825**, *66*, 263.
- [76] D. Schlenker, J. Dumas, M. Greenblatt, S. Smaalen, *Physics and Chemistry of Low-Dimensional Inorganic Conductors*, Plenum, New York **1996**.
- [77] S. Raj, H. Matsui, S. Souma, T. Sato, T. Takahashi, A. Chakraborty, D. D. Sarma, P. Mahadevan, S. Oishi, W. H. McCarroll, M. Greenblatt, *Physical Review B* **2007**, *75*, 155116.
- [78] C. Tsang, S. Y. Lai, A. Manthiram, *Inorganic Chemistry* **1997**, *36*, 2206.
- [79] C. Schlenker, J. Dumas, C. Escribe-Filippini, H. Guyot, J. Marcus, J. Fourcaudot, *Philos. Mae. B* **1985**, *52*, 643.
- [80] E. Canadell, M. H. Whangbo, *Chemical Reviews* **1991**, *91*, 965.
- [81] M. Onoda, K. Toriumi, Y. Matsuda, M. Sato, *Journal of Solid State Chemistry* **1987**, *66*, 163.
- [82] N. Sotani, T. Manago, T. Suzuki, K. Eda, *Journal of Solid State Chemistry* **2001**, *159*, 87.
- [83] D. M. Thomas, E. M. McCarron Iii, *Materials Research Bulletin* **1986**, *21*, 945.

- [84] A. Du, B. Zhou, Y. Zhong, X. Zhu, G. Gao, G. Wu, Z. Zhang, J. Shen, *Journal of Sol-Gel Science and Technology* **2011**, 58, 225.
- [85] W.-S. Kim, H.-C. Kim, S.-H. Hong, *Journal of Nanoparticle Research* **2011**, 12, 1889.
- [86] Z. Chen, Y. Qin, D. Weng, Q. Xiao, Y. Peng, X. Wang, H. Li, F. Wei, Y. Lu, *Advanced Functional Materials* **2009**, 19, 3420.
- [87] C. J. Brinker, G. W. Scherer, *Sol-gel science: the physics and chemistry of sol-gel processing*, Academic Press, Boston **1990**.
- [88] M. I. Yanovskaya, I. E. Obvintseva, V. G. Kessler, B. S. Galyamov, S. I. Kucheiko, R. R. Shifrina, N. Y. Turova, *Journal of Non-Crystalline Solids* **1990**, 124, 155.
- [89] S. H. Lee, M. S. Seong, E. Tracy, A. Mascarenhas, R. Pitts, S. K. Deb, *Solid State Ionics* **2002**, 147, 129.
- [90] L. Q. Mai, B. Hu, W. Chen, Y. Y. Qi, C. S. Lao, R. S. Yang, Y. Dai, Z. L. Wang, *Advanced Materials* **2007**, 19, 3712.
- [91] K. Eda, K. FURUSAWA, F. HATAYAMA, S. TAKAGI, N. SOTANI, *Bull. Chem. Soc. Jpn.* **1991**, 64, 161.
- [92] G. R. Patzke, A. Michailovski, F. Krumeich, R. Nesper, J.-D. Grunwaldt, A. Baiker, *Chemistry of Materials* **2004**, 16, 1126.
- [93] T. Brezesinski, J. Wang, S. H. Tolbert, B. Dunn, *Nat Mater* **2010**, 9, 146.